ISOMERIZATION OF ALPHA-PINENE OXIDE OVER SOLID ACID CATALYSTS

D. B. R. A. DE SILVA

(B.Sc. (Hons.), UNIVERSITY OF PERADENIYA, SRI LANKA)

A THESIS SUBMITTED

FOR THE DEGREE OF MASTER OF SCIENCE

DEPARTMENT OF CHEMISTRY

NATIONAL UNIVERSITY OF SINGAPORE

2003

Acknowledgements

First and foremost, I would like to thank my supervisor A/P G.K. Chuah, for her constant encouragement, invaluable guidance, patience and understanding throughout the length of my candidature in NUS. I am also grateful to A/P Stephan Jaenicke, for his invaluable guidance.

I would also like to thank all the other members of our research group for their kind help and encouragement during my candidature.

Thanks are due to my parents and wife for their understanding, encouragement and support.

Finally, I wish to express my gratitude to the National University of Singapore for awarding me a valuable research scholarship.

TABLE OF CONTENTS

	PAGE
Acknowledgement	i
Table of Contents	ii
Summary	v
List of Tables	vii
List of Figures	ix
Chapter I Introduction	
1.1 Mesoporous Molecular Sieves	1
1.1.1 Catalytic Application of Mesoporous Materials	2
1.1.2 Modification of Mesoporous Materials	2
1.1.3 Micro- and Mesoporous Materials	4
1.2 Environment Impact of Solid Catalysts	6
1.3 Solid Acid and Catalysts	8
1.4 Supported Oxide Catalysts	9
1.4.1 Metal Oxide Supported Boron Oxide	13
1.4.2 SiO_2-Supported ZrO_2 Catalysts	15
1.4.3 $InCl_3$-Supported Solid Acid Catalysts	16
1.5 Methodology	16
1.6 Isomerization of α-Pinene oxide	24
1.7 Beckmann Rearrangement	27
1.8 Aims of the Project	29

Chapter II Experimental

2.1 Preparation of Catalysts 31

2.1.1 Synthesis of Hexagonal Aluminosilicate Mesoporous Materials (MSU-S) 31

2.1.2 Synthesis of Metal Oxide-Supported Boron Oxide 34

2.1.3 Preparation of SiO_2/ZrO_2 Catalyst using Silica Glass and Quartz Chips 34

2.1.4 Synthesis of $InCl_3$ Supported on ZrO_2 and $Zr(OH)_4$ Catalysts 35

2.1.5 Synthesis of Phosphated Zirconia 36

2.1.6 Synthesis of Zirconia-Supported Tungsten Oxide Catalysts 36

2.2 Catalytic Characterization 36

2.2.1 X-Ray Powder Diffraction 37

2.2.2 BET Surface Area and Porosity Determination 38

2.2.3 Pyridine Adsorption IR 43

2.2.4 Solid State Nuclear Magnetic Resonance (NMR) Spectroscopy 44

2.3 Catalytic Activity Tests

2.3.1 α-Pinene Oxide Isomerization Reaction 47

2.3.2 Liquid-Phase Beckmann Rearrangement of Cyclohexanone Oxime 50

Chapter III Physical Properties of Synthesized Catalysts

3.1 MSU-S Type Mesoporous Materials 52

3.1.1 X-Ray Diffraction 52

3.1.2 Bet Surface Area and Pore Volume 55

3.1.3 ^{27}Al-MAS and ^{29}Si-MAS Solid State NMR Spectroscopy 60

3.1.4 Pyridine Adsorption 65

3.2 Silica-Supported Boron Oxide Catalysts

3.2.1 Powder X-Ray Diffraction 67

3.2.2 BET surface Area and Pore Volume 71

3.2.3 ^{11}B-MAS NMR 72

3.2.4 IR Pyridine Adsorption 74

3.3 $InCl_3$-Supported on $Zr(OH)_4$ Catalyst

3.3.1 X-Ray Diffraction 76

3.3.2 BET Surface Area and Pore Volume 77

3.3.3 IR Pyridine Adsorption 78

3.4 ZrO_2-Supported SiO_2 Catalysts

3.4.1 Powder X-Ray Diffraction 79

Conclusion 85

Chapter IV Catalytic Studies

4.1 α-Pinene Oxide Isomerization Reaction 87

4.1.1 Catalytic Activity of HY Zeolite 87

4.1.2 Catalytic Activity of MSU-S Materials 90

4.1.3 Catalytic Activity of Metal Oxide-Supported Boron Oxide 100

4.1.4 Catalytic Activity of $InCl_3$-Supported on ZrO_2 107

4.1.5 Catalytic Activity of ZrO_2-Supported SiO_2 Catalysts 110

4.2 Liquid-Phase Beckmann Rearrangement of Cyclohexanone Oxime 111

Conclusion 112

References 114

Summary

Hexagonal aluminosilicate mesostructures were prepared from nanoclustered zeolite Y (MSU-S_{HY}, Si/Al ratio of 25, 50 and 70) and zeolite beta seeds (MSU-$S_{(BEA)}$, Si/Al = 67). For comparison, Al-MCM-41 with Si/Al =70 and HCl-treated MSU-S_{HY}(70) also prepared. The surface area, total pore volume, micropore volume and d_o spacing of the samples increased with increase of Si/Al ratio. The MSU-S_{HY} material with Si/Al = 70 was found to have the highest surface area (976 m^2/g) and total pore volume (0.99 cc/g). MSU-S_{HY} with Si/Al = 25 and 50 had surface areas above 815 m^2/g and total pore volume around 0.80 cc/g. The d_{100} increased from 37.75 Å (Si/Al = 25) to 41.26 Å (Si/Al = 70) with decrease of Al content. N_2 sorption data indicated presence of both micro- and mesopores. About 10% of the surface area is due to microporous. Compared to the untreated MSU-S_{HY}(70), the HCl-treated MSU-S_{HY}(70) had lower surface area, total pore volume and d_o value.

From pyridine adsorption studies, it was found that only Lewis acidity was present in MSU-S materials. Al-MCM-41(70) showed the presence of both Brønsted and Lewis acidity. The surface area and pore volume of B_2O_3/SiO_2 samples decreased with increase of boron oxide loading. XRD data showed that boron was present in the hydrated form, H_3BO_3, in B_2O_3/SiO_2. Both BO_3 and BO_4 units were detected by NMR studies. The wt% B_2O_3/SiO_2 samples showed strong Lewis acidity. Brønsted acidity was detected only with boron oxide loading of 15 wt% and higher.

$InCl_3/Zr(OH)_4$ samples were X-ray amorphous. The samples showed both Lewis and Brønsted acidity. The surface area and pore volume decreased with increase of $InCl_3$ loading. Both surface area and pore volume increased with digestion

time and Si content in hydrous zirconia. The presence of Si also favors the tetragonal phase. Samples digested with Si for one day had high crystalline size (119 Å) compared to crystalline size of samples digested for 8 days (76.6 Å). $InCl_3/Zr(OH)_4$ was not a good catalyst for the isomerization reaction. It showed very low selectivity to campholenic aldehyde with increase of $InCl_3$ loading, ~ 49%.

MSU-S_{HY} materials are good catalysts for α-pinene oxide isomerization. Toluene was a good solvent for α-pinene oxide isomerization. The conversion was higher in polar solvents but the selectivity decreased. The selectivity to campholenic aldehyde increased from 73% to 86% after 8 h in toluene with increase of Si/Al ratio from 25 to 70. HCl-treated MSU-S_{HY} (70) showed 100% selectivity with 47% conversion after 8 h.

B_2O_3/SiO_2 catalysts were also active. The conversion increased with boron oxide loading and reached a maximum value of 89% after 8 h at room temperature in toluene with 15 wt.% boron oxide loading. Despite the increase in activity, the selectivity towards campholenic aldehyde was independent of boron oxide loading. At room temperature the selectivity was around 70%.

LIST OF TABLES

PAGE

[1] Table 1-1 E-Factors in the chemical industry. 7

[2] Table 1-2 Number of solid acid, base and acid-base bi-functional catalysts in industrial process. 9

[3] Table 1-3 Infrared bands of pyridine adsorbed on solid acid catalysts in the 1400-1700 cm^{-1} region. 22

[4] Table 2-1 Synthesis of hexagonal aluminosilicate mesostructures from HY zeolite seeds. 32

[5] Table 3-1 XRD data of MSU-S samples and Al-MCM-41(70). 55

[6] Table 3-2 Physical properties of MSU-S type mesoporous materials. 60

[7] Table 3-3 Tetrahedral amuminum/octahedral aluminum ratio from ^{27}Al-MAS NMR. 63

[8] Table 3-4 ^{29}Si-MAS NMR data of mesoporous catalysts. 65

[9] Table 3-5 BET surface area and pore volume of supported boron oxide calcined at 350 ^{o}C. 71

[10] Table 3-6 BET surface area and pore volume of supported $InCl_3$ catalysts dried at 120 ^{o}C. 78

[11] Table 3-7 Microstructural parameters for calcined ZrO_2 samples 82

[12] Table 3-8 Weight loss of glass and quartz during digestion. 83

[13] Table 3-9 BET surface area and pore volume of hydrous ZrO_2 digested with glass and quartz. 84

[14] Table 3-10 BET surface area, pore volume and amount of Si of ZrO_2 digested with glass and quartz. 84

[15] Table 4-1 Conversion, selectivity and yield over HY zeolites and H-Beta after

4 h at room temperature in toluene 89

[16] Table 4-2 Selectivity to campholenic aldehyde over various catalysts 91

[17] Table 4-3 Effect of various solvents for α-pinene oxide isomerization over MSU-S_{HY}(70) at room temperature. 97

[18] Table 4-4 Conversion and selectivity over different supported boron oxide catalysts 101

[19] Table 4-5 Effect of various solvents for α-pinene oxide isomerization over 15% B_2O_3/SiO_2 at room temperature. 105

[20] Table 4-6 α-pinene oxide isomerization over $InCl_3$-supported on hydrous ZrO_2 and ZrO_2. 107

[21] Table 4-7 α-pinene oxide rearrangement over hydrous ZrO_2 and ZrO_2 digested with glass and quartz, at room temperature after 24 h in toluene 110

LIST OF FIGURES

PAGE

[1] Scheme 1-1 Synthesis of MCM-41: Liquid crystal initial mechanism 1

[2] Scheme 1-2 Various arrangement of oxide catalysts on a support 10

[3] Scheme 1-3 Illustration of the stages in the preparation of supported metal catalysts by incipient wetness method 12

[4] Scheme 1-4 Major products formed during acid-catalyzed rearrangement of α-pinene oxide isomerization 25

[5] Scheme 1-5 Postulated mechanism for the formation of campholenic aldehyde and isomeric aldehyde 26

[6] Scheme 1-6 Mechanism for the rearrangement of oxime (I) to amide (V) 28

[7] Scheme 2-1 Adsorption isotherms 41

[8] Scheme 2-2 De Boer's five types of hysteresis 42

[9] Scheme 2-3 Possible hysteresis loops for mesoporous materials 43

[10] Scheme 2-4 Ranges of ^{29}Si NMR chemical shifts of Si(nAl) units in zeolite 46

[11] Fig. 2-1 Gas chromatogram of 97% pure α-pinene oxide dissolved in toluene 48

[12] Fig. 2-2 Gas chromatogram of cyclohexanone oxime dissolved in N,N-dimethylformamide 50

[13] Fig. 2-3 Gas chromatogram of Beckmann rearrangement of cyclohexanone oxime over P_2O_5 in N,N-dimethylformamide at 100 ^{o}C after 2.5 h 51

[14] Fig. 3-1 XRD diffraction patterns of calcined (a) MSU-S_{HY}(25), MSU-S_{HY}(50), (c) HCl-treated MSU-S_{HY}(70) and (d) MSU-S_{HY}(70) 53

[15] Fig. 3-2 XRD diffraction patterns of calcined (a) MSU-S_{BEA}(67) and (b) Al-MCM-41(70) 54

[16] Fig. 3-3 Wide-angle XRD patterns of calcined (a) MSU-S_{HY}(25), (b) MSU-S_{HY}(50) 54

[17] Fig. 3-4 Wide-angle XRD pattern of calcined (a) MSU-S_{HY}(70) 55

[18] Fig. 3-5 N_2 adsorption/desorption isotherm and pore size distribution for calcined MSU-S_{HY}(25) 57

[19] Fig. 3-6 N_2 adsorption/desorption isotherm and pore size distribution for calcined MSU-S_{HY}(50) 57

[20] Fig. 3-7 N_2 adsorption/desorption isotherm and pore size distribution for calcined MSU-S_{HY}(70) 58

[21] Fig 3-8 N_2 adsorption/desorption isotherm and pore size distribution for calcined MSU-S_{HY}(70) after HCl-treatment 58

[22] Fig. 3-9 N_2 adsorption/desorption isotherm and pore size distribution for calcined MSU-S_{BEA}(67) 59

[23] Fig 3-10 N_2 adsorption/desorption isotherm and pore size distribution for calcined Al-MCM-41(70) 59

[24] Fig. 3-11 ^{27}Al-MAS NMR spectra of (a) HCl-treated MSU-S_{HY}(70), (b) MSU-S_{HY}(25), (c) MSU-S_{HY}(50), (d) MSU-S_{HY}(70) 61

[25] Fig. 3-12 ^{29}Al-MAS NMR spectra of (a) Al-MCM-41(70), (b) MSU-S_{BEA}(67) 62

[26] Fig. 3-13 ^{29}Si-MAS NMR of (a) MSU-S_{HY}(25), (b) MSU-S_{HY}(50) 62

[27] Fig. 3-14 ^{29}Si-MAS NMR of (a) MSU-S_{HY}(70), (b)HCl-treated MSU-S_{HY}(50) 64

[28] Fig 3-15 ^{29}Si-MAS NMR of (a) MSU-S_{BEA}(67), (b) Al-MCM-41(70) 64

[29] Fig. 3-16 IR pyridine adsorption of MSU-S materials at room temperature 66

[30] Fig. 3-17 IR pyridine adsorption of MSU-S materials at 100 ^{o}C 66

[31] Fig. 3-18 XRD patterns of wt.% B_2O_3/SiO_2 67

[32] Fig. 3-19 XRD of 15% B_2O_3/SiO_2 at different temperatures 68

[33] Fig. 3-20 XRD of calcined 15% B_2O_3/Al_2O_3 69

[34] Fig. 3-21 XRD of calcined 15% B_2O_3/TiO_2 70

[35] Fig. 3-22 XRD of calcined 15% B_2O_3/ZrO_2 70

[36] Fig. 3-23 Surface area and pore volume of silica-supported boria catalysts 72

[37] Scheme 3-1 Proposed structure of metal oxide-supported boria catalyst 73

[38] Fig. 3-24 ^{11}B-MAS NMR of wt% B_2O_3/SiO_2 73

[39] Fig. 3-25 ^{11}B-MAS NMR of 15% B_2O_3/SiO_2 after drying at 100 ^{o}C 74

[40] Fig. 3-26 IR spectra of pyridine adsorbed at room temperature on wt.% B_2O_3/SiO_2 75

[41] Fig. 3-27 Pyridine adsorbed on 15% B_2O_3/SiO_2 at different temperatures 76

[42] Fig. 3-28 XRD of mmol $InCl_3$/g $Zr(OH)_4$ 77

[43] Fig. 3-29 IR pyridine adsorbed of 2 mmol $InCl_3$/g $Zr(OH)_4$ at different temperatures 79

[44] Fig. 3-30 XRD of hydrous zirconia samples digested with quartz chips 81

[45] Fig. 3-31 XRD of hydrous zirconia samples digested with glass chips 82

[46] Fig. 3-32 % Tetragonal phase vs digestion time 83

[47] Fig. 4-1 Conversion of α-pinene oxide vs reaction time over HY zeolites 89

[48] Fig. 4-2 Selectivity vs time over HY zeolites 90

[49] Fig. 4-3 Conversion of α-pinene oxide vs reaction time over MSU-S catalysts 93

[50] Fig. 4-4 Gas chromatogram of α-pinene oxide isomerization reaction MSU-S_{HY}(70) 93

[51] Fig. 4-5 Selectivity to campholenic aldehyde vs time over MSU-S 94

[52] Fig. 4-6 Effect of temperature over activity, selectivity and yield over MSU-S materials 95

[53] Fig. 4-7 Plot of ln[-ln(1-conversion)] vs 1/T for MSU-S_{HY}(70) 96

[54] Fig. 4-8 Selectivity vs conversion for MSU-S catalysts 98

[55] Fig. 4-9 Conversion vs time for regenerated MSU-S materials 99

[56] Fig. 4-10 Selectivity vs time for regenerated MSU-S materials 100

[57] Fig. 4-11 Effect of boria loading on α-pinene oxide isomerization over wt% B_2O_3/SiO_2 102

[58] Fig. 4-12 Gas chromatogram for α-pinene oxide isomerization over 15 wt% B_2O_3/SiO_2 103

[59] Fig. 4-13 Effect of temperature on activity, selectivity, and yield to campholenic aldehyde over 15 wt% B_2O_3/SiO_2 103

[60] Fig. 4-14 Plot of ln[-ln(1-conversion) vs 1/T for 15% B_2O_3 104

[61] Fig. 4-15 Conversion vs time for regenerated 15% B_2O_3/SiO_2 106

[62] Fig. 4-16 Selectivity vs time for regenerated 15% B_2O_3/SiO_2 107

[63] Fig. 4-17 Conversion of α-pinene oxide versus time at room temperature in toluene over mmol $InCl_3$/g $Zr(OH)_4$ 108

[64] Fig. 4-18 Selectivity to campholenic aldehyde versus time at room temperature in toluene over mmol $InCl_3$/g $Zr(OH)_4$ 109

[65] Fig. 4-19 Gas chromatogram of homogeneous liquid-phase Beckmann rearrangement of cyclohexanone oxime over P_2O_5 at 100 ^oC in N,N-dimethylformamide after 2.5 h 112

CHAPTER I

INTRODUCTION

1.1 Mesoporous Molecular Sieves

The first successful attempt to synthesize mesoporous materials by using a surfactant as a template was made by Yanagisawa et al. in 1990 [1]. These mesoporous sieves with pore diameter ranging from 1.8 to 3.2 nm were prepared by heating a layered polysilicate kaenemite in an aqueous solution of alkyltrimethylammonium with different alkyl-chain lengths. In 1992, researchers in Mobile Corporation reported a family of mesoporous materials (M41S) including hexagonal MCM-41, cubic MCM-48 and lamellar MCM-50. These materials were synthesized (Scheme 1-1) by polymerizing a silica source around an organic liquid crystal template (LCT) of quaternary ammonium surfactants. Calcination of these materials led to removal of surfactant, and to high order silica, both in terms of uniform pore size and long-range order. The surface area is very high, typically ca. 1000 m^2g^{-1} and the pore size is monodispersed and varies predictably with surfactant chain length.

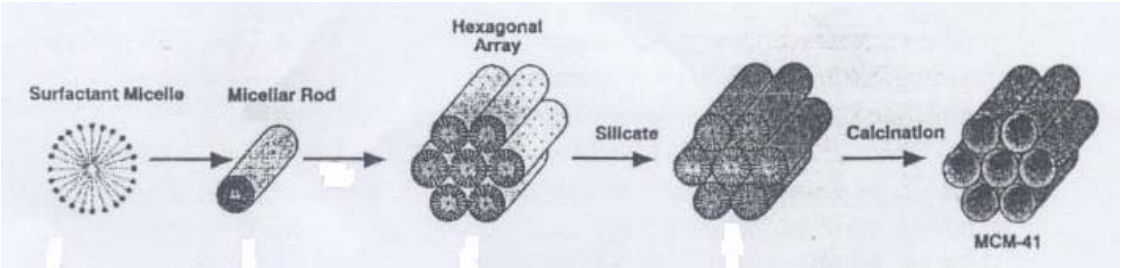

Scheme 1-1 Synthesis of MCM-41: Liquid crystal initiative mechanism [2].

1.1.1 Catalytic Applications of Mesoporous Materials

Today mesoporous molecular sieves with well-defined pore diameters ranging from 20 to 500 Å have been successfully synthesized by various researchers and these materials have overcome the pore diameter constraint of zeolites (< 10 Å) and allowed the diffusion of larger molecules. Furthermore, high surface area and tunable pore size are among the many desirable properties that have made such materials the focus of great interest. In particular, mesostructured aluminosilicate compositions have been studied by many researchers, because these materials have many potential applications in catalysts and adsorption technology, particularly for use as acid catalysts for many reactions in chemical industry. Although, these materials are not as strongly acidic as zeolites, they are quite effective for reactions of larger molecules either in mild acid form or via impregnation with catalytically active metals or complexes for catalyzing reactions such as oligomerization of propene [3,4] and butane [5], alkylation of aromatic hydrocarbons [6-8], acylation of activated aromatics [9,10], and tetrahydropyranylation of alcohols [11].

1.1.2 Modification of Mesoporous Materials

Over the last few years different assembly pathways have been developed for the synthesis of hexagonal (MCM-41) [12, 13], cubic (MCM-48) [14-16], wormhole (HMS, MSU-H) [17, 18] lamellar-vesicular (MSU-G) [19], 2D hexagonal (SBA-15, MSU-H) [20, 21] and foam-like (MCF, MSU-F) [22, 23] mesoporous materials. However, when compared to conventional zeolites, these mesostructured materials have relatively low acidity and poor stability. Especially the hydrothermal and mechanical stability of all these materials is below the practical level for industrial applications. The poor stability of these mesoporous materials can be attributed in part

to the amorphous nature and thinness of the pore walls. Therefore, to enhance the performances of mesoporous molecular sieves, several attempts have been made to improve the hydrothermal stability and acidity. Some of the strategies that have been investigated are discussed in reference [24]. They include:

(i) decreasing the silianol group content of the framework by silylation of the surface -OH groups in order to make the surface more hydrophobic and thereby improve the stability in water [25].

(ii) increasing the thickness of MCM-41 by post-treatment of primary MCM-41 to improve the hydrothermal stability and subsequently grafting Al-centers into the framework walls [26].

(iii) adding salt to the synthesis gel to facilitate the condensation of silanol groups during the formation of the framework, thereby improving the framework cross link [27].

(iv) partially transforming the pore walls into a pentasil phase by post-synthesis treatment of the original mesoporous aluminosilicate with zeolite structure-directing agents, such as tetrapropylammonium salts [28, 29].

(v) generating microporous zeolites-mesostructure composite mixtures to improve both hydrothermal stability and acidity [30].

(vi) using triblock copolymer surfactants to make thick wall mesoporous structures such as SBA-15 [19, 20].

(vii) using neutral Gemini amine surfactants to make thick-walled, vesicle-like lamellar frameworks with improved hydrothermal stability [18].

1.1.3 Micro- and Mesoporous Materials

In general all these approaches have improved the stability and acidity in comparison to the originally reported M41S materials, but generation of microporosity within the amorphous pore walls of mesoporous aluminosilicate have gained more attention than the other approaches. In addition to their improved acidity and hydrothermal stability, materials with combined micro- and mesoporosity have many significant advantages over mesoporous molecular sieves, such as an improved diffusion rate for transport in catalytic processes; multifunctionality to process a large variety of feed stocks; capabilities of encapsulated waste in the micropores; controlled leaching rates for a constant and gradual release of an active components etc.

The first successful attempt to synthesize combined micro- and mesoporous materials was made by van Bekkum and co-workers in 1997 [31]. They transformed the preassembled walls of Al-MCM-41 into zeolitic structures by post-assembly treatment with a microporous zeolite structure director, tetrapropylammonium cations. Following-up on van Bekkum's approach, Kaliaguine et al. [28, 29] investigated the possibility of transforming a thicker wall mesostructured cellular foams (MCF) aluminosilicate into crystalline zeolitic framework. The acidity of this material was determined by pyridine adsorption and the results showed that the acidic strength was much stronger than the parent amorphous mesoporous material. Pinnavaia et al. [32] recently reported an alternative approach for the preparation of more acidic and hydrothermally stable mesostructures based on direct assembly of nanoclustered aluminosilicate precursors that normally nucleate zeolite type Y crystallization. These protozeolitic species, known as "zeolite seeds", promote zeolite nucleation by adopting AlO_4 and SiO_4 tetrahedral connectivity that resemble the secondary building

units of a crystalline zeolite. Following up on the use of zeolite seeds as precursors for the assembly of thermally stable structures, several researchers have used pentasil zeolite seeds, such as BEA and MFI type seeds [33-36]. In comparison to the faujasitic zeolite seeds, which are nucleated by sodium ions, pentasil zeolite seeds are nucleated by specific tetraalkylammonium ions. The structural evolution of nanoclusters leading to the nucleation of MFI silicate has been studied by in detail by van Santen [37] and Martens et al. [38, 39].

In further developing the concept of using protozeolitic nanoclusters for mesostructure assembly, Pinnavaia et al. [23] prepared hydrothermally stable and strongly acidic MCM-41 analogs from zeolite ZSM-5 and beta seeds, which are nucleated by tetrapropylammonium and tetraethylammonium cations, respectively. Zhang et al. [35, 36] also reported a hydrothermally stable MCM-41 analog, MAS-5 which was assembled from zeolite beta. MAS-5 showed stronger acidity than conventional Al-MCM-41 for 1, 3, 5-triisopropylbenzene cracking and higher catalytic activity than zeolite beta for alkylation of 2-butene with isobutene. Although the acidity of MAS-5 reported to be very similar to zeolite beta, the higher catalytic activity for the alkylation was attributed to the easier diffusion of products in the mesoporous channels of MAS-5 than in microporous zeolite beta. An approach to assemble larger pore SBA-15 and MCF analogs with improved hydrothermal stability and acidity using nanoclustered faujasite, ZSM-5 and beta seeds as precursors under mild acidic conditions has been reported [33]. The resulting large hexagonal and foam-like materials (denoted MSU-S/F_{FAU}, MSU-S/F_{MFI} and MSU-S/F_{Beta}) showed higher stability in boiling water and under steaming conditions. All these materials exhibited higher cumene cracking activities than corresponding Al-MCF. Most

recently, Han et al. [40] reported a hydrothermally stable SBA-15 analog (denoted MAS-9) assembled from ZSM-5 seeds. An interesting extension of the use of zeolite seeds as grafting to prepare hydrothermally stable and strongly acidic mesostructures sources was reported by Kaliaguine et al. [41]. A clear ZSM-5 seed solution was used to graft the seeds onto the framework walls of a primary Al-SBA-15. The resultant SBA-15 analog, ZC MesoAS, showed higher Brønsted acid sites compared to the parent Al-SBA-15. Recently, an ordered mesoporous organosilica hybrid material with crystal like framework walls was successfully synthesized by Inagaki et al. [42]. This material has a hexagonal array of mesopores with a lattice constant of 52.5 Å, and crystal-like pore walls that exhibit structural periodicity with a spacing of 7.6 Å along the channel direction.

The research focus in the area of mesoporous materials is in the development of materials with tunable pore dimensions and fully crystalline walls that has high thermal and mechanical stability. Although at present these micro- and mesoporous aluminosilicates have limited application in chemical industry, they are expected to play an important role as solid acid catalysts.

1.2 Environmental Impact of Solid Catalysts.

The requirement for more environmentally friendly production technology in the chemical industry is universally accepted and much progress has already been made. The control of discharge of waste products into the environment and limiting the manufacture, storage, transport and use of certain hazardous chemicals, have been introduced to environmentally friendly technology.

Two useful measures of the environmental impact of chemical processes are the E-factor, defined by the mass ratio of waste to desired product, and the atomic utilization, calculated by dividing the molecular weight of the desired product by the sum of the molecular weights of all substances produced in the stoichiometric equation [43]. Processes employing acids and bases requiring neutralization, or stoichiometric redox reagents, represent the major sources of waste production in the form of salts and heavy metals and have high E-factors and low atomic utilization. The E-factor increases largely from bulk to fine chemicals and pharmaceuticals [44] (Table 1-1). Reactions employed in the fine chemical industry include isomerization, and Friedel Crafts reactions which are catalyzed by Lewis acids such as $ZnCl_2$, $AlCl_3$, reductions with metal hydrides or dissolving metals such as zinc or iron, all of which generate prohibitive amounts of metal-containing wastes. Moreover, many other acid-catalyzed reactions generate chloride-containing wastes. By introducing effective heterogeneous catalysts in chemical industry, two goals can be achieved. The first is elimination of such wastes; the second is the reduction of dependence on the use of hazardous chemicals such as dimethylsulphate, peracids, sodium azide, halogens and HF.

Table 1-1 E-factors in the chemical industry [44]

Industry segment	Product tonnage[a]	E (kg waste/kg product)
Bulk chemicals	$<10^4$-10^6	<1→ 5
Fine chemicals	10^2-10^4	5→>50
Pharmaceuticals	10-10^3	25→>100

[a] Depending on the product, this could be the capacity of a single plant or the worldwide production.

1.3 Solid Acids and Catalysts

According to Tanabe [45], a solid acid can be defined as a solid on whose surface a basic indicator changes its color or a base undergoes chemisorption. By taking into account both the Brønsted and Lewis definitions, generally we can consider a solid acid as a proton donor or an election pair acceptor. The amount of acid on a solid is expressed as number or mmol of acid sites per unit weight or per unit surface area of the solid acid. The strength of an acid can vary. Some solids have acid strength higher than 100% sulfuric acid. They are known as super solid acids with a Hammett acidity function, $H_o < -11.9$.

Solid acid-catalyzed reactions form one of the most extensive areas for the application of heterogeneous catalysis. Hundreds of solid acids have been developed to date. The range of materials available includes the acidic H-forms of ion-exchange resins, zeolites, and modified oxides such as sulfated zirconia, immobilized forms of Lewis acids such as metal halides and of Brønsted acids.

Solid acid catalysts have many advantages over liquid Brønsted and Lewis acid catalysts. They are non-corrosive, thermally stable, easily separated and recovered from liquid products. Moreover, in many cases they are designed to give higher activity, selectivity and longer lifetime.

The advantages of solid acid catalysts were first appreciated in the petroleum refining. Clays were used for this purpose as early as the 1930s. They were replaced firstly by synthetic silica-aluminas, and then by X and Y zeolites. These solid acids are used in reactions, such as cracking (X and Y zeolites), alkylation (zeolites, SiO_2-phosphoric

acid), and the formation of alcohols from olefins (SiO_2-phosphoric acid), etc. Increasingly, the benefits of solid acids are being applied to the fine chemical industry. According to a recent review in 1999 [46], out of 127 industrial processes using acid-base catalysts, solid acid catalysts are used in 103 cases (Table 1-2).

Table 1-2 Numbers of solid acid, base and acid–base bi-functional catalysts in industrial process [46].

Solid acid catalysts	103
Solid base catalysts	10
Solid acid – base bi-functional catalysts	14
Total	127

1.4 Supported Oxide Catalysts

Supported oxides have several advantages over unsupported materials. Supports can be used to improve the mechanical strength, the thermal stability and the lifetime of the catalyst. They can also provide ways to increase the surface area of the active species. In addition, supported oxides frequently have structural features and chemical compositions different from the surface of the bulk oxide. This difference arises mainly from the interaction of the oxide with the support and the size and shape of the catalytic species. There are several ways in which the active oxide can be found on the surface of the supported material. As shown in Scheme 1-2 (a), the active component and the support can be intimately mixed throughout the catalyst particle. This arrangement provides the maximum interaction between the support and the catalyst but it also leaves a large portion of the active material buried in the support. The second possibility is catalytic dispersion, as shown in Scheme 1-2 (b); the individual catalytic molecules are bound to the support surface as a localized binary

oxide. The third possibility is formation of monolayer on the support oxide as shown in Scheme 1-2 (c). Here also the catalyst support interaction is strong due to the larger contact area between the support and oxide. It is this monolayer coverage that is considered the best for a number of oxides [47]. However, in practice, it may not be possible to form a monolayer of catalytic species on supported metal oxide surface. Instead, there may be areas of monolayer coverage accompanied by some larger supported oxide particles and some uncovered supported surface (Scheme 1-2 (d)).

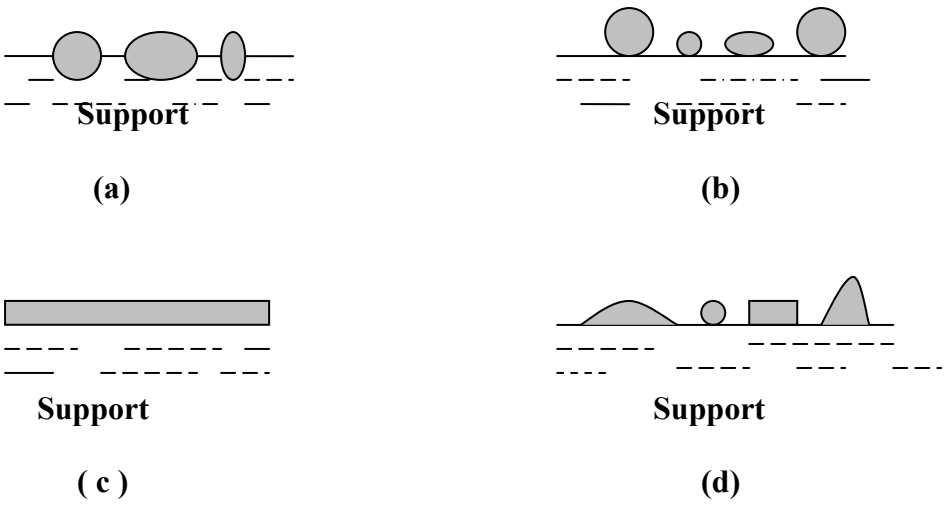

Scheme 1-2 Various arrangements of oxide catalysts on a support. (a) Portion of the catalyst buried in the support (b) catalyst molecules on the surface of the support (c) monomolecular layer of the catalyst on the support surface (d) mixture of monomolecular layers, larger particles of the catalyst, and molecules.

There are several methods commonly used to prepare supported oxide catalysts [48]. They differ mainly in the manner in which the active component or its precursor is placed in contact with the support. The supported species are calcined at appropriate temperatures to give the active catalyst.

Co-precipitation of the support and the catalytic material is achieved by treatment of a solution containing both the support precursor and the catalytic precursor with a suitable precipitating agent. The resulting precipitate contains species either as a single phase or as multiple phases, from which the active component and the support materials are produced. One disadvantage of this method is that a large portion of the active species is buried in the support hence unavailable for reactions. Co-precipitation method has been used to prepare MoO_3/SiO_2 catalyst, which is active for hydrodesulfurization reactions [49].

Another method for preparing supported oxide catalysts involves the dispersion of the active species or its precursor onto the surface of a support oxide. This can be achieved by equilibrium adsorption, incipient wetness or dry impregnation. The equilibrium adsorption procedure involves the adsorption of active species or its precursor from a solution in which the solid support is suspended. This procedure is also known as ion-exchange or grafting of the active species to the support surface. After adsorption is completed, the modified support is removed from the suspension, washed, dried and finally calcined. The isoelectric point (IEP) of the solid and the pH of the solution are very important factors in this method, because they determine the sign and extent of the charge on the support surface.

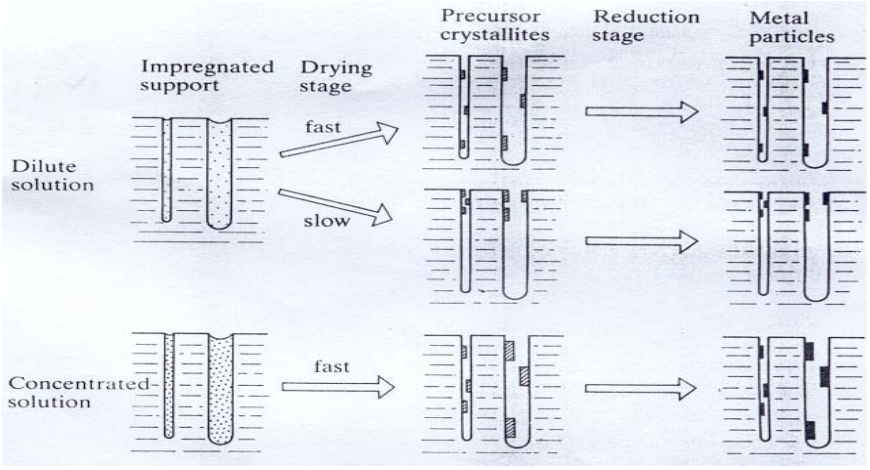

Scheme 1-3 Illustration of the stages in the preparation of supported metal catalysts by incipient wetness method [48].

The incipient wetness method involves the wetting of the support with just enough of a solution of the active species to fill the pores of the support material. This is normally achieved by adding the solution slowly to the solid material with continuous stirring. If the volume of the liquid needed to reach this point is known, the concentration of the solution can be adjusted to give the desired catalytic loading. Once the incipient wetness point has been reached, the solvent is evaporated and the modified support is calcined to give the catalyst. Incipient wetness can be used with aqueous or organic solutions depending on the solubility of the catalytic precursor. Evaporation of high surface tension solvents such as water can result in pore disruption in the support resulting in a decrease of the surface area of the catalyst. The average size of the catalytic precursor particles depends on the concentration of the solution used. High catalytic loadings tend to give larger particles than low loadings. If the drying step is performed slowly, the catalytic particles will migrate towards the external surface of the support. Therefore, to have a uniform distribution

of catalyst throughout the support, it is better to dry quickly. The procedure for catalytic preparation in terms of incipient wetness is illustrated in scheme 1-3 [48].

1.4.1 Metal Oxide-Supported Boron Oxide

B_2O_3 is usually used as a catalyst by dispersing it on support metal oxides, such as alumina [51-53], silica [54, 55], thoria [56], titania [57], zirconia [58-61]. Metal oxide-supported boria exhibit higher surface acidity, surface area, and thermal and mechanical strength when compared to the pure oxide supports.

In amorphous and crystalline compounds, boron may exist both in tetrahedral BO_4 and trigonal BO_3 units [62]. These two forms can be distinguished by either solid state NMR or IR spectroscopy. In ^{11}B-MAS NMR, the BO_4 unit gives a sharp resonance peak at ca. 2 ppm, whereas the signal for trigonally co-ordinated BO_3 appears as a doublet due to second order quadrupolar effect [63]. From the IR spectra of KBr discs of pure borax, boric acid and boria, BO_3 units show absorbance at 1460, 1190 and 885 cm^{-1} indicative of BO_3 units while the BO_4 units absorbs around 1350-1420 cm^{-1} [64]. The conventional method used for the preparation of boria supported on metal oxides is impregnation of the support with aqueous H_3BO_3 followed by calcination at the desired temperature. Supported boron oxides can also be prepared via vapour decomposition of a boron ester (e.g. $B(OEt)_3$) onto the support [55]. The latter resulted in uniform dispersion of B_2O_3 and showed much improved selectivity and activity for the Beckmann rearrangement of cyclohexanone oxime, compared to the conventional method [55]. In the vapour decomposition method, Sato et al. [55] reported that the rate of B_2O_3 deposition on SiO_2 surface was greatly influenced by the vapour decomposition temperature. The maximum B_2O_3 content, 34 wt% was

attained at about 350 ^{o}C. Furthermore, they reported that the amount of B_2O_3 deposited on SiO_2 did not depend on the surface area or on the average pore diameter, but on the pore volume of the support. The larger the pore volume of support, the more B_2O_3 could be deposited to give more active catalysts [55]. The maximum boria content was achieved when the pore volume was 1.35 ml/g. Moreover, the catalyst showed 98.6% conversion and 96.4% selectivity for the Beckmann rearrangement of cyclohexanone oxime to ε-caprolactam after 2 h at 250 ^{o}C.

The acidic properties and catalytic performance of various boria supported on metal oxides have been studied by many researchers. For the Beckmann rearrangement of cyclohexanone oxime, it was reported that relatively strong acid sites (H_o<-5.6) of B_2O_3/SiO_2 are responsible for the formation of ϵ-caprolactam with high selectivity [55]. On the other hand, Takahashi et al. [65] found that for H-ZSM-5 zeolite modified by B_2O_3, ϵ-caprolactam selectivity improves with the increase of the ratio of weak acid sites to strong acid sites. Curtin et al. [53] showed that the lactam selectivity is directly proportional to the concentration of medium strength acid sites of B_2O_3/Al_2O_3 (H_o< -13). Xu et al. [60] used the desorption of adsorbed ammonia at 200 ^{o}C to link active sites for Beckmann rearrangement to medium and strong acid sites on the surface of B_2O_3/ZrO_2 catalyst. In addition to Beckmann rearrangement of cyclohexanone oxime, boria supported on metal oxides are used to catalyze reactions such as hydrocarbon conversion [66], and xylene isomerisation reactions [67]. Generally, boria-supported oxides exhibit very strong acidity at low levels of boria loading due the specific reaction between surface OH groups of the support and boron oxide. At high loadings, moderately strong acid sites prevail as the strong acid sites are covered by B_2O_3. Xu et al. [60] found that tetrahedral oxygen co-ordinated boron

(BO_4) units are the main structure at low levels of boria loading (5% B_2O_3) on B_2O_3/ZrO_2. Trigonal BO_3 units increase with increasing boria content. Furthermore, they reported that the monolayer dispersed BO_4 state of boria is not an effective catalyst for lactam synthesis and the best performance of catalysis for B_2O_3/ZrO_2 is determined by a combination of dispersed boria species with mainly BO_3 as the structural units with a BO_4 sublayer between the support surface and the BO_3 structures.

Therefore, the performance of supported boria catalysts can be improved by proper control of variable factors such as nature of the support, load and dispersion of boria, and calcination temperature.

1.4.2 ZrO_2-Supported SiO_2 Catalysts

Zirconia is an oxide with a high melting point (about 2700 ^oC), low thermal conductivity and high corrosion resistance. The application of ZrO_2 as a catalyst support is promising due to its physical properties, amphoteric nature as well as its reducing and oxidizing capabilities [68, 69]. However, the surface area of ZrO_2 is not large compared with common supports such as SiO_2 or Al_2O_3. It is typically < 40 m^2/g. The reported highest acid strength of ZrO_2 is H_o = + 1.5 and the acid concentration are 0.06 and 0.28 mmol/g at $H_o \leq$ + 1.5 and $H_o \leq$ + 4.0 respectively. Zirconia has mainly Lewis acidity with some Brønsted acidity [70]. The incorporation of silica into zirconia gives stronger acid sites than either silica or zirconia alone [70]. It also imparts stability against surface area loss and crystallization upon heating [71]. ZrO_2-SiO_2 mixed oxides have been applied for reactions including alcohol

dehydration [72], alkene isomerization [73], and cumene dealkylation [72]. Therefore, ZrO_2-SiO_2 mixed oxides have been considered as potential solid acid catalysts in fine chemical industry. Sol-gel [74] and alkoxide [75] routes have been widely used to prepare ZrO_2-SiO_2 mixed oxides. In this study the SiO_2, in the form of silica glass and quartz chips is incorporated into zirconia.

1.4.3 Supported-$InCl_3$ Solid Acid Catalysts

In the area of synthesis chemistry, main group XIII metal salts have long been used as prominent Lewis acids. For example, aluminum and boron salts are known to be excellent promoters for Friedel-Crafts, Diels-Alder and Mukaiyama-aldol reactions [76]. On the other hand, less attention has been given to indium salts because of their low Lewis acidity compared with that of aluminum or boron salts [77]. However, the importance of indium chloride has been reported due to its ease of carbon nucleophiles formation by transmetallation [78], and its activity in the presence water [79]. The unsupported form of $InCl_3$ has been used in catalytic reactions [80,81], although there is now a shift to $InCl_3$ dispersed on various supports. The Lewis acid nature of $InCl_3$ and the reusability of the supported form have focused attention on this material [82].

1.5 Methodology

Determination of the strength of the acidic sites exposed on the solid surface as well as their distribution is a necessary requirement to understand the catalytic properties

of solid acids. A variety of methods has been suggested to determine the acidity of solid surfaces. They differ from each other in their chemical and physical properties.

The strength of an acid can be characterized by its dissociation constant, K_A

$$K_A = \frac{[H^+][A^-]}{[HA]} \quad (1)$$

$$pK_A = -\log K_A \quad (2)$$

The pK_A value cannot be measured directly. Hammett and Deyrup proposed an ordering of acid strengths based on the acidity function, H_O (Hammett function). The H_O scale permits a comparison of the strength of acids by taking into account their capability to transfer a proton to a neutral base or accept an electron pair from a neutral molecule of a basic indicator.

If the reaction proceeds by means of proton transfer from the solid surface to the adsorbate, the acid strength is expressed by

$$H_o = pK_A + \log[B]/[BH^+] \quad (3)$$

where $[B]$ and $[BH^+]$ are the concentrations of the neutral base (basic indicator) and its conjugate acid, respectively, and pK_A *is* $pK_{BH}+$

If the reaction proceeds by means of electron pair transfer from adsorbate to the solid surface, H_o is given by

$$H_o = pK_A + log[B]/[AB]$$

(4)

where [AB] is the concentration of neutral base

One method used for the determination of the acidic strength of a solid surface is the adsorption of an electrically neutral indicator and the observation of the colour appearing on the surface. The application of Hammett indicators for such determination was proposed by Walling [83]. The measure of the acidic strength of the surface is the pK_{BH+} value of the weakest basic indicator, which after adsorption exhibits the color of the conjugated acid. In this case, using the acidity function of Hammett, one can state that the acidic strength H_o of the investigated surface is less than or equal to the pK_{BH+} of the indicator used ($H_o = pK_{BH+}$).

Having a series of indicators with relatively small differences in pK_{BH+} values, one can determine the acidic strength of a surface, placing it between pK_{BH+} of the last indicator which changes its color ($pK_{BH+}1$) and the first which does not undergo any color change after adsorption ($pK_{BH+}2$). For such a case, $pK_{BH+}2 < H_O < pK_{BH+}1$. The acidic strength is usually determined by adding drops of a basic indicator solution to a suspension of the catalyst in a water free solvent. Some of the most commonly used indicators are methyl red, phenylazonaphthylamine, benzeneazodiphenylamine, anthraquinone, etc. The transformation of an indicator into its conjugated acid form can also be detected spectrometrically. The indicators are in this case adsorbed onto thin, optically transparent wafers of the catalyst. Absorption spectra can be compared with standard spectra of indicator solutions in acidic media.

The adsorption of bases is widely used for the determination of the acidity of solid surfaces. The adsorption may be measured from the gas phase or the liquid phase

(non-aqueous solvents). Ammonia, pyridine or aliphatic amines are the bases most often used in adsorption measurements. Their basic character is relatively weak and their strength decreases in the range: aliphatic amines > ammonia > pyridine and its alkyl derivatives. The center of basicity is the electron lone pair on the nitrogen. When chemisorbed on solid acids, amines can interact with acidic protons, electron acceptor sites, and hydrogen from neutral or weakly acidic hydroxy groups.

An acidic catalyst surface may provide Brønsted (protic) sites and Lewis (aprotic) sites. The former are typically surface hydroxy groups (OH_{solid}) on oxide surfaces, the latter are surface cations (L). A base (B) will interact with hydroxy groups through hydrogen bonding:

$$OH_{solid} + B \rightleftharpoons OH_{solid} \ldots B \quad (1)$$

The next step is proton transfer from hydroxy groups to base

$$OH_{solid} \ldots B \rightleftharpoons O^-_{solid} \ldots H^+ B \quad (2)$$

In the case of aprotic sites L, the base, B will form a Lewis acid-base interaction through the lone pair of electron on the nitrogen of base, B.

$$L + B \Leftrightarrow L \leftarrow B \quad (3)$$

Infrared spectroscopy (IR) has found large application for determining the nature of acid sites and acid strength of solid acids. An important advantage of IR is its capability to detect states exhibiting lifetimes of the order 10^{-12} s. Infrared spectroscopic studies of ammonia and pyridine adsorbed on solid acid surfaces make it possible to distinguish between Brønsted and Lewis acid sites and to assess their amounts independently. IR spectroscopy is extremely useful in detecting H-bonded

systems since it responds sensitively to the perturbations induced in the O-H oscillator and in the H-bonded base, B. The protonated base H^+B can easily be discriminated from the parent base when the proton transfer occurs and the H-bonding of the H^+B species to the conjugated surface base O^-_{solid} in the ion-pair complex $O^-_{solid}\ldots H^+B$ can be studied. When Lewis acid-base interactions are formed, IR spectroscopy can only provide information on the perturbation of the base, B. These perturbations may lead to modifications of the bond energies and hence, force constants and normal mode frequencies without any symmetry reduction. Depending on the molecular structure of the base, adduct formation may also lead to symmetry reduction so that a symmetry analysis of the vibrational spectra will provide information on the nature and structure of the adsorption complex. The following order of stability for surface species can be assigned: hydrogen bound molecules < protonated molecules < coordinatively bound molecules. However there exists no simple relationship between the stability of individual surface species and acidic strength of the binding surface sites. Furthermore, the acidic properties of surface sites may change with temperature.

Ammonia is widely used for the characterization of the acid properties of solid acids. It is a hard Lewis base and it is small in size. The various forms of expected chemisorbed NH_3 species, namely, coordinated, H-bonded and protonated NH_3 can be detected by IR spectroscopy and discriminated by their characteristic normal vibrations. The protonated form NH_4^+ gives rise to band near 1450 and 3130 cm^{-1}, whereas NH_3 coordinately bonded to Lewis acid sites shows bands near 1250, 1630, and 3330 cm^{-1}. However, several complications may arise with the use of ammonia as a detector for surface acidity. Due to its strong basicity (hardness), ammonia can be very strongly bonded to a wide variety of sites. Therefore, it cannot be considered as a very specific probe molecule, and it may not always provide ideal properties for

studies of surface acidity. Moreover, dissociative adsorption of NH_3 with formation of NH_2 and NH surface groups has been observed at elevated temperatures (≥ 500 K) on partially dehydroxylated oxide surfaces [84,85].

Pyridine is classified as a weaker base than ammonia, this being consistent with its pK_a value as determined in the liquid phase. However, gas phase basicities indicate that pyridine should be the stronger base relative to ammonia, and Parillo et al. [86] were able to demonstrate that pyridine is more easily protonated than ammonia and that the pyridinium ion is thermally more stable than the ammonium ion. The pyridine molecule can undergo coordination to aprotic sites; it can be protonated to form the pyridinium ion PyH^+ on acidic OH groups and it can undergo H-bonding with less acidic groups. The infrared spectra of pyridine coordination compounds are clearly distinct from those of PyH^+ and of H-bonded pyridine [87], so that the corresponding surface species can be quite easily distinguished. Infrared spectra measured for pyridine adsorption on solid acids in the 1400-1700 cm^{-1} are presented in Table 1-3 [87]. Pyridine ion bonded to Brønsted acid sites gave characteristic IR absorption bands at about 1485-1500 cm^{-1}, 1540 cm^{-1}, 1620 $cm^{-1}$and 1640 cm^{-1}, the "ring" vibration region of C_6H_5N. The characteristic bands of pyridine coordinatively bonded to Lewis acid sites appeared at 1447-1460 cm^{-1}, 1448-1503 cm^{-1}, ~1580 cm^{-1} and 1600-1633 cm^{-1}. Hydrogen bonded pyridine showed adsorption bands around 1440-1447 cm^{-1}, 1485-1490 cm^{-1}, and 1580-1600 cm^{-1}. Parry studied the IR spectra for pyridine adsorption on η-alumina [87]. He showed that evacuation at temperatures higher than room temperature caused disappearance of bands relevant to hydrogen bonded pyridine. After evacuation at 100 ^oC a band appeared at 1632 cm^{-1}; this band was ascribed to pyridine bound to Lewis acid sites. The most strongly bound pyridine with bands at 1459 cm^{-1} and 1632 cm^{-1} were observed after evacuation at 565 ^oC.

These two bands were ascribed to pyridine adsorbed on Lewis acid sites. On silica, Parry found [87] only hydrogen bound pyridine (bands at 1447 cm^{-1} and 1599 cm^{-1}). Evacuation at 150 ^{o}C caused disappearance of these bands, which indicated the weakness of pyridine binding to silica.

Table 1-3 Infrared bands of pyridine adsorbed on solid acid catalysts in the 1400-1700 cm^{-1} region [87].

H-bonded pyridine	Coordinately bonded pyridine	Pyridinium ion
1400-1447 (v.s.)	1447-1460 (v.s.)	
1485-1490 (w)	1488-1503 (v)	1485-1500 (v.s.)
1580-1600 (s)	~1580 (v)	1540 (s)
	1600-1633 (s)	~1620 (s)
		~1640 (s)

v.s.— very strong; s— strong; w— weak; v— variable.

Alkyl substitution in the 4-position increases the basicity of pyridines via inductive effects. The same is true for substitution in the 2- and 6- positions, in the latter case; however, the nitrogen lone pair is sterically shielded. The influence of these effects on the adsorption interaction with alumina surfaces was first investigated by Knözinger and Stolz [89]. They showed that 2,4,6-trimethylpyridine can still coordinately interact with Lewis acid sites, Al^{3+} on alumina surfaces, although the interaction is sterically hindered. However, the interaction is weaker than with unsubstituted pyridine. Benesi [88] has shown that 2, 6-dimethylpyridine may be used as a specific detector for protonic sites. Following the paper of Benesi, several workers have used

substituted pyridines as probe molecules for acid sites on various oxide materials [90-92]. Kotral and co-workers [93] suggested the use of N-H stretching mode of protonated pyridine to detect the strength of the conjugated basic center after proton transfer had occurred.

Temperature programmed desorption (TPD) of simple bases is another widely used method to assess the total number and acid strength of acid sites [94-97]. For example, ammonia TPD has been employed to characterize the acidity of ZSM-5 [94], mordenite [94,95], and Y-zeolite [96-98]. In a typical TPD experiment, the catalyst is contained in a reactor that can be heated at a linear rate. After pretreatment, the catalyst is saturated with a probe molecule under well-defined adsorption conditions. After the excess gas is flushed out of the reactor, the sample is heated in a flowing inert gas stream. A thermocouple inserted in the catalyst measures the temperature and a detector downstream measures the effluent gas composition. The concentration of the desorbing gas may be monitored by absorption/titration, thermal conductivity, flame ionization, or mass spectroscopy. Alternatively, TPD experiments may be carried out by using a microbalance to measure the changes in sample mass during heating. Inert gas flow rate, catalyst particle size, catalyst pore size, and catalyst bed depth affect the TPD spectra. Temperature programmed desorption studies of porous catalysts are generally carried out using reactors designed to minimize concentration gradients in the reactor.

In addition, any kind of acid catalyzed reactions such as cumene cracking, alkylation of benzene with propene, hydration of olefins, esterification of acetic acid with ethanol etc. can also be used to estimate the acidic property of solid acids.

1.6 Isomerization of α-Pinene Oxide.

Campholenic aldehyde (2) is an important intermediate used by the fragrance industry in the synthesis of santalol, and it is currently prepared by using Lewis acid catalyzed rearrangement of α-pinene oxide (1). α-Pinene oxide (1) is a reactive molecule which is readily rearranged to campholenic aldehyde (2) by acid catalysts giving several different products such as isomeric aldehyde (7), *iso*-pinocamphone (3), *trans*-carveol (4), *p*-cymene (5), and *trans*-sobrerol (6). The structural isomers (2) and (7) are almost always formed in a ratio depending on the catalyst used in every acid catalyzed reaction. The rearrangement of α-pinene oxide is facile and over 100 different products can be found under different reaction conditions with different catalysts. The major products formed during the acid catalyzed rearrangement are shown in Scheme 1-4.

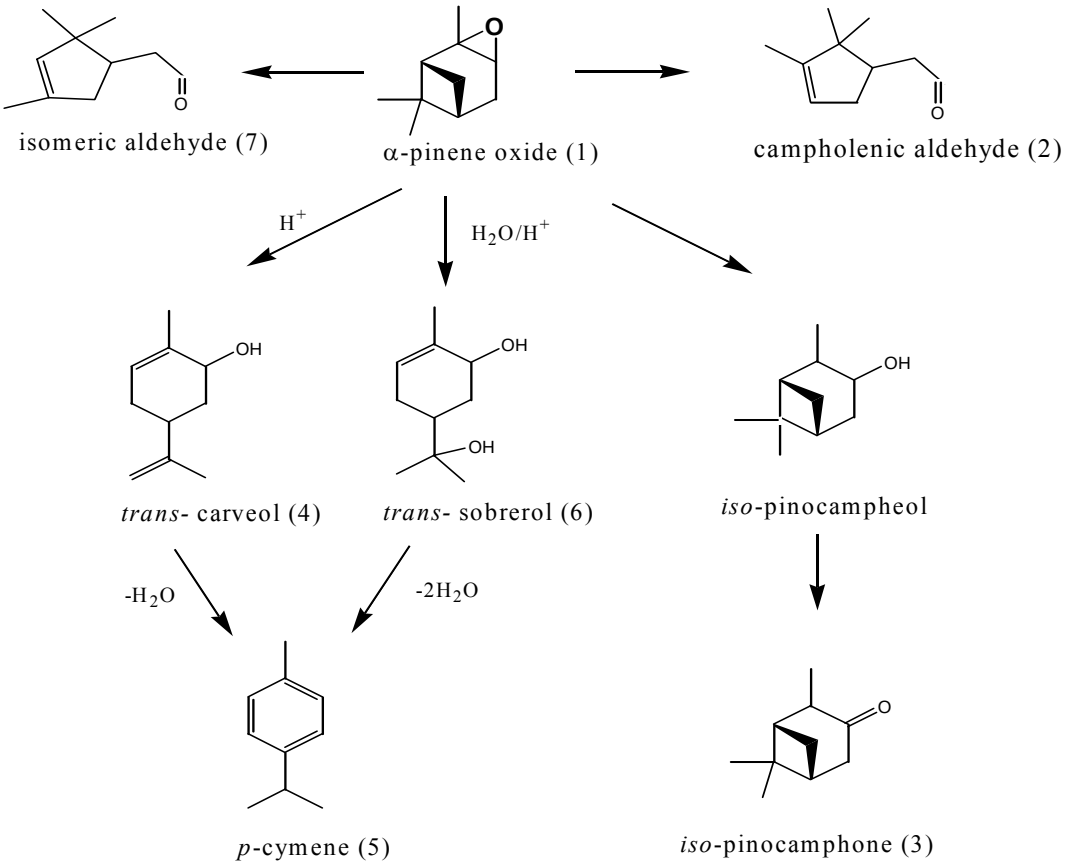

Scheme 1-4 Major products formed during acid-catalyzed rearrangement of α-pinene oxide.

The use of mild Lewis acids favors the product of campholenic aldehyde (2), while Brønsted acid sites will result in the formation of (4) , (5) and (6). Scheme 1-5 shows the reaction mechanism for the formation of campholenic aldehyde and isomeric aldehyde postulated by Carr et al. [99]. ^{1}H and ^{13}C NMR experiments and kinetic studies showed that the rate-determining step of the reaction does not involve opening of the cyclobutane ring. The first step is the cleavage of the C-C bond in the oxirane ring, followed by hydride shift. Then the seven membered heterocyclic ring undergoes C-O bond cleavage and resulting carbocation rearranges to give (2) or (7) depending on whether the isopropyl- or methylene bridge is shifted. The most active and selective homogeneous systems used for this reaction are $ZnBr_2$ and $ZnCl_2$.

These are very effective homogeneous catalysts that provide selectivity of about 85% in benzene towards campholenic aldehyde (2).

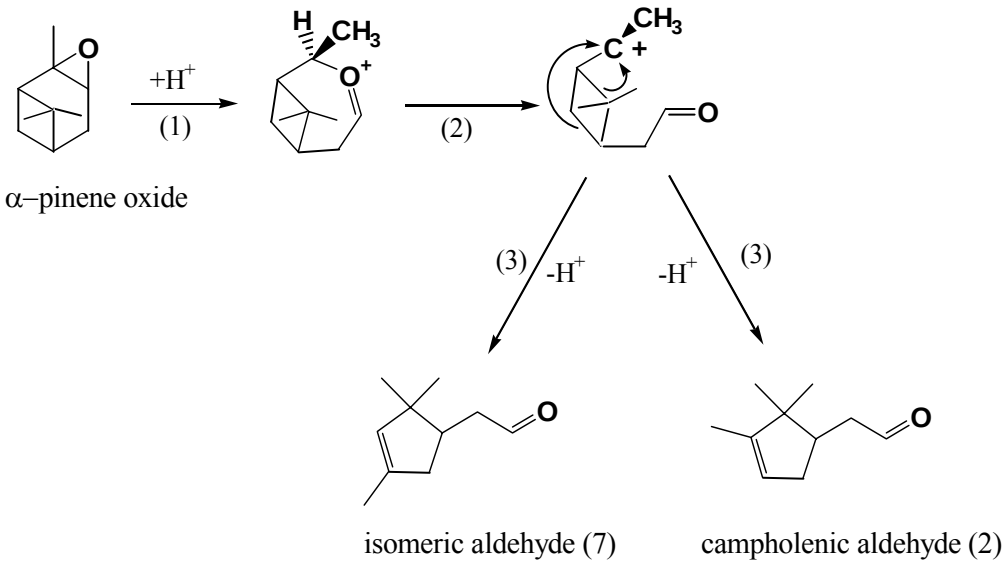

Scheme 1-5 Postulated mechanism for the formation of campholenic aldehyde and isomeric aldehyde [99].

The higher selectivity can be attributed to the highly stable intermediate formed by complexing with zinc. However, aqueous extraction of these catalysts from the reaction results in the formation of large quantities of zinc-contaminated water which is environmentally unacceptable; hence, these homogeneous catalysts must be replaced by effective heterogeneous catalysts. Many efforts have been made to find a truly heterogeneous system for this reaction.

H. van Bekkum and coworkers found that heteropolyacid; $H_4SiW_{12}O_{40}$ is very active catalyst for the rearrangement [100]. With benzene as a solvent, 100 % conversion was achieved after 15 min but the selectivity towards campholenic aldehyde was very low (34 %). In 1,2-dichloroethane the selectivity was 48 % and (7) was not detected

but several by-products including (3), (5) and (6) were found. In batch reactors, Holderich et al. [101] reported a 78 % yield using USY zeolite dealuminated by dilute HCl. Kunkeler et al. [102] reported 89 % selectivity towards campholenic aldehyde at a low conversion on Ti-Beta as a catalyst. Using a flow reactor, the same group achieved 94 % selectivity for the desired aldehyde with 95 % conversion with $C_2H_4Cl_2$ as a solvent, whereas with alkenes as solvents the selectivity reached 89 % at full conversion. However, the catalyst started to decay after 5-6 h. It has been reported that an active catalyst for the reaction can be obtained by impregnating Zn triflate on silica [103]. The selectivity for the aldehyde by using this system was 80 % at 50 % conversion but the selectivity decreased to 69 % at full conversion. Amorphous silica-aluminas have also been reported for the isomerisation of α-pinene oxide with a yield of 75 % at room temperature [104]. Despite their activity and selectivity, many of these heterogeneous catalysts suffered from the formation of various side-products, extensive decomposition, polymerization and decay of catalytic system.

1.7 Beckmann Rearrangement

ϵ-Caprolactam is a key intermediate for nylon-6. Generally, ϵ-caprolactam is industrially synthesized by liquid phase Beckmann rearrangement of cyclohexanone oxime using a strong acid such as concentrated sulfuric acid or fuming sulfuric acid. One problem in this method is the substantial amount of ammonium sulfate produced as a by-product. The reaction pathway for the Beckmann rearrangement is given in Scheme 1-6. The initial protonation at the oxygen atom of an oxime (I) gives an oxonium cation (II), followed by a migration of an alkyl group concomitant with liberation of water molecule affording a nitrilium cation (III). The nitrilium cation

(III) is hydrolyzed to form (IV) and, finally, its tautomer (V), an amide. The reaction is highly stereospecific.

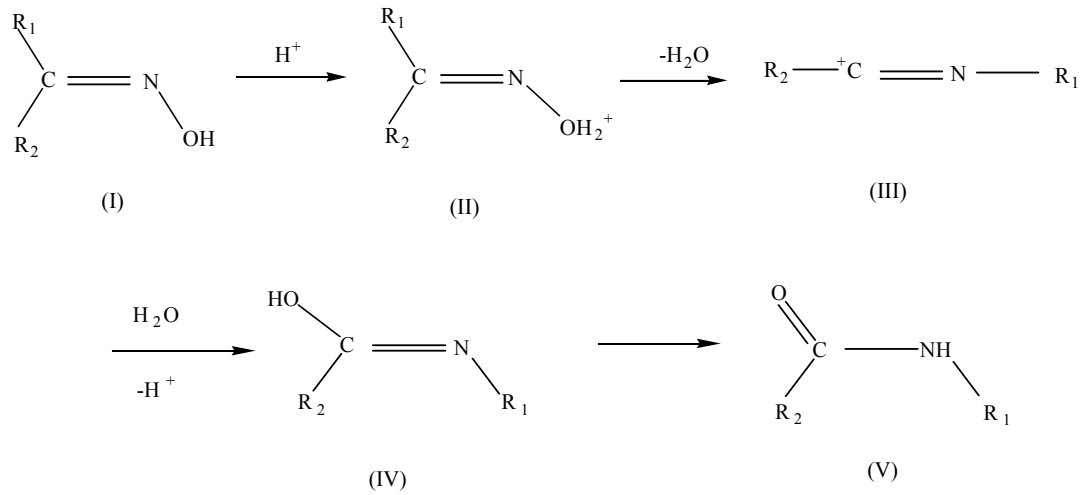

Scheme 1-6 Mechanism for the rearrangement of oxime (I) to amide (V)

Cyclohexanone, 2-cyclohexen-1-one, 5-hexenenitrile, aniline, 2-methylpyridine and hexanenitrile are commonly observed by-products in the Beckmann rearrangement of cyclohexanone oxime. Generally, it is accepted that Brønsted acid sites are the catalytic sites for the Beckmann rearrangement [105].

Various studies have been made on the Beckmann rearrangement reaction to replace sulfuric acid by solid acid catalysts. Under gas phase conditions silica-alumina [106], metal phosphate [107], boria-thoria [56], alumina supported-boria catalysts [51], zirconia supported-boria catalysts [60,58], and H-Y zeolite [108], ZSM-5 [109], etc. have been reported as active catalysts. However, side reactions, such as thermal decomposition and polymerization occur under gas-phase conditions. Furthermore, the catalytic activity decreased with time. The possibility of using solid acid catalysts for Beckmann rearrangement of cyclohexanone oxime in liquid phase has also been

investigated [110-112]. A series of zeolite beta has been applied to the liquid-phase Beckmann rearrangement [110,111]. Activity was observed for zeolite beta catalysts synthesized in OH^- media, with internal silanol groups but no framework Al. The selectivity was, however, dependent on the oxime; for cyclohexanone oxime, lactam selectivity was high, for cyclododecanone oxime it was low. Although many solid-acid catalysts have been reported for Beckmann rearrangement, their performance has been less than satisfactory level from the industrial standpoint and the heterogeneously catalyzed Beckmann rearrangement has yet to be commercialized.

1.8 Aims of the Project

In this project, the preparation of different solid acids is investigated. These include mesoporous materials with pores above 20 Å studied as catalysts and as supports. To induce acidity, aluminium was incorporated into the framework of silica, such as the formation of aluminium-MCM-41. MSU-type materials having both micro- and mesoporous features were prepared and its catalytic properties were compared with that of purely mesoporous and purely microporous materials. This project also explored the incorporation of silica into zirconia and the resulting acidity. Another form of solid acid was prepared by impregnating boron oxide on silica, zirconia, titania and alumina. $InCl_3$-impregnated onto zirconia was also investigated as solid acid. The solid acids were characterized for the surface area, pore volume, acidity, phase composition and catalytic activity.

Two catalytic reactions were chosen as test reactions. In one, the isomerization of α-pinene oxide was studied. The selectivity to campholenic aldehyde was compared amongst the different series of catalysts. This reaction depends on Lewis acidity. In

another test reaction, Beckmann rearrangement of cyclohexanone oxime into ε-caprolactam was investigated. In contrast to the α-pinene oxide isomerization, the rearrangement involves Brønsted acidity.

CHAPTER II

EXPERIMENTAL

2.1 Preparation of Catalysts

2.1.1 Synthesis of Hexagonal Aluminosilicate Mesoporous Materials (MSU-S)

Hexagonal aluminosilicate mesostructures were prepared from nanoclustered zeolite seeds that normally nucleate the crystallization of faujasitic zeolite type Y [32]. Hexagonal aluminosilicate mesostructure, (Si/Al = 70), denoted as MSU-S_{HY}(70) was prepared as follows. Nanoclustered zeolite Y seeds were prepared by reacting NaOH (0.029 mol, J.T. Baker, 98.6%) and $NaAlO_2$ (1.3×10^{-3} mol, Merck) in H_2O (0.85 mol) with silicate anions (0.09 mol) in the form of a sodium silicate solution containing 27 wt% SiO_2 and 10 wt% NaOH (Riedel-deHaen). The gel formed was stirred at room temperature for 1 h and heated under reflux condition with vigorous stirring at 100 ^oC overnight. Hexagonal MSU-S_{HY}(70) was formed by adding the zeolite seed solution to a solution of cetyl-trimethyl ammonium bromide (CTAB, Merck) template in water (0.02 mol in 12 mol of H_2O) at room temperature. The pH of the solution was lowered to approximately 9 by adding 5 M H_2SO_4 dropwise to the solution under stirring. The gel was then aged for another 1 h at room temperature before hydrothermal treatment for 48 h at 100 ^oC in Teflon-lined stainless steel autoclave. The product was washed with deionized water several times to remove the surfactant. The dried as-prepared sample was calcined at 540 ^oC for 10 h to remove the surfactant. The calcined catalyst was then ion exchanged with 1M NH_4NO_3 (Merck) solution at 100 ^oC under stirring overnight. The calcined product was filtered, washed, dried and finally calcined at 540 ^oC for 10 h to decompose the NH_4^+ to H^+.

Hexagonal aluminosilicate mesostructure, (Si/Al = 25 and 50), denoted as MSU-S_{HY}(25) and MSU-S_{HY}(50) respectively were prepared following the same procedure. The molar oxide ratio of the reactants is:

0.029 NaOH: 0.09 Na_2SiO_3: 3.6×10^{-3} $NaAlO_2$: 0.02 CTAB: 0.065 H_2SO_4: 10-20 H_2O

and

0.029 NaOH: 0.09 Na_2SiO_3: 1.8×10^{-3} $NaAlO_2$: 0.02 CTAB: 0.065 H_2SO_4: 10-20 H_2O,

respectively. Table 2-1 gives the weights of the components for the synthesized hexagonal aluminosilicate mesostructures.

Table 2-1 Synthesis of hexagonal aluminosilicate mesostrcutures from HY zeolite seeds.

Si/Al	NaOH/g	$NaAlO_2$/g	$Na_2Si_3O_7$/g	CTAB/g	H_2O/g
25	1.16	0.2952	20	7.3	231.3
50	1.16	0.1476	20	7.3	231.3
70	1.16	0.1066	20	7.3	231.3

Modification of MSU-S_{HY}(70) by Dealumination Process

A pretreatment of MSU-S_{HY}(70) with 0.01 M HCl at room temperature overnight, subsequent washing and calcination at 540 ^oC for 8 h produced dealuminated MSU-S_{HY}(70).

Synthesis of Aluminosilicate Mesostructures from Zeolite Beta Seeds, (MSU-S_{BEA})

For comparison purpose with MSU-S_{HY}, MSU-S_{BEA} (Si/Al = 67) was prepared. MSU-$S_{(BEA)}$ (Si/Al = 67) denoted as MSU-S_{BEA}(67), was prepared according to the method described by Pinnavaia et al. [33]. First the beta seeds were prepared by the reaction of 1.0 M tetraethylammonium (TEA) hydroxide (Fluka,~40% in water), sodium aluminate (0.5 mmol, Merck), and fumed silica (33.3 mmol, Aerosil 200, Degussa) in water (1270 mmol) at 100 ^{o}C for 18 h. MSU-S_{BEA}(67) mesostructures were assembled by reaction of the beta seed solution with cetyltrimethylammonium bromide (CTAB, 8.65 mmol, Merck) at 150 ^{o}C for 48 h in a Teflon-lined stainless steel autoclave. The product was washed with deionized water for several times and dried at 100 ^{o}C overnight. Finally, the dried product was calcined at 550 ^{o}C for 10 h to remove the surfactant. The calcined catalyst was then ion exchanged with 1M NH_4NO_3 (Merck), dried and finally calcined at 550 ^{o}C for 10 h.

Synthesis of Al-MCM-41

AI-MCM-41 (Si/Al = 70) denoted as Al-MCM-41 (70) was prepared following reference [113]. 0.1438 g of Al-isopropoxide (98%, Aldrich) was dissolved in 10 g of H_2O and 2.9577 g of fumed silica (Aerosil 200, Degussa) was added to the solution. In a separate beaker, 3.4974 g of TEAOH solution (Fluka, ~40% in water), 4.92 g cetyltrimethylammonium bromide (CTAB, Merck) and 34 g of H_2O were mixed and gently heated until a clear solution was obtained. The solution was added to the silica-alumina solution with stirring. The final mixture was stirred for another 2 h at room temperature and aged at room temperature for 24 h. The final gel composition was:

0.0141 Al: 0.9859 Si: 0.19 TEAOH: 0.27 CTAB: 40 H_2O. Finally the mixture was reacted for 48 h at 150 ^oC in Teflon-lined stainless steel autoclave. The product was filtered, washed with deionized water, and dried at 70 ^oC overnight and calcined at 550 ^oC for 10 h.

2.1.2 Synthesis of Boron Oxide Supported on Metal Oxides

Silica-supported boron oxide catalysts were prepared as follows: 1 g of silica (silica gel 60, Merck) was calcined in air for 8 h at 500 ^oC. It was then impregnated with 0.0975, 0.1965, 0.2925, 0.3898 and 0.7796 g of boric acid (Riedel-deHaen) dissolved in warm deionized water to give 5, 10, 15, 20 and 40 wt.% nominal boron oxide loading, respectively. After stirring gently for 2 h, the excess water was evaporated off and the slurry was dried overnight at 120 ^0C. The catalysts were calcined at 350 ^oC for 8 h in air.

For comparison purpose, 15 wt.% boron oxide on TiO_2 (Titandioxide P25, Degussa), Al_2O_3 (γ- Al_2O_3, Merck) and ZrO_2 were similarly prepared.

2.1.3 Preparation of SiO_2/ZrO_2 Catalyst using Silica Glass and Quartz Chips

Hydrous zirconia was prepared by the hydrolysis of zirconium chloride (Merck) in excess 5 M NH_4OH (Fisher) [114]. 10 wt.% $ZrCl_4$ solution was added dropwise via a peristaltic pump to 5 M NH_3 solution. A white gelatinous precipitate of hydrous zirconia was formed. The pH of the final gel solution was adjusted to 9.5 by adding concentrated NH_4OH dropwise. One portion of the precipitate (0 h) was immediately removed and thoroughly washed with dilute ammonium nitrate (Merck) until free of chloride and dried at 100 ^oC overnight. The sample was denoted as 0-100. Half of the

0-100 sample was calcined at 500 ^{o}C in air for 12 h to convert it to zirconia and the calcined sample was named as 0-500. The remaining hydrous zirconia was divided into two portions and placed into two Teflon round-bottomed flasks. Silica glass chips were added to one flask and quartz chips were added to the second sample. Each sample was then digested under open reflux at 100 ^{o}C for 1, 2, 4, and 8 days.

After the respective digestion time, the solids were recovered, washed free of chloride and dried overnight at 100 ^{o}C. The hydrous oxides were then calcined at 500 ^{o}C in air for 12 h to convert them to zirconia (heating rate 1 ^{o}C/min).

The samples were coded as follows: Q-D-T and G-D-T, where Q = quartz, G =glass, D = digestion time in days, T = calcination temperature.

2.1.4 Synthesis of $InCl_3$-Supported on ZrO_2 and $Zr(OH)_4$ Catalysts

2 mmol $InCl_3$/g $Zr(OH)_4$ was prepared by incipient wetness technique as follows: 1 g of $Zr(OH)_4$ was added to a solution containing 0.4424 g of $InCl_3$ (Riedel-deHaen). Then 2 drops of conc. HCl (37% fuming, Merck) was added to this solution and stirred gently for 2 h and the excess water was evaporated at 60 ^{o}C. Finally the catalyst was dried overnight at 120 ^{0}C. $Zr(OH)_4$ was prepared according to the method stated in section 2.1.3. 0.25, 0.5, 1 and 4 mmol $InCl_3$/g $Zr(OH)_4$ were prepared by impregnating the appropriate amount of $InCl_3$ with 1 g of $Zr(OH)_4$.

A sample containing 2 mmol $InCl_3$/g ZrO_2 was prepared in a similar manner. The supported zirconia was formed by calcining silica-free hydrous zirconia for 8 h at 500 ^{o}C.

2.1.5 Synthesis of Phosphated Zirconia [115]

1 g of ZrO_2 was added to a solution of $(NH_4)_2HPO_4$ (99%, Fluka) (0.1530 g in 10 ml of H_2O). The suspension was then left for 1 h and subsequently dried by evaporation of the water. Finally, the dried phosphated material was calcined at 550 ^oC for 6 h to produce 10 wt.% PO_4^{-3}/ZrO_2 catalyst.

2.1.6 Synthesis of Zirconia-Supported Tungsten Oxide Catalyst

20 wt.% WO_3/ZrO_2 was prepared following reference [116]. 1.293 g of $Zr(OH)_4$ was added to ammonium tungstate (para, 99%, Fluka) solution, (0.278 g in 10 ml of H_2O) and subsequently dried by evaporation of water. Finally, the dried product was calcined at 500 ^oC for 6 h to obtain the catalyst.

2.2 Catalyst Characterization

A number of techniques were used to characterize the prepared catalysts. These include powder X-ray powder diffraction (XRD), surface area, pore volume, solid state nuclear magnetic resonance (NMR), pyridine infrared spectroscopy (IR), and ICP-AES for elemental analysis.

2.2.1 X-Ray Powder Diffraction

The powder diffraction pattern is the fingerprint of any crystalline phase and powder diffraction is used extensively to identify the mixture of phases which generally constitutes a catalyst. Powder diffraction patterns are obtained by measuring the angles at which an X-ray beam of wavelength, λ, is diffracted by the sample. The position, intensity, shape and width of the diffraction lines give information of the sample. The spacing between two planes (*hkl*), *d*, is related to the diffraction angle 2θ by the Bragg's law:

$$\lambda = 2d \sin \theta \tag{1}$$

For crystals of the cubic system, the unit cell dimension, *a*, is related to *d*, by

$$d = \frac{a}{\sqrt{h^2 + k^2 + l^2}} = \frac{a}{M} \tag{2}$$

where *h, k, l* are Miller indices and

$$M^2 = h^2 + k^2 + l^2 \tag{3}$$

Combining equations (1) and (2),

$$\sin^2 \theta = \frac{\lambda^2}{4a^2}(h^2 + k^2 + l^2) = A(h^2 + k^2 + l^2) \tag{4}$$

For the hexagonal structure, the unit cell parameter, a_o, can be calculated using equation (5).

$$a_0 = \frac{2d_{100}}{\sqrt{3}} \tag{5}$$

By using Bragg's equation (1), the interplanar distance, *d*, can be calculated.

The crystallite size can be calculated by using the Debye-Scherrer equation.

$$D_{crystal}\ (Å) = \frac{k\lambda}{\beta \cos\theta} \qquad (6)$$

where λ = wave length, and

$$\beta = \sqrt{B^2 - b^2} \qquad (7)$$

B = peak width at half maximum (in rad)

b = instrumental broadening (in rad)

The crystallinity and phase purity of the solids were determined by powder X-ray using a Siemens D5005 diffractometer with Cu-Kα radiation at 40 kV and 40 mA. Temperature dependent measurements were carried out using D8 ADVANCE diffractometer. The scanning range for 2θ is normally 5^o to $70^{o;}$ for MCM-41 and MSU-materials, the range was from 1.5^o to 12^o. The step size used was 0.02^o.

2.2.2 BET Surface Area and Porosity Determination

Most catalysts are highly porous resulting in a higher surface area. The determination of surface area is an important requirement in catalyst characterization.

BET Surface Area Determination

The Brunauer-Emmett-Teller (BET) method is the most widely used procedure for the determination of surface area of solid materials. There are two stages in the application of the BET procedure. First, it is necessary to derive the *monolayer capacity*, n_m^a defined as the amount of adsorbate required to form a complete

monolayer on the surface of unit mass of the adsorbent. The *specific surface area*, a_s (BET), is then obtained from n_m^a by taking a value for the average area, a_m, occupied by the adsorbate molecule in the monolayer. Thus

$$a_s\,(\mathrm{BET}) = n_m^a \times \mathrm{L} \times a_m \tag{8}$$

where L is the Avogadro constant.

The simplified BET equation using for the determination of surface area is,

$$\frac{P/P_0}{n^a(1-P/P_0)} = \frac{1}{n_m^a C} + \frac{C-1}{n_m^a C}\frac{P}{P_0} \tag{9}$$

where n^a is the weight of gas adsorbed at a relative pressure P/P_0. The term C, the BET constant, is related to the energy of adsorption in the first adsorbed layer and consequently its value is an indication of the magnitude of the adsorbent/adsorbate interactions.

Nitrogen (at 77 K) is generally considered to be the most suitable adsorbate for the determination of the surface area of nonporous, macroporous, or mesoporous solids. It is usually assumed that the BET nitrogen monolayer is closed packed. The surface area is measured by determining the quantity of gas that adsorbs as a single layer of molecules on a sample. This adsorption is done near the boiling point of the adsorbate gas. Under specific condition, the area covered by each gas molecule is known within relatively narrow limits. The surface area is thus directly calculable from the number of adsorbed molecules, which is derived from the gas quantity at the prescribed conditions, and the area occupied by each molecule.

Porosity by Gas Adsorption

According to the IUPAC definition of porosity, is the ratio of pore volume to apparent volume of particle or granule. The pores are classified as follows:

(a) Micropore Pore of width less than 2 nm

(b) Mesopore Pore of width between 2 and 50 nm

(c) Macropore Pore of width greater than 50 nm

The understanding of the surface area and porosity of an adsorbent can be achieved by the construction of an adsorption isotherm. The adsorption isotherm is the relationship between the amount adsorbed and the equilibrium pressure (or relative pressure) at a known temperature. Similarly the desorption isotherm is the relationship between the amount of gas desorbed and the equilibrium pressure at a known temperature. All adsorption isotherms may be grouped into one of the five types shown in Scheme 2-1. The reversible Type-I isotherm exhibits a distinctive plateau so that n approaches a limiting value as P/P_0 becomes 1. Type-I isotherms are given by microporous catalysts such as molecular sieve zeolites and many activated carbon supports. Type-II is also reversible, and it is the normal form of isotherm given by a nonporous or macroporous adsorbent. The shape is indicative of unrestricted monolayer-multilayer adsorption up to high P/P_0. Type-III is rarely encountered and it is also reversible.

Isotherms like Type-IV are given by mesoporous adsorbents such as silica gels and some other oxide catalysts and supports. Type-V isotherms are uncommon, corresponding to Type-III, except that pores in the mesopore range are present. Type IV and V, associated with mesoporosity, usually exhibit hysteresis between the adsorption and desorption isotherms.

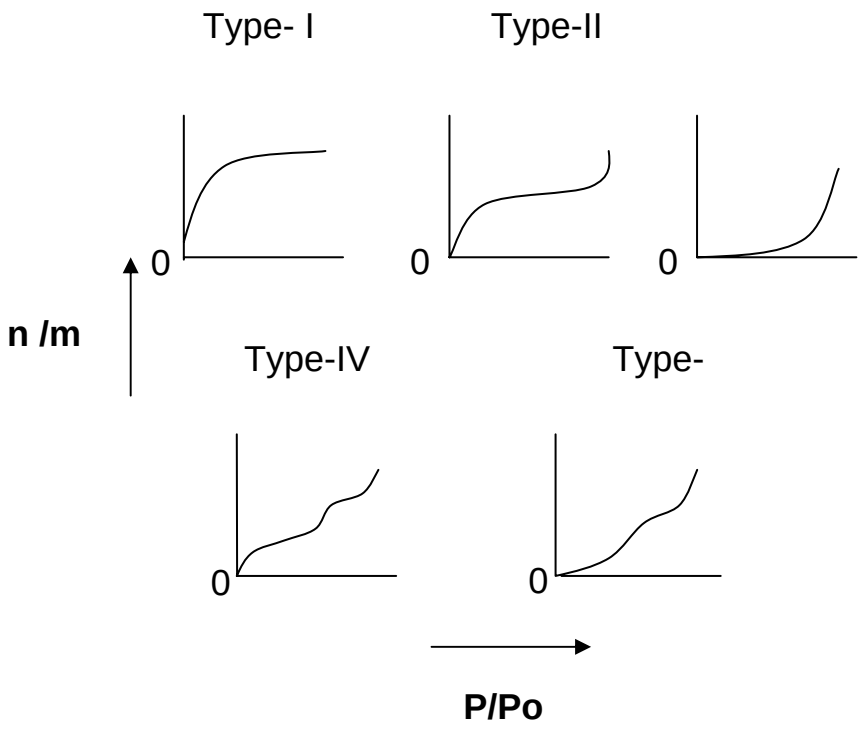

Scheme 2-1 Adsorption isotherms: n = amount of adsorbed, m = mass of solid adsorbent, P = equilibrium pressure, P_0 = saturation vapour pressure.

De Boer has identified five types of hysteresis loops and correlated them with various pore shapes (Scheme 2-2). Type A hysteresis is attributed to cylindrical pores; Type B is associated with slit shaped pores; Type C hysteresis is produced by wedge-shaped with open necks at one or both open ends. Type D loops result from wedge-shaped pores with narrow necks at one or both ends. The type E hysteresis loop has been attributed to "ink-bottle" pores. Characteristically, the hysteresis loops in all isotherms close before reaching a relative pressure of 0.3 in the desorption process except when microporosity is present. The distribution of pore volume with respect to pore size is called a pore size distribution. It is generally accepted that the desorption isotherm is

more appropriate than the adsorption isotherm for evaluating the pore size distribution of an adsorbent due to the attainment of thermodynamic equilibrium.

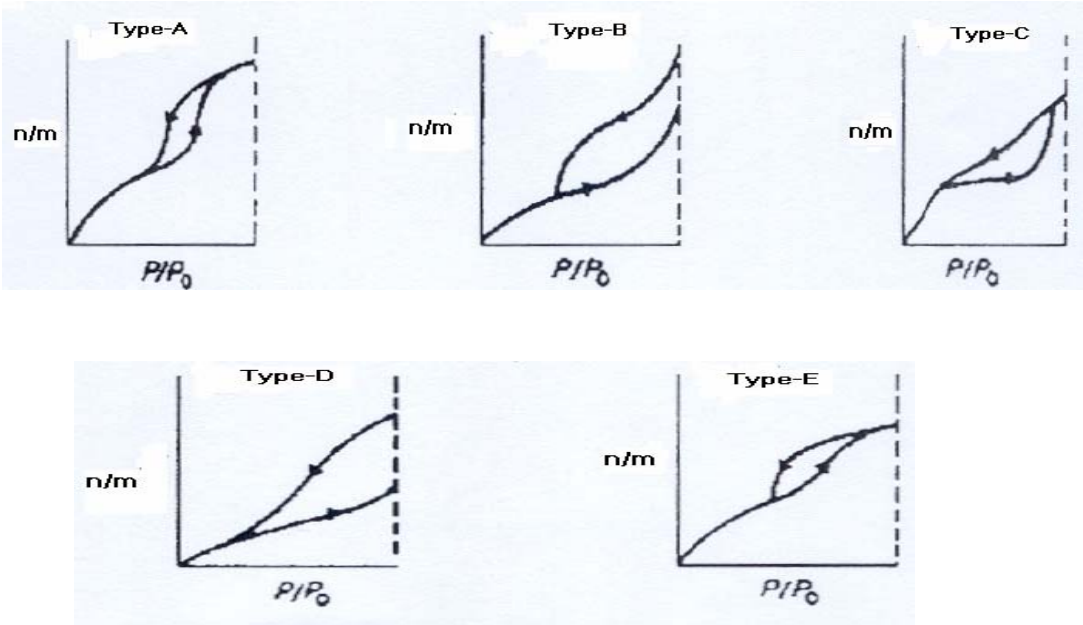

Scheme 2-2 De Boer's five types of hysteresis

According to the IUPAC classification of physisorption hysteresis loops (Scheme 2-3), Type-H1 is representative of an adsorbent with a narrow distribution of relatively uniform mesopores, whereas Type-H2 is associated with a more complex pore structure in which network effects are important. Type-H2 loops are given by adsorbents containing narrow slits-shaped pores such as activated carbons. Type-H3 and H4 do not exhibit any limiting adsorption at high relative pressure. This is clear indication that the adsorbents do not possess well-defined mesopore structures and therefore it is not possible to attempt to derive either the pore size distribution or the total pore volume from these isotherms. Type-H3 loops are often obtained with plate like materials such as clays. A particular feature of many hysteresis loops (Types-H2,

H3, and H4) is the very steep region of the desorption branch which leads to a lower closure point of the loop at a constant P/Po for a given adsorbate and temperature (e.g. P/Po = 0.42 for nitrogen at 77 K). This feature is thus dependent on the nature of the adsorbate rather than the distribution of pore size.

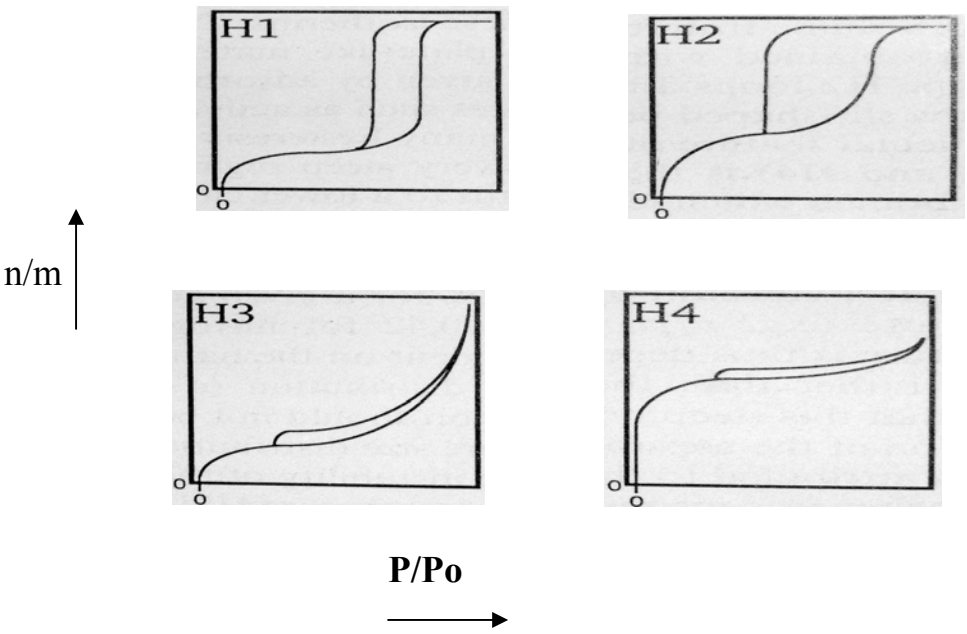

Scheme 2-3 Possible hysteresis loops for mesoporous materials.

2.2.3 Pyridine Adsorption IR

The pyridine adsorption IR method is widely used to investigate the nature of acid sites. To determine the acidity and type of acid sites, IR pyridine adsorption measurements were carried out. The sample was pressed into a thin self-supporting disk of ~ 10 mm diameter. It was placed in a Pyrex cell with NaCl windows and degassed at 300 ^{o}C for 2 h under vacuum. After cooling down to room temperature, an IR spectrum of the pellet was measured. The sample was then dosed with pyridine

at 22 mbar for 15 minutes and evacuated at room temperature for 1 h before another IR spectrum was recorded. The difference spectrum of two measurements gives the pyridine adsorption of the sample. Subsequently, the sample was heated in vacuum at 100 ^{o}C and 200 ^{o}C for 1 h at each temperature cooled to room temperature before measuring the IR spectra. A Biorad spectrometer was used for recording the spectra at a resolution of 2 cm^{-1} and 32 scans were averaged.

According to Emies [117], the molar extinction coefficient of the band at 1545 cm^{-1} due to pyridine on a Brønsted acid site is 1.67 cm/μmol and for the band at 1455 cm^{-1} due to co-ordinately bonded pyridine on a Lewis acid site is 2.22 cm/ μmol. Hence, the relative ratio of Brønsted to Lewis acid sites (B/L) given by following equation.

$$\frac{B}{L} = \frac{IA(B) / 1.67}{IA(L) / 2.22} \qquad (10)$$

where *IA(B,L)* is integrated absorbance of B or L band (cm^{-1})

2.2.4 Solid State Nuclear Magnetic Resonance (NMR) Spectroscopy

Since its discovery in the 1940s, nuclear magnetic resonance (NMR) spectroscopy has become one of the most powerful tools for investigating structure and dynamics of molecular systems. Until the late 1970s, however, the applications of high resolution NMR spectroscopy in chemistry was restricted to liquids but with the introduction of novel sophisticated solid-state NMR it become possible to measure NMR spectra of solids with high resolution.

Fundamentals of NMR Spectroscopy [118]

Atomic nuclei which contain an odd number of protons and/or neutrons possess a nuclear spin $I \neq 0$ and consequently a magnetic moment $\mu = \gamma\hbar I$, where γ, the gyromagnetic ratio, is a specific constant for each type of nucleus. When placed in an external magnetic field B_o, the Zeeman interaction results in quantized orientations of the nuclear magnetic moments, and the nucleus can adopt $2I + 1$ magnetic energies with energies $E(m) = -m\gamma\hbar B_o$, where $m = (I, I-1, \ldots, -I)$. Transition between neighboring energy states ($\Delta m = \pm 1$) can be induced by electromagnetic radiation of energy $E = h\nu$. In condensed matter each nucleus is exposed to specific interactions with other nuclei and the electric field of surrounding electrons, and the total magnetic field B_{tot}, experienced by the nucleus is the sum of the external field, B_o, and the internal component, $B_{int.}$ The absorption of energy from the irradiated radiofrequency field in the sample stimulates the transition between the energy states.

The dominant structure-dependent interactions which contribute to the shape and position of the NMR lines of solid are

(i) dipolar interaction

(ii) chemical shift interactions

(iii) quadrupolar interactions for nucleus with $I > ½$

For the measurement of highly resolved NMR spectra of powders with individual resonance lines for inequivalent nuclei, special techniques have to be applied to remove or to reduce substantially the line broadening effects. The most important techniques for line narrowing are

(i) dipolar decoupling

(ii) magnetic-angle spinning (MAS)

(iii) double oriented rotation (DOR)

^{29}Si-MAS NMR

Silicates are characterized by the tetrahedral anion $(SiO_4)^{4-}$, labeled Q, with various degrees of condensation. The chemical shift of the central ^{29}Si varies from -60 to -120 ppm relative to TMS. Typical shift ranges for the four Si(nAl) environments have been established from a large body of shift data measured in various types of zeolites and other framework silicates (Scheme 2-4) [119]. $Si(OSi)_{4-n}(OAl)_n$ with n = 0-4, conventionally designated as "Si(nAl)"

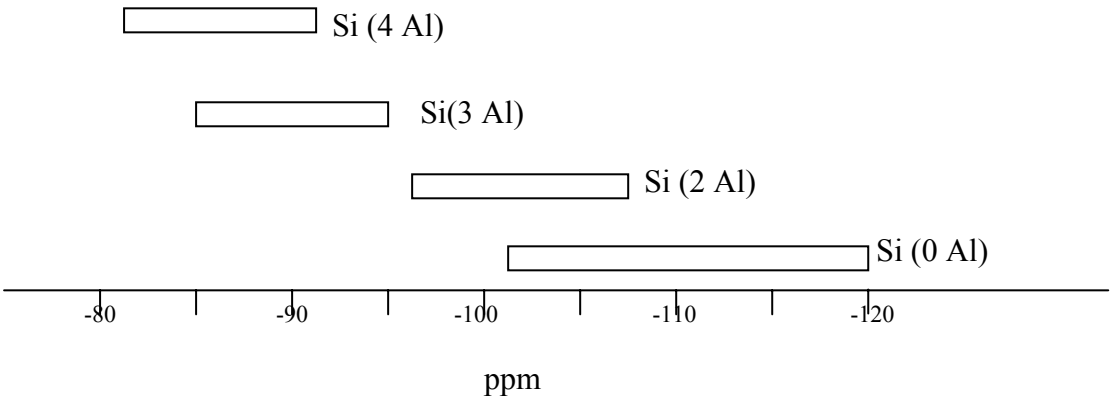

Scheme 2-4 Ranges of ^{29}Si chemical shifts of Si(nAl) units in zeolites [119].

^{27}Al-MAS NMR

The ^{27}Al chemical shift is governed primarily by the aluminum co-ordination. The octahedral aluminum chemical shift span ranges from 0-22 ppm relative to $[Al(H_2O)_6]^{3+}$, whereas the chemical shift span for tetrahedral aluminum is within 50-

80 ppm relative to the same reference. The value of chemical shift also varies with the second neighbors.

^{11}B-MAS NMR

In amorphous crystalline compounds boron may exists both as tetrahedral and trigonal units. Tetrahedral boron exhibits a narrow signal whereas trigonal boron is characterized by a broad highly anisotropic signal. Normally the chemical shifts are measured relative to BF_3 etherate as a reference from -50 ppm to 50 ppm.

The MAS NMR spectra were recorded on a Bruker DRX-400 spectrometer with 4 mm cylindrical zirconia rotors at a spinning rate of 12 kHz. The ^{27}Al-MAS NMR spectra were obtained at 104.26 MHz with an excitation pulse of 1.7 μs and a recycle delay of 5 s. Chemical shifts were measured relative to aqueous $Al(NO_3)_3$. The ^{29}Si-MAS NMR spectra were recorded at 79.5 MHz using 3.0 μs pulse with repetition time of 20 s. Chemical shifts were measured relative to sodium 3-(trimethylsilyl)-1-propanesulfonate. The ^{11}B-MAS NMR was recorded at 128.4 MHz using 8^o rf pulses, 1 s recycle delay, while the MAS spinner was rotated at a rate of 12 kHz. Chemical shifts were recorded relative to BF_3 etherate.

2.3 Catalytic Activity Tests

2.3.1 α-Pinene Oxide Isomerization Reaction

1.5 g of α-pinene oxide (Aldrich, purity 97 %) and 6 g of toluene (J.T.Baker) were placed into a round bottomed flask equipped with guard tube. The catalyst was first dried at 100 ^{o}C before adding 0.15 g to the reaction mixture. An internal standard, m-xylene, was used. The reaction mixture was stirred by magnetic stirrer and the

reaction temperature was varied from 0 ^{o}C to 50 ^{o}C. Aliquots were extracted at regular time intervals and analyzed by GC (HP 6890, 5% phenyl methyl siloxane 30.0m×320μm×0.25μm, FID). The products were identified by verification with authentic samples and by GC-MS (Shimadzu GCMS-QP5000, capillary column: DB5MS, 30m). A typical chromatogram is shown in Fig. 2-1. The GC conditions for the analysis were: initial temperature 60 ^{o}C, holding time 2 min, final temperature 200 ^{o}C , holding time 2 min and ramp 20 ^{o}C/min.

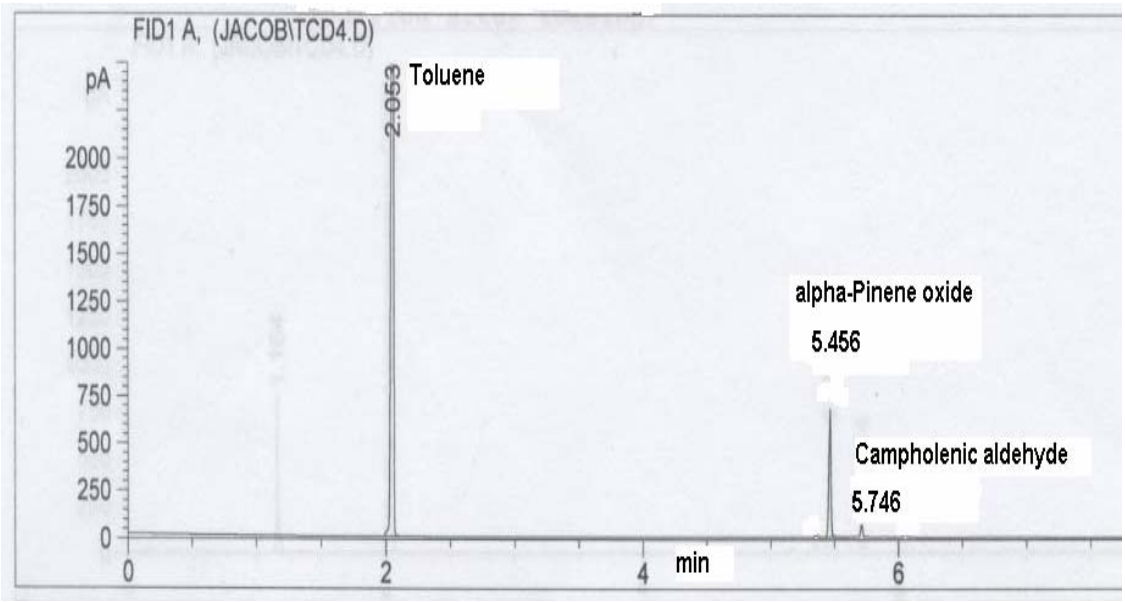

Fig. 2-1 Gas chromatogram of 97% pure α-pinene oxide dissolved in toluene.

Since the starting material was only 97% pure, a small amount of campholenic aldehyde was detected with aldehyde/ α-pinene oxide ratio equal to 0.04 (Fig. 2-1). This ratio was taken into account when calculating the conversion and selectivity. The selectivity and the conversion were calculated as follows:

$$\frac{[CA_o]}{[PO_o]} = 0.04 \qquad (11)$$

where $[CA_o]$ = Initial concentration of campholenic aldehyde

$[PO_o]$ = Initial concentration of α-pinene oxide.

$$\% \text{ Conversion} = \frac{([CA_t]-[CA_o])+[I_t]}{([CA_t]-[CA_o])+[PO_t]+[I_t]} \times 100 \quad (12)$$

where $[CA_t]$ = concentration of campholenic aldehyde after reaction time t

$[PO_t]$ = concentration of α-pinene oxide after reaction time t

$[I_t]$ = concentration of all other isomers after reaction time t

However,

$$[CA_o] = 0.04([PO_t]+[CA_t]-[CA_o]+[I_t]) \quad (13)$$

From equation (13)

$$[CA_o] = 0.038([PO_t]+[CA_t]+[I_t]) \quad (14)$$

Therefore,

$$[CA_t]-[CA_o] = [CA_t]-0.038([PO_t]+[CA_t]+[I_t]) \quad (15)$$

From equation (15)

$$[CA_t]-[CA_o] = 0.962[CA_t]-0.038([PO_t]+[I_t]) \quad (16)$$

From equation (12) and (16)

$$\% \text{ Conversion} = \frac{0.962[CA_t]-0.038([PO_t]+[I_t])+[I_t]}{0.962([CA_t]+[PO_t]+[I_t])} \times 100 \quad (17)$$

$$\% \text{ Selectivity} = \frac{[CA_t]-[CA_o]}{([CA_t]-[CA_o]+[I_t])} \times 100 \quad (18)$$

where $[I_t]$ = concentration of other by-products after reaction time t

From equations (16) and (18),

$$\% \text{ Selectivity} = \frac{0.962[CA_t]-0.038([PO_t]+[I_t]}{[0.962([CA_t]+[I_t])-0.038[PO_t]}] \times 100 \quad (19)$$

2.3.2 Liquid-Phase Beckmann Rearrangement of Cyclohexanone Oxime

0.1g cyclohexanone oxime (97%, Fluka) was dissolved in 20 ml of solvent and the reaction mixture was heated to the reaction temperature and allowed to equilibrate at the set temperature. 0.1 g of dried catalyst was added to the cyclohexanone oxime solution. Aliquots were extracted at regular time intervals and analyzed by GC (HP 6890, 5% phenyl methyl siloxane 30.0m×320μm×0.25μm, FD). The temperature range for the analysis was 60 ^{o}C to 200 ^{o}C with 2 min initial holding time and the ramp was 20 ^{o}C/min.

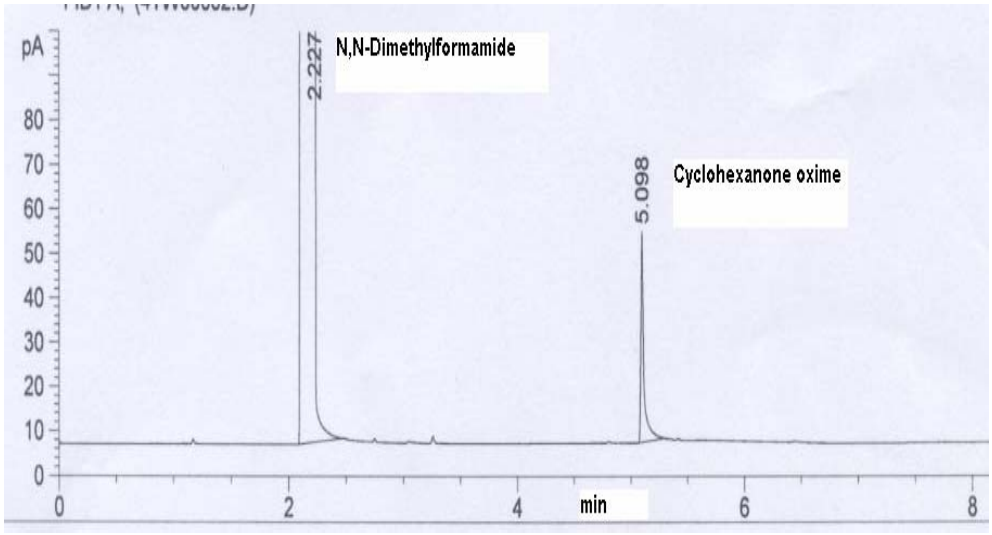

Fig. 2-2 Gas Chromatogram of cyclohexanone oxime dissolved in N,N-dimethylformamide.

The products were identified by verification with authentic samples and by GC-MS (Shimadzu GCMS-QP5000, capillary column: DB5MS, 30m). A typical chromatogram of pure cyclohexanone oxime is shown in Fig. 2-2.

The rearrangement was also studied using a homogeneous catalyst, P_2O_5 [120]. A 25 ml round-bottomed flask was purged with nitrogen. A solution of 4.5 ml N,N-dimethylformamide and 0.035 g of P_2O_5 was then placed in the flask. The resulting mixture was heated 100 ^{0}C. Finally, a solution of 0.8 g cyclohexanone oxime in 4.5 ml of N, N-dimethylformamide was added to the mixture at 100 ^{o}C. The reaction was continued for 2.5 h. A small amount of alkali (NaOH) was then added to the reaction mixture to deactivate the catalyst. The reaction mixture was analyzed by GC (Fig. 2-3).

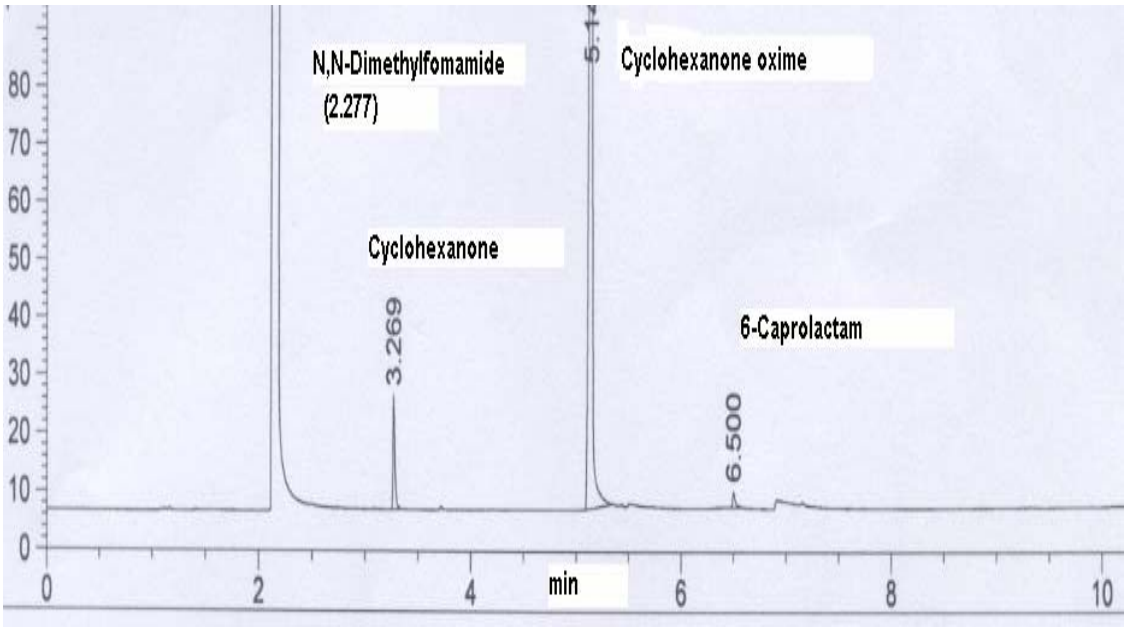

Fig. 2-3 Gas chromatogram of Beckmann rearrangement of cyclohexanone oxime over P_2O_5 in N,N-dimethylformamide at 100 ^{o}C after 2.5 h.

CHAPTER III

Results and Discussion

PHYSICAL PROPERTIES OF SYNTHESIZED CATALYSTS

3.1 MSU-S Type Mesoporous Materials

3.1.1 X-Ray Diffraction

The low angle X-ray diffraction (XRD) patterns for the calcined samples of MSU-S_{HY} (Si/Al = 25, 50, and 70) exhibited three well resolved peaks (Fig.3-1). They can be indexed as (100), (110), and (200) reflections associated with the hexagonal symmetry [20]. With increase of Al content, the intensity of these three peaks decreased indicating lattice imperfections [121]. At the same time, the peak width broadened showing that smaller crystallites are formed (Table 3-1). The peak positions also shifted towards higher 2θ values with increase of Al content, resulting in the d_{100} spacing changing from 41.26 Å to 37.75 Å. After HCl-treatment of MSU-S_{HY}(70), the intensity of the (100) reflex was unchanged but the peak was slightly shifted to higher 2θ value. The d_{100} spacing decreased from 41.26 Å to 40.50 Å after acid treatment. A wide-angle scan from 2θ of 1.5^o to 40^o showed that there was no zeolitic phase present (Fig. 3-3 and 3-4). The XRD patterns for MSU-S_{BEA}(67) and Al-MCM-41(70) were also well resolved with diffraction peaks of (100), (110) and (200) reflexes (Fig. 3-2). The a_o value for MSU-S_{BEA}(67) and Al-MCM-41(70) are both higher than those of MSU-S_{HY}.

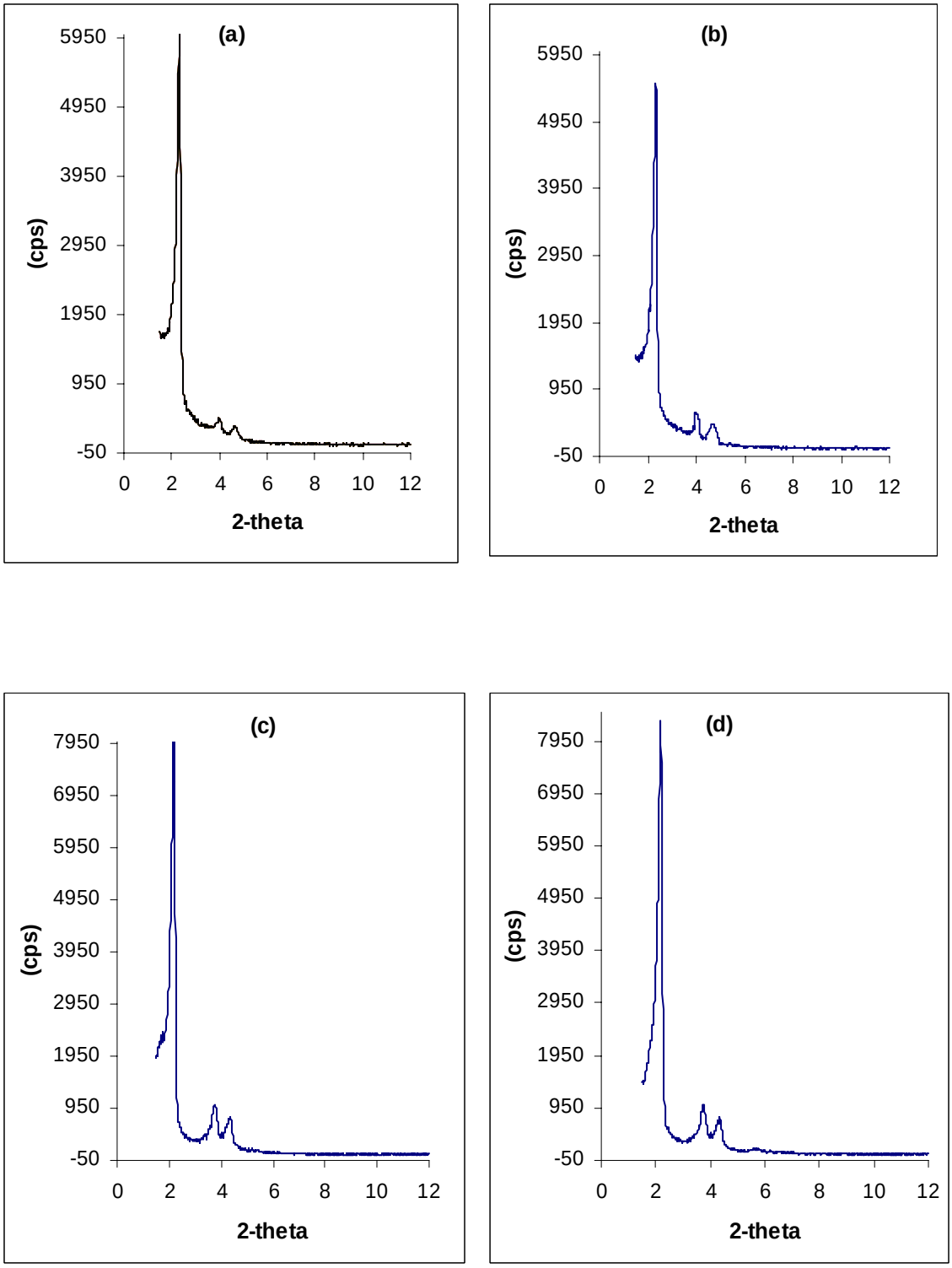

Fig. 3-1 XRD diffraction patterns of calcined (a) MSU-S_{HY}(25), (b) MSU-S_{HY}(50), (c) HCl- treated MSU-S_{HY}(70) and (d) MSU-S_{HY}(70).

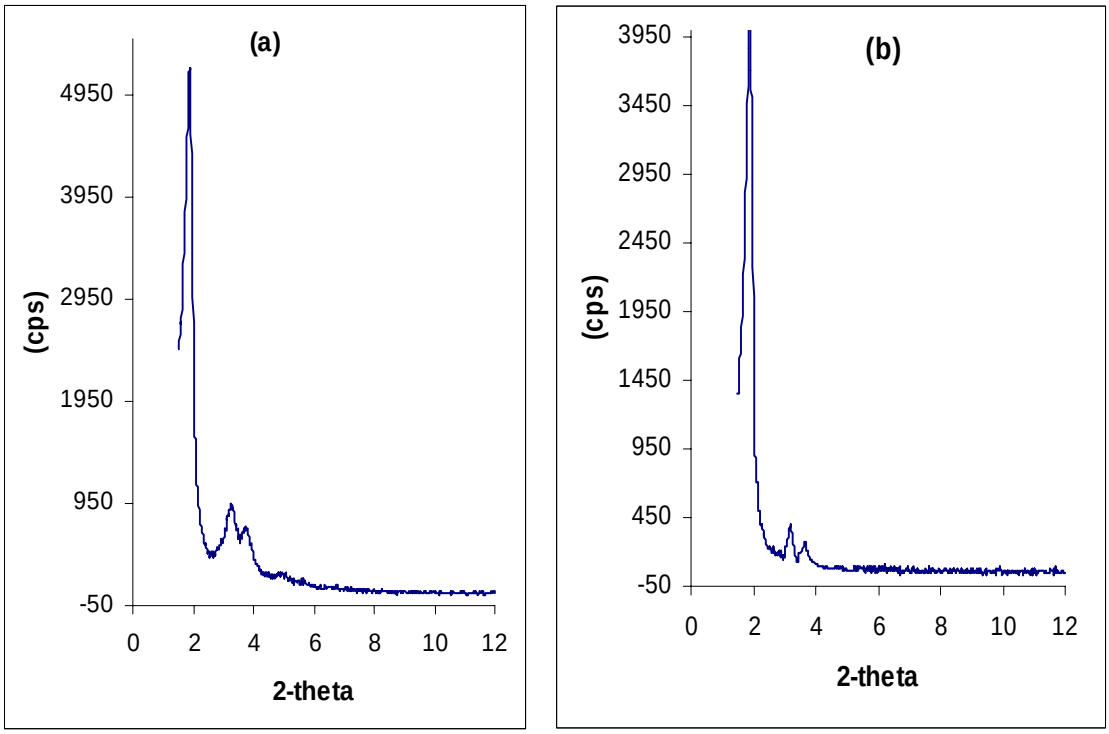

Fig. 3-2 XRD diffraction patterns of calcined (a) MSU-S_{BEA}(67) and (b) Al-MCM-41(70)

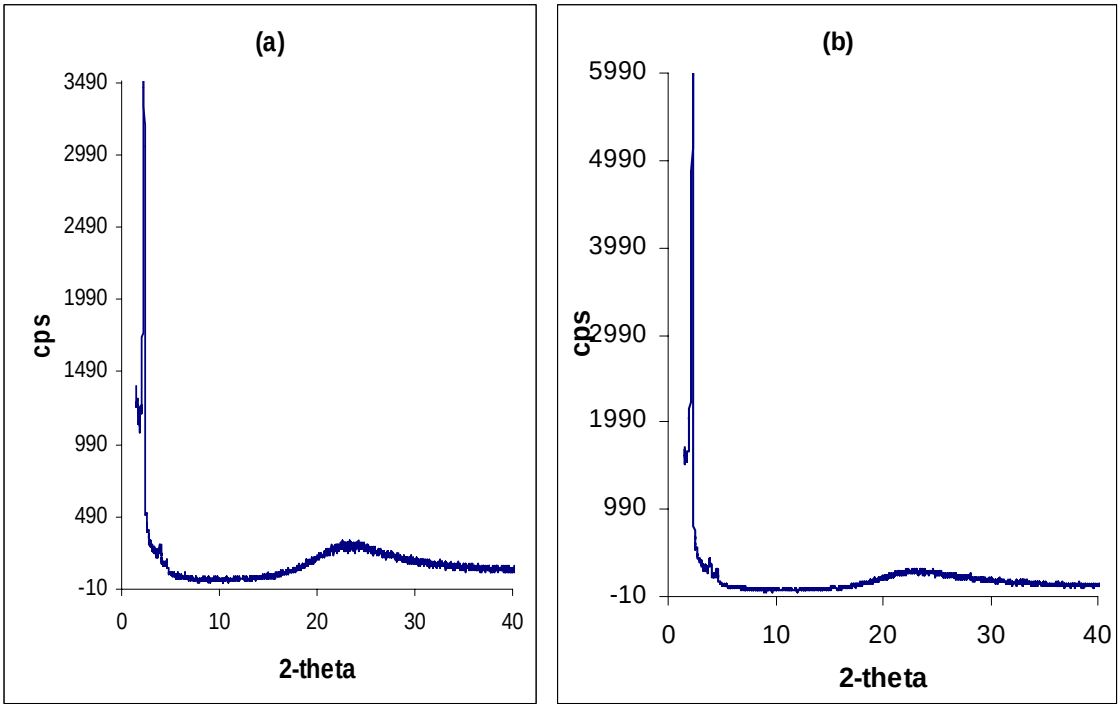

Fig. 3-3 Wide-angle XRD patterns of calcined (a) MSU-S_{HY}(25), (b)MSU-S_{HY}(50)

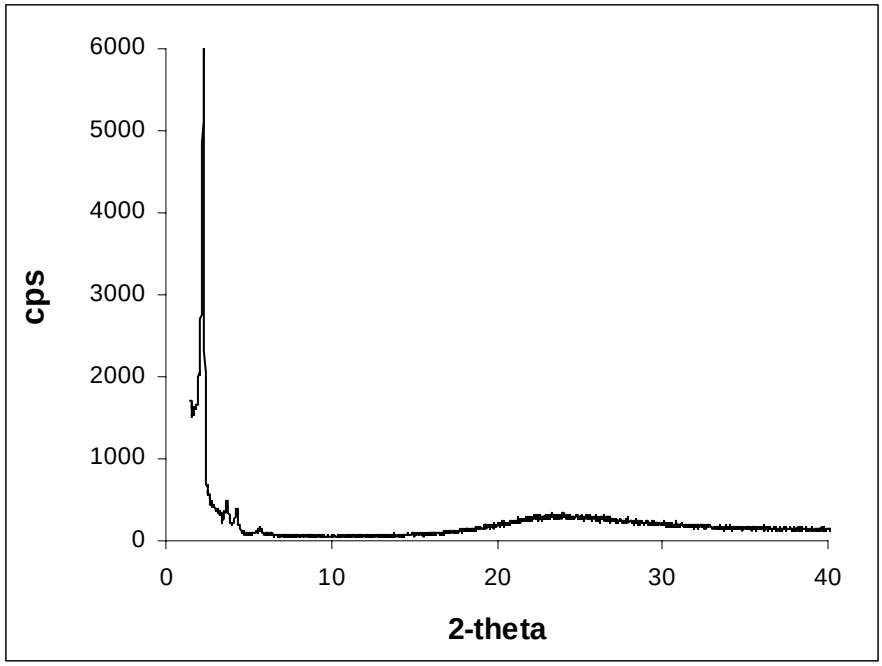

Fig. 3-4 Wide-angle XRD pattern of calcined MSU-S_{HY}(70)

Table 3-1 XRD data of MSU-S samples and Al-MCM-41(70)

	MSU-S_{HY}(25)	MSU-S_{HY}(50)	MSU-S_{HY}(70)	MSU-S_{HY}(70)[a]	MSU-S_{BEA}(67)	Al-MCM-41(70)
2θ (100)	2.34°	2.33°	2.14°	2.18°	1.90°	1.86°
d_{100}/Å	37.75	37.89	41.26	40.50	46.47	47.47
a_o/Å	43.57	43.76	47.63	46.77	53.65	54.81

a = HCl-treated

3.1.2 BET Surface Area and Pore Volume

Figs. 3-5–3-10 show N_2 adsorption /desorption isotherms and pore size distribution curves of synthesized mesoporous materials. MSU-S_{HY}(25) exhibited a steep rise at low relative pressure ($P/P_o < 0.1$) indicating presence of micropores structures. A well-defined capillary condensation step was observed at $P/P_o \sim 0.2$-0.3. No hysteresis was observed in this region, indicating that N_2 sorption within the framework

confined pores was reversible. The shape of this isotherm shows that MSU-S_{HY}(25) contains larger mesopores, of irregular or bottlenecked pores. The pore size distribution of MSU-S_{HY}(25) showed that the framework-confined pores, as described by the low pressure capillary condensation step, had a mean pore diameter of 23 Å while the larger mesopores were ~37 Å in size. The N_2 adsorption/desorption isotherm and pore size distribution curve of MSU-S_{HY}(50) were also similar to MSU-S_{HY}(25) although there was a shift to bigger pore sizes. In MSU-S_{HY}(70), the low-pressure capillary step was very pronounced and the framework-confined pores constitute the greater fraction of pore in this material (Fig. 3-7). The mesoporous pore volume was 1.00 cc/g as compared to 0.80 and 0.82 cc/g in the other two samples. The microporous pore volume, however, remained constant at 0.03 cc/g. The microporous surface area was 106 m^2/g out of total surface area of 976 m^2/g. HCl-treated MSU-S_{HY}(70) showed a similar isotherm to MSU-S_{HY}(70) although the low-pressure capillary step also showed hysteresis as with the higher pressure step. This indicates that N_2 sorption within the framework-confined pores was no longer reversible. The pore size distribution curve was also broader than the untreated sample. For MSU-S_{BEA}(67) and Al-MCM-41(70), there was only one step in the isotherm. The mesopores were of a mean diameter of 32 Å in MSU-S_{BEA}(67). The total pore volume was high, 0.88 cc/g and the surface area was 817 m^2/g. The microporous surface area constituted 91 m^2/g with a low microporous volume of 0.01 cc/g. In Al-MCM-41(70), the N_2 sorption curve showed a step at P/P_o ~0.3-0.5, coinciding with pores of ~ 30 Å. The sharp step without any hysteresis indicates the reversibility of N_2 sorption in this sample. The surface area was ~ 682 m^2/g, with a pore volume of 0.78 cc/g.

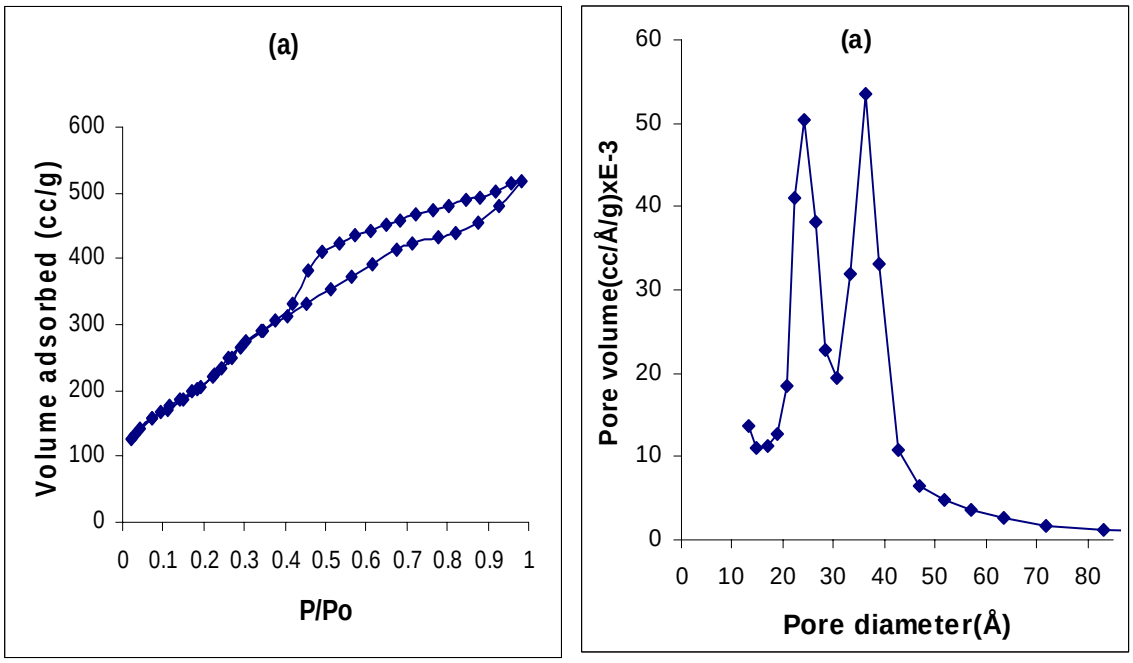

Fig. 3-5 N_2 adsorption/desorption isotherm and pore size distribution for calcined MSU-S_{HY}(25)

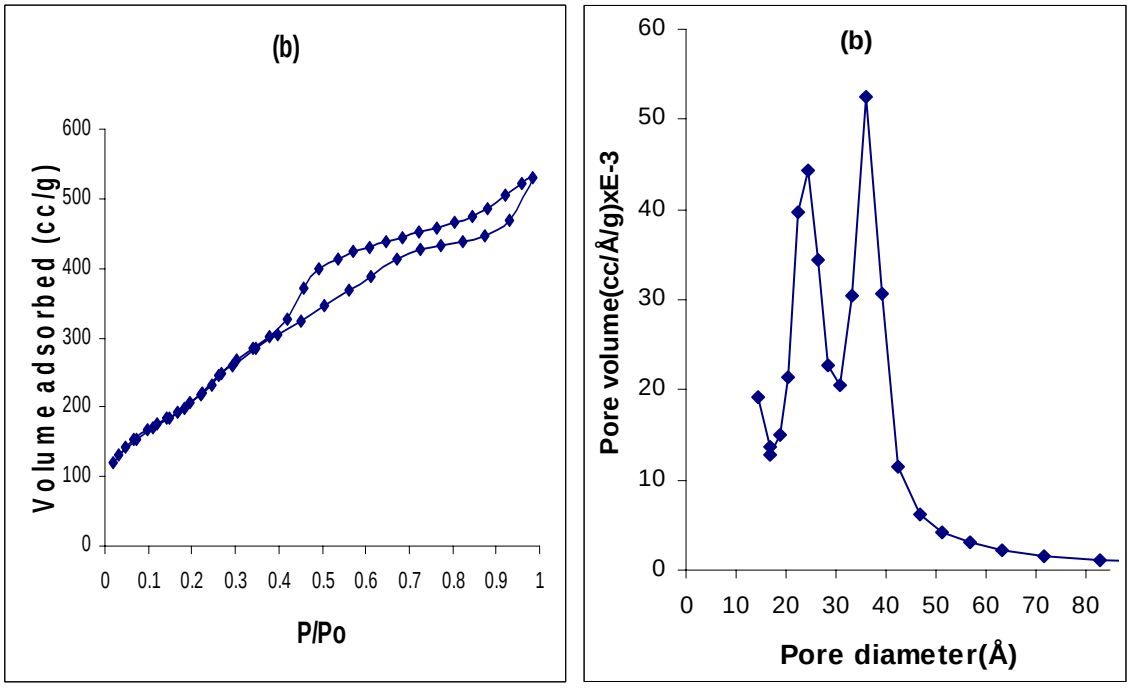

Fig. 3-6 N_2 adsorption/desorption isotherm and pore size distribution for calcined MSU-S_{HY}(50)

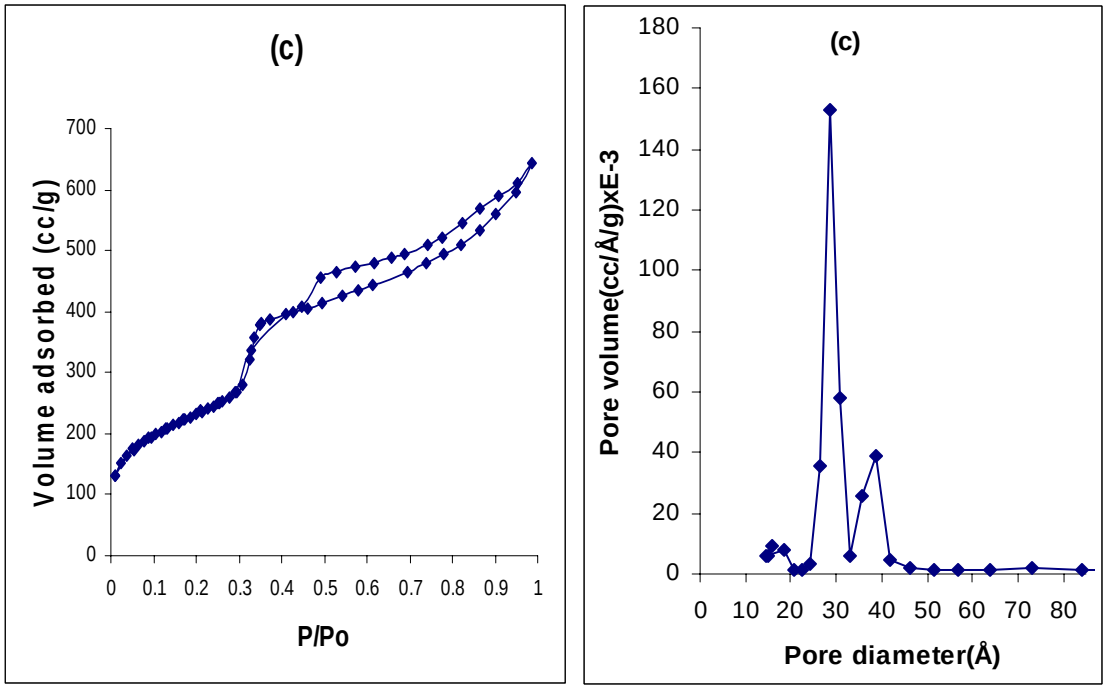

Fig. 3-7 N_2 adsorption/desorption isotherm and pore size distribution for calcined MSU-S_{HY}(70)

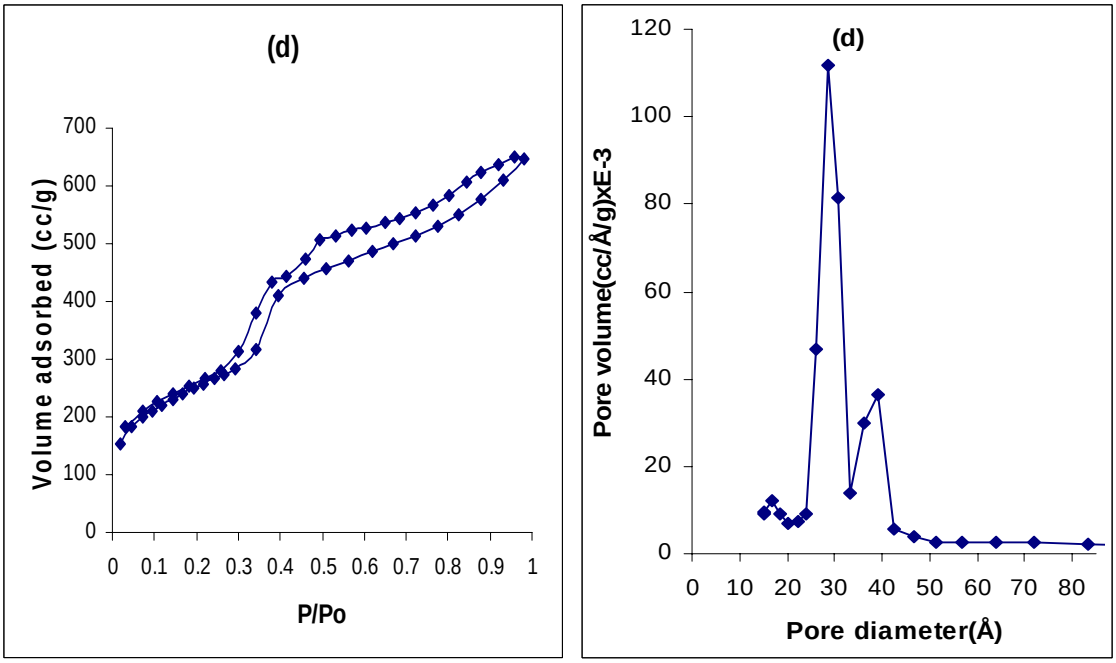

Fig. 3-8 N_2 adsorption/desorption isotherm and pore size distribution for calcined MSU-S_{HY}(70) after HCl-treatment.

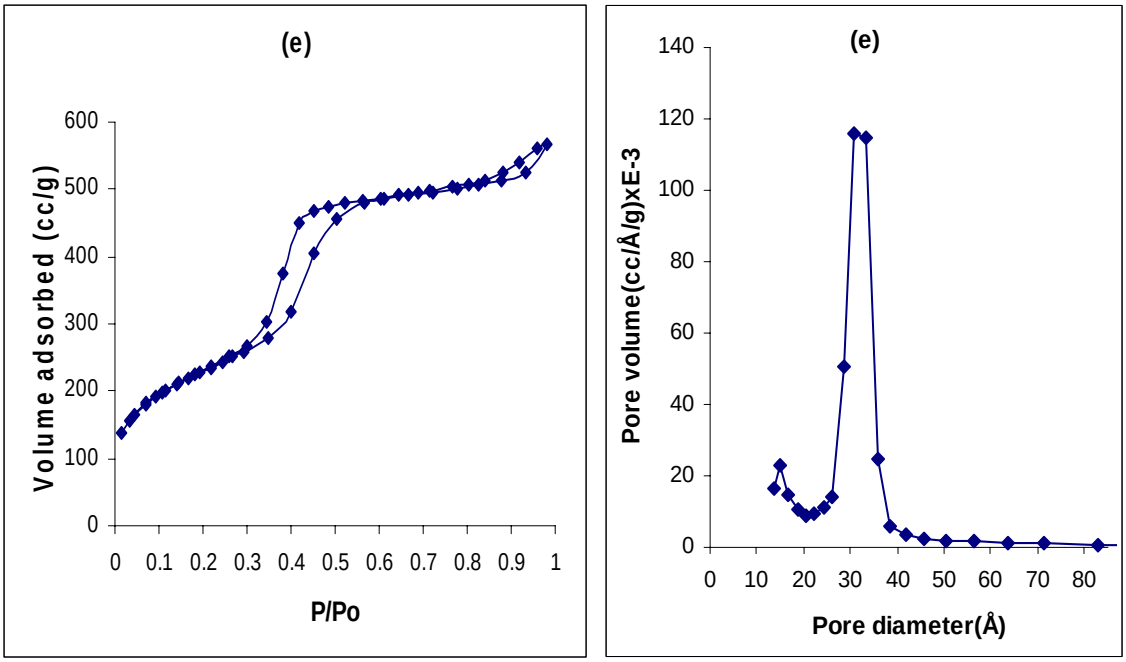

Fig. 3-9 N_2 adsorption/desorption isotherm and pore size distribution for calcined MSU-S_{BEA}(67).

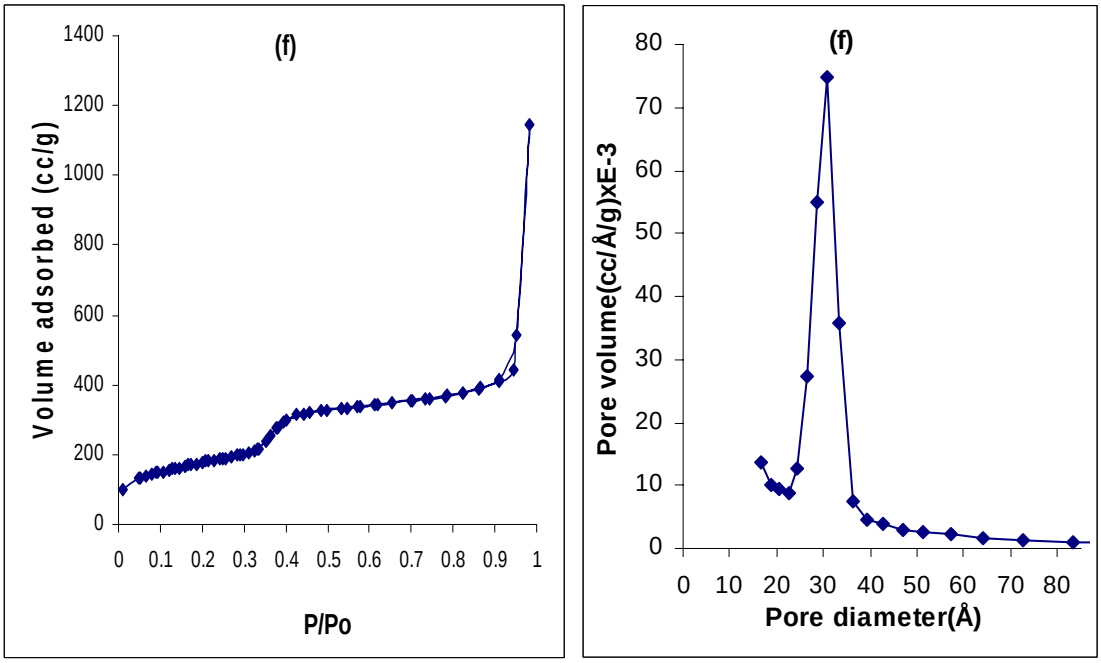

Fig. 3-10 N_2 adsorption/desorption isotherm and pore size distribution for calcined Al-MCM-41(70)

Table 3-2 Physical properties of MSU-S type mesoporous materials.

Catalyst	BET surface area/(m^2/g)	Total pore volume/(cc/g)	Micropore volume/(cc/g)	Micropore area/(m^2/g)
MSU-S_{HY}(25)	825	0.80	0.02	69
MSU-S_{HY}(50)	815	0.82	0.02	87
MSU-S_{HY}(70)	976	1.00	0.03	106
MSU-S_{HY}(70)[a]	774	0.95	0.03	103
MSU-S_{BEA}(67)	817	0.88	0.01	91
Al-MCM-41(70)	682	0.78	0.01	53

a = HCl-treated

3.1.3 ^{27}Al-MAS and ^{29}Si-MAS Solid State NMR Spectroscopy

The ^{27}Al-MAS NMR spectra of calcined MSU-S_{HY} samples (Fig. 3-11) showed very strong and broad peaks centered around 53-55 ppm and weak resonances around 0 ppm. The 55 ppm signals were assigned to $Al(O)_4$ joined to four $Si(O)_4$ units in highly symmetrical tetrahedral coordination [121]. The peak at ~0 ppm was assigned to $Al(O)_6$ species in poorly symmetrical octahedral coordination, (O_h). In MSU-S_{HY}(70) the chemical shift of the tetrahedral Al was ~53 ppm, compared to ~55 ppm in MSU-S_{HY}(25) and MSU-S_{HY}(50). The octahedral resonance for MSU-S_{HY}(70) was more intense than the other two samples, despite the lower aluminium content. The area of the aluminium in tetrahedral to octahedral was calculated (Table 3-3). The ratio decreased from 105 to 36.5 with increase of Si/Al ratio from 25 to 70. Despite the lower aluminium content in MSU-S_{HY}(70), more aluminium was present as extra-framework 6-fold coordinated species than framework tetrahedrally bound Al. This may be due to the faujasite structure of HY where high Al content is favoured. After

HCl-treatment of MSU-S_{HY}(70), the intensity of both the tetrahedral and octahedral Al peaks was reduced, especially the latter. This is due to the dissolution and consequent removal of the extraframework Al by the HCl. MSU-S_{BEA}(67) also showed two resonances, at ~ 55 ppm and another 0 ppm. The relative intensity of the tetrahedral to octahedral Al was lower compared to the corresponding value of MSU-S_{HY}(70), indicating the presence of more extraframework Al in MSU-S_{BEA}(67). However, in Al-MCM-41(70) only tetrahedrally coordinated Al, was detected (Fig. 3-12).

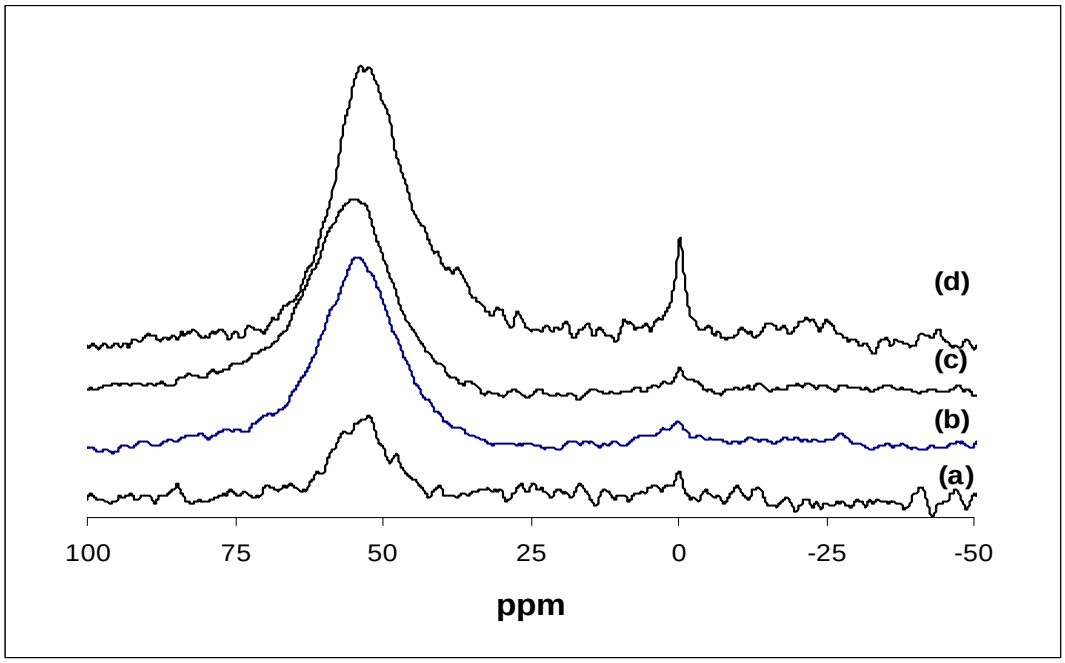

Fig. 3-11 ^{27}Al-MAS NMR spectra of (a) HCl-treated MSU-S_{HY}(70), (b) MSU-S_{HY}(25), (c) MSU-S_{HY}(50) and (d) MSU-S_{HY}(70).

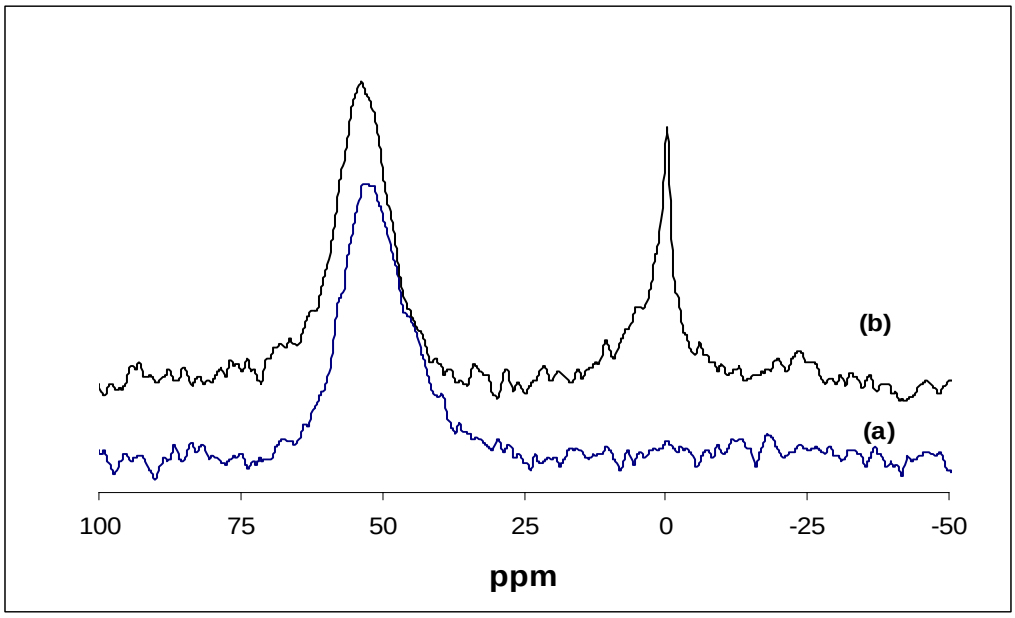

Fig. 3-12 ^{27}Al-MAS NMR spectra of (a) Al-MCM-41 (70) and (b) MSU-S_{BEA}(67).

The ^{29}Si-MAS NMR spectra of calcined MSU-S_{HY} are shown Figs. 3-13 and 3-14. The spectra showed broad resonances of Q^3 and Q^4 Si signals. Q^4 signals are due to Si attached to four SiO_4 units while Q^3 is due to $AlOSi(OSi)_3$ or $HO\text{-}Si(OSi)_3$. A small signal due to Q^2 resonance at ~91-93 ppm was also observed. This signal is about 1-7% of the total signal (Table 3-4). The broad lines may be due to the small or poorly crystalline zeolitic seed building blocks, so that the different Si coordination environments are not well-resolved. However, in general for the MSU-S_{HY} samples, Q^4 resonance made up about 58-67% of the total Si signal. These values were obtained by deconvolution of the broad peaks using the software on the computer. Q^3 resonance formed about 28-34% of the Si signal. The proportion of Q^4 relative to Q^3 and Q^2 resonance was highest in MSU-S_{HY}(70) and lowest in MSU-S_{HY}(25). After HCl-treatment, the relative Q^3: Q^4: Q^2 signal was rather similar to the sample prior to HCl-treatment. However, when the Si/Al ratio from NMR was compared, there was

an increase of the ratio from 11.7 to 45.9 after HCl-treatment. This shows that some Al had removed by the treatment.

In MSU-S_{BEA}(67), and Al-MCM-41(70), three Si environments were also detected. In the former, Q^4 resonance was about 61% of the total Si signal while in Al-MCM-41(70), Q^4 formed 80% of the Si signal.

Table 3-3 Tetrahedral aluminum/octahedral aluminum ratio from ^{27}Al-MAS NMR

Catalyst	Si/Al	$Al(O)_4$ area/(abs.)	$Al(O)_6$ area/(abs.)	$Al(O)_4/Al(O)_6$
MSU-S_{HY}(25)	25	1.52×10^{10}	1.44×10^{8}	105
MSU-S_{HY}(50)	50	1.77×10^{10}	3.38×10^{8}	52.4
MSU-S_{HY}(70)	70	2.28×10^{10}	6.24×10^{8}	36.5
MSU-S_{HY}(70)[a]	-	4.47×10^{9}	4.01×10^{8}	11.1
MSU-S_{BEA}(67)	67	1.21×10^{10}	4.63×10^{9}	2.61
Al-MCM-41(70)	70	1.30×10^{10}	—	—

a = HCl-treated

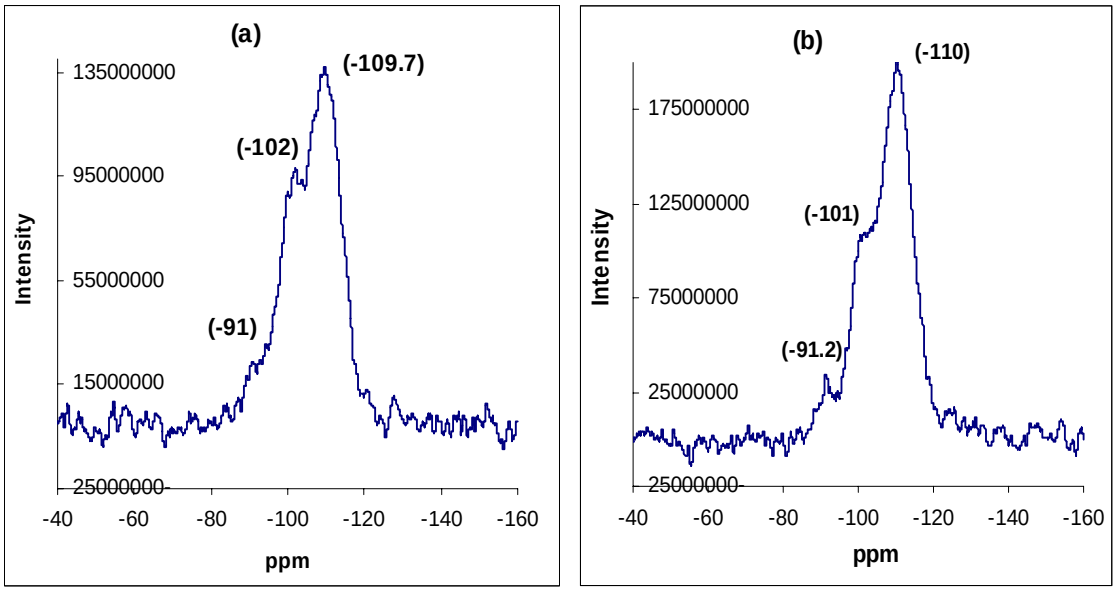

Fig. 3-13 ^{29}Si-MAS NMR of (a) MSU-S_{HY}(25) and (b) MSU-S_{HY}(50)

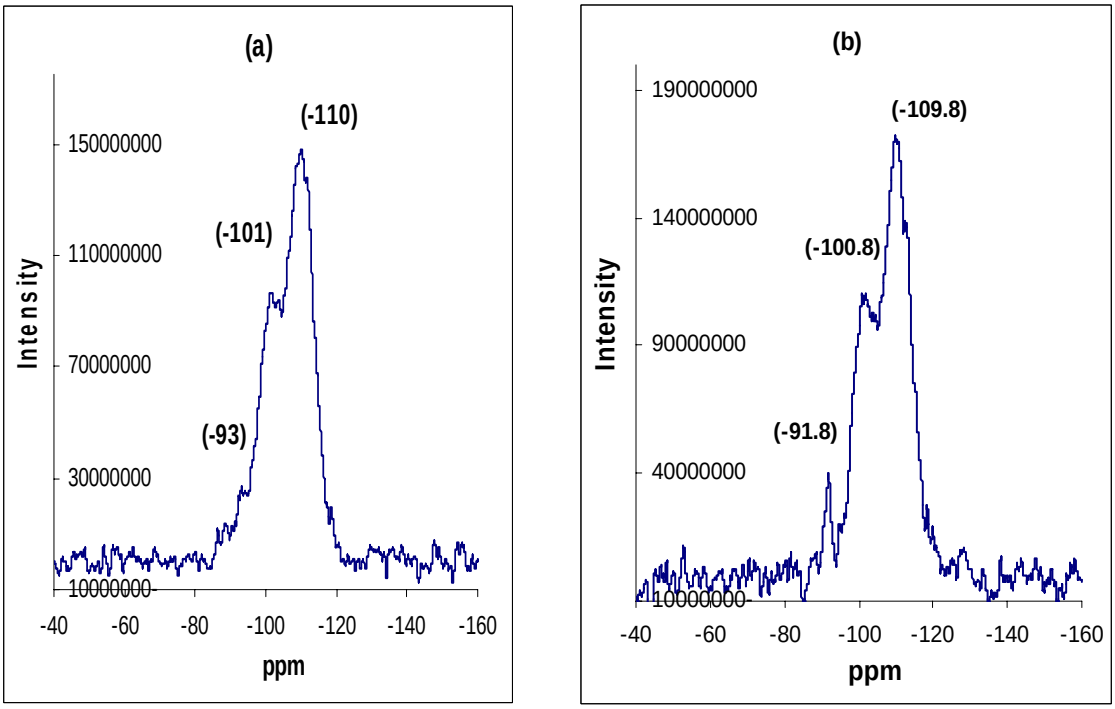

Fig. 3-14 ^{29}Si-MAS NMR of (a) MSU-S_{HY}(70) and (b) HCl-treated MSU-S_{HY}(70).

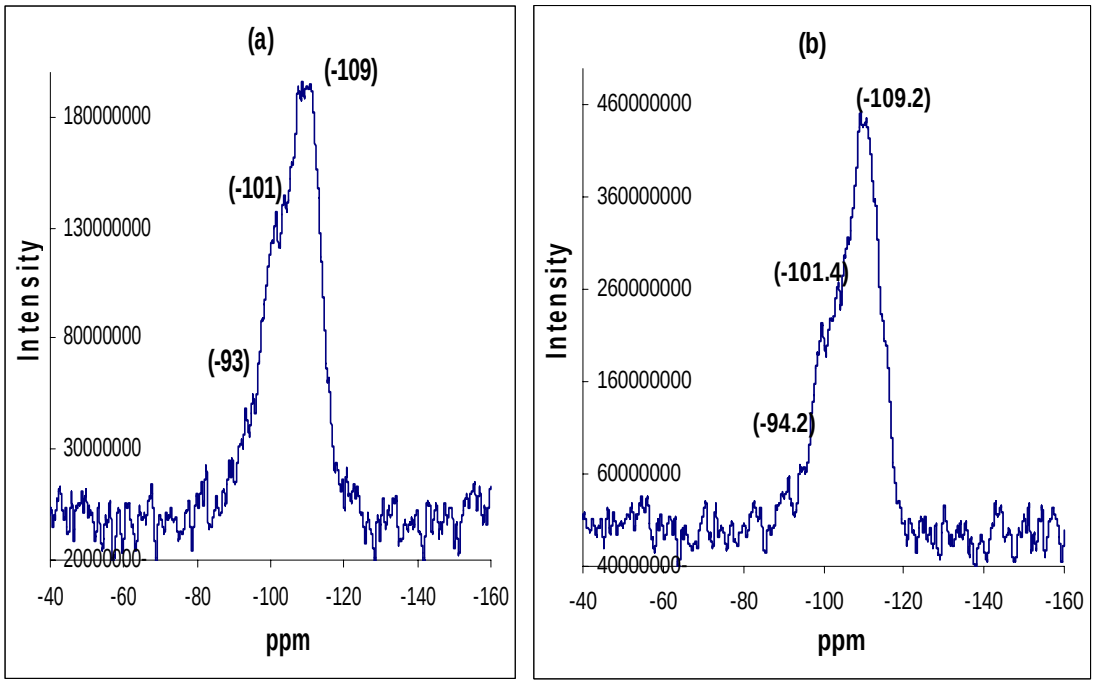

Fig. 3-15 ^{29}Si-MAS NMR of (a) MSU-S_{BEA}(67) and (b) Al-MCM-41(70).

Table 3-4 ^{29}Si-MAS NMR data of mesoporous catalysts

Catalyst	Si/Al	Q^4(abs.)/10^{10}	Q^3(abs.)/10^{10}	Q^2(abs.)/10^{10}	Total* abs./10^{11}	$(Si/Al)_{NMR}$
MSU-S_{HY}(25)	25	8.06	4.71	1.07	1.45	9.44
MSU-S_{HY}(50)	50	18.3	10.1	1.64	3.17	17.6
MSU-S_{HY}(70)	70	18.0	7.71	1.08	2.74	11.7
MSU-S_{HY}(70)[a]	unknown	14.7	6.68	0.52	2.44	45.9
MSU-S_{BEA}(67)	67	17.4	10.5	0.56	2.95	17.6
Al-MCM-41(70)	70	45.8	10.6	0.67	5.66	43.5

a = HCl-treated

* = Total signal is from integration of entire broad signal.

3.1.4 Pyridine Adsorption IR

The acidity of the samples was probed by pyridine IR spectroscopy. Figs. 3-16 and 3-17 show the infrared spectra of pyridine adsorption at room temperature and 100 ^{o}C respectively. MSU-S_{HY} mesoporous materials show the presence of Lewis acidity. Bands in the range of 1440-1456, 1490 and 1560-1632 cm^{-1} indicate the presence of both hydrogen-bonded and coordinately bonded pyridine at room temperature (Fig. 3-16) [87]. The band around 1450 cm^{-1} became narrower and more intense with increase of Si/Al ratio. After HCl-treatment, the bands became broader and intense than those of MSU-S_{HY}(70). This shows that Lewis sites of varying acidity had formed. After heating the samples to 100 ^{o}C, the intensity of the bands decreased. Similarly, in MSU-S_{BEA}(67), only Lewis acid sites were detected. No Brønsted acidity was detected. However, in Al-MCM-41(70), both Brønsted and Lewis acid sites were present. The former was detected by the absorption band at ~ 1550 cm^{-1}. The band presented even after heat treatment at 100 ^{o}C.

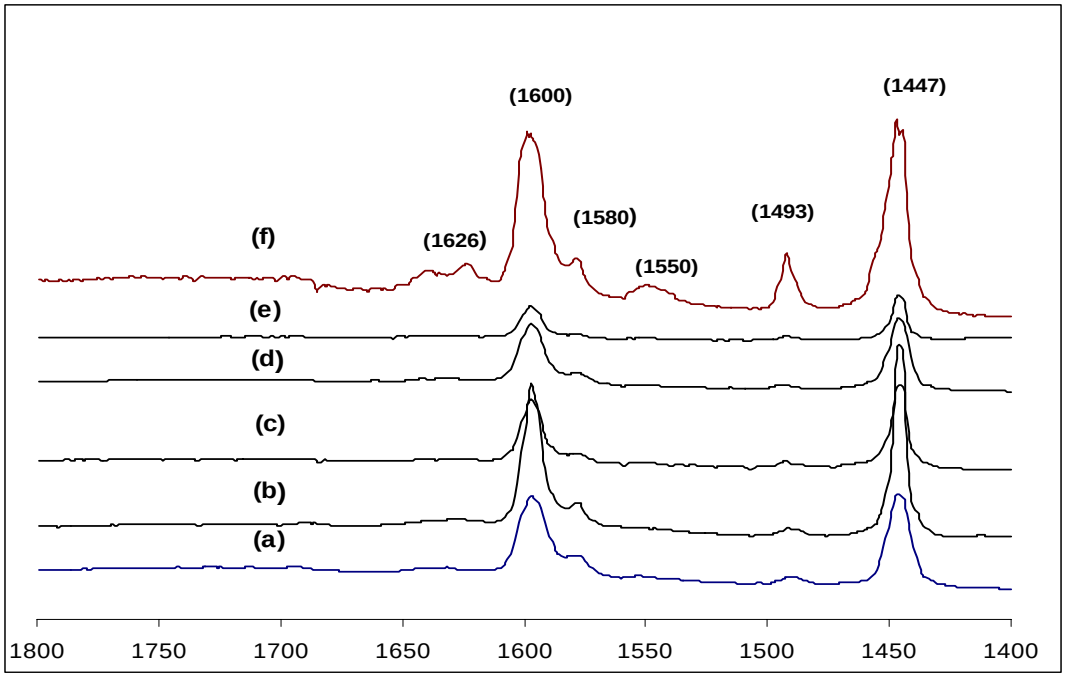

Fig. 3-16 IR pyridine adsorption at room temperature (a) MSU-S_{HY}(25), (b) MSU-S_{HY}(50), (c) MSU-S_{HY}(70), (d) HCl-treated MSU-S_{HY}(70), (e) MSU-S_{BEA}(67) and (f) Al-MCM-41(70).

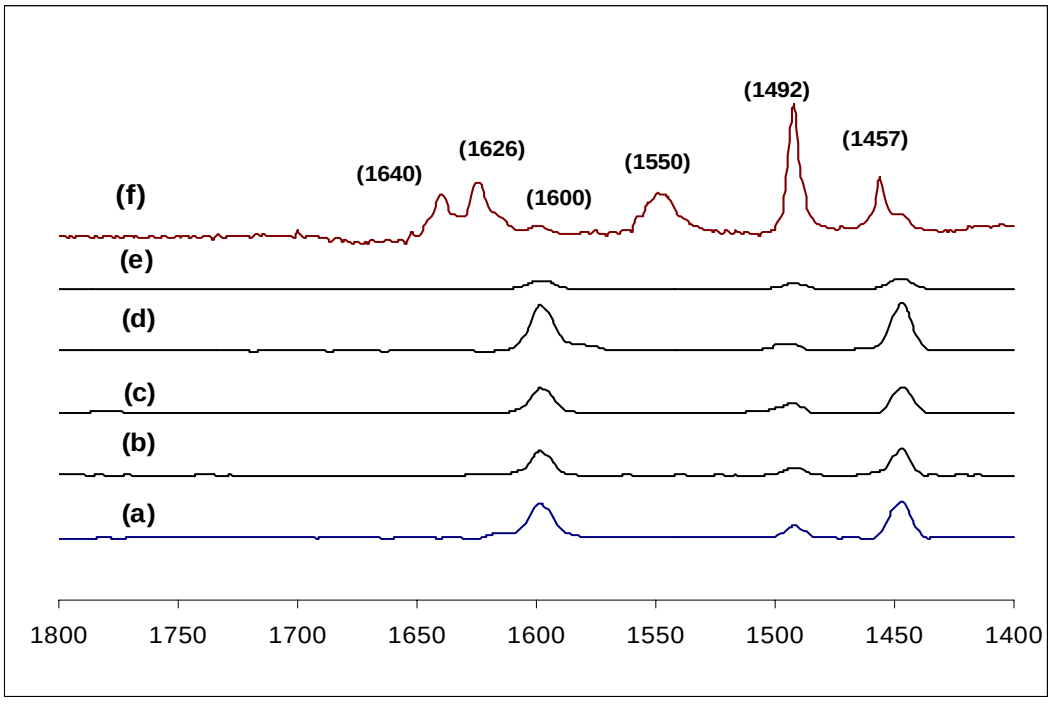

Fig. 3-17 IR pyridine adsorption at 100 °C (a) MSU-S_{HY}(25), (b) MSU-S_{HY}(50), (c) MSU-S_{HY}(70), (d) HCl-treated MSU-S_{HY}(70), (e) MSU-S_{BEA}(67) and (f) Al-MCM-41(70).

3.2 Silica-Supported Boron Oxide Catalysts

3.2.1 Powder X-Ray Diffraction

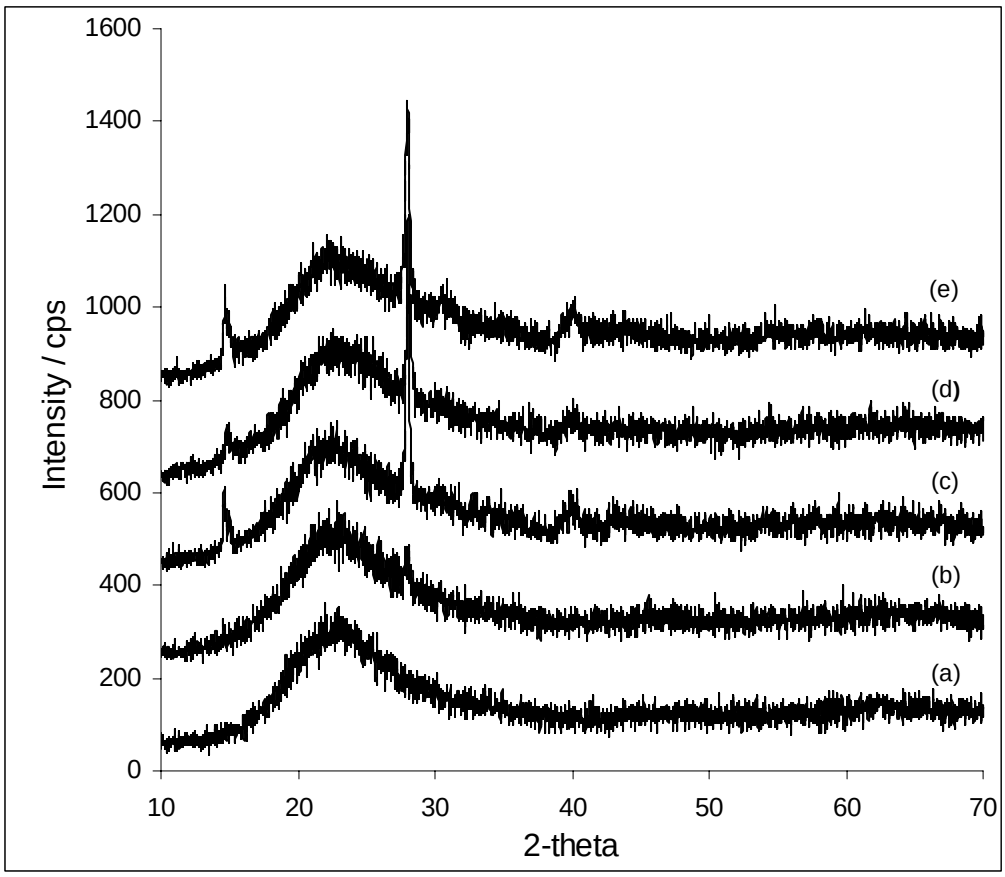

Fig. 3-18 XRD patterns of (a) SiO_2 and SiO_2-supported catalysts with (b) 5% B_2O_3, (c)10% B_2O_3, (d) 15% B_2O_3 and (e) 20% B_2O_3 measured at 25 ^oC.

The XRD patterns of wt% B_2O_3/SiO_2 catalysts with various boria loading and pure SiO_2 are shown in Fig. 3-18. A sharp peak was observed at $2\theta = 28^0$ for all the B_2O_3/SiO_2 catalysts. Except for 5% B_2O_3/SiO_2 all the other boria-loaded catalysts showed additional broad peaks at $2\theta = 15°$, 31° and 40°. The intensity of the peak $2\theta = 28°$ increased with the increase of boria loading. This agrees with that reported for B_2O_3/Al_2O_3 catalysts by Murakami et al. [123], in which the intensity of diffraction lines increased with boria loading.

Comparing with the literature values, these peak positions could be due to either B_2O_3 or H_3BO_3. Variable temperature studies were conducted on these samples. Fig. 3-19 shows the XRD patterns obtained at different temperatures for 15 wt% B_2O_3/SiO_2 catalyst which was heated in-situ. The intensity of the peak at 2θ ~28° continuously decreased with temperature up to 70-75 °C. On cooling down in static air environment, no peaks were observed. However, after exposure to the ambient environment for a few minutes, the 2θ peak at ~28° could once again be observed. Hence, it shows that on the support, the boron oxide is present as the hydrated form as boric acid.

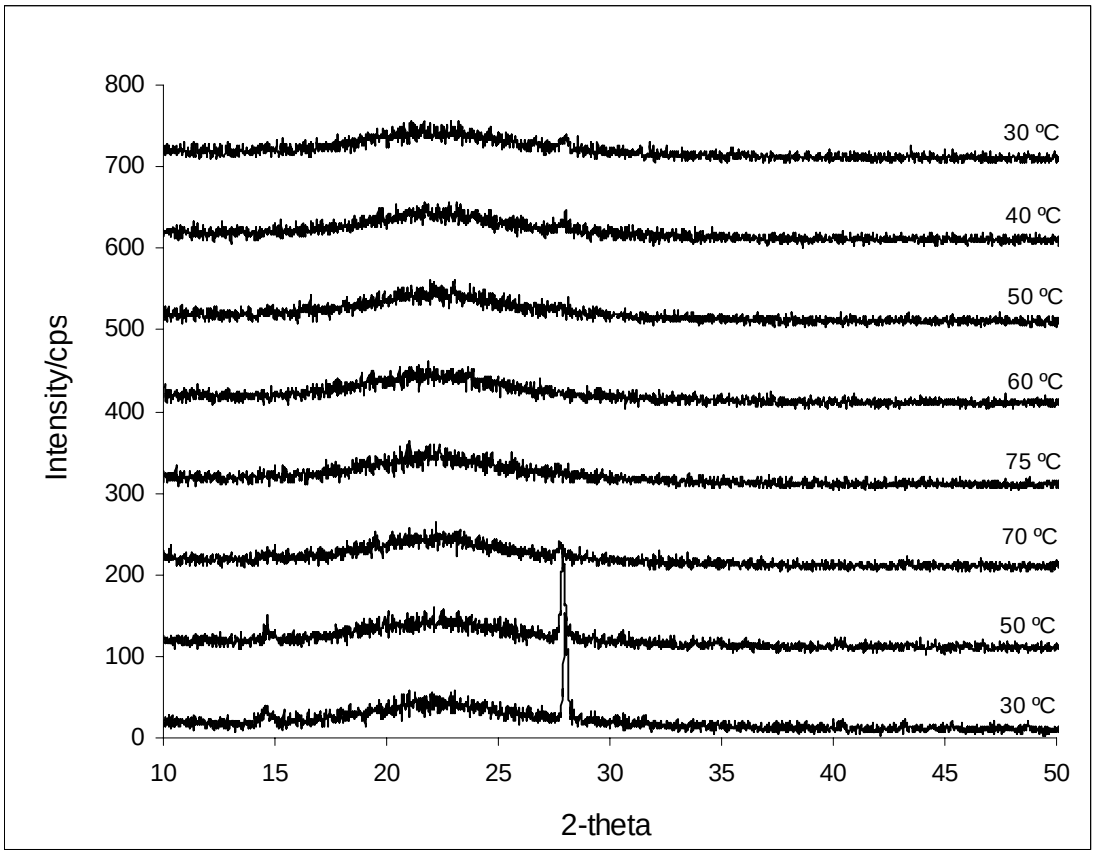

Fig. 3-19 XRD of 15% B_2O_3/SiO_2 at different temperatures

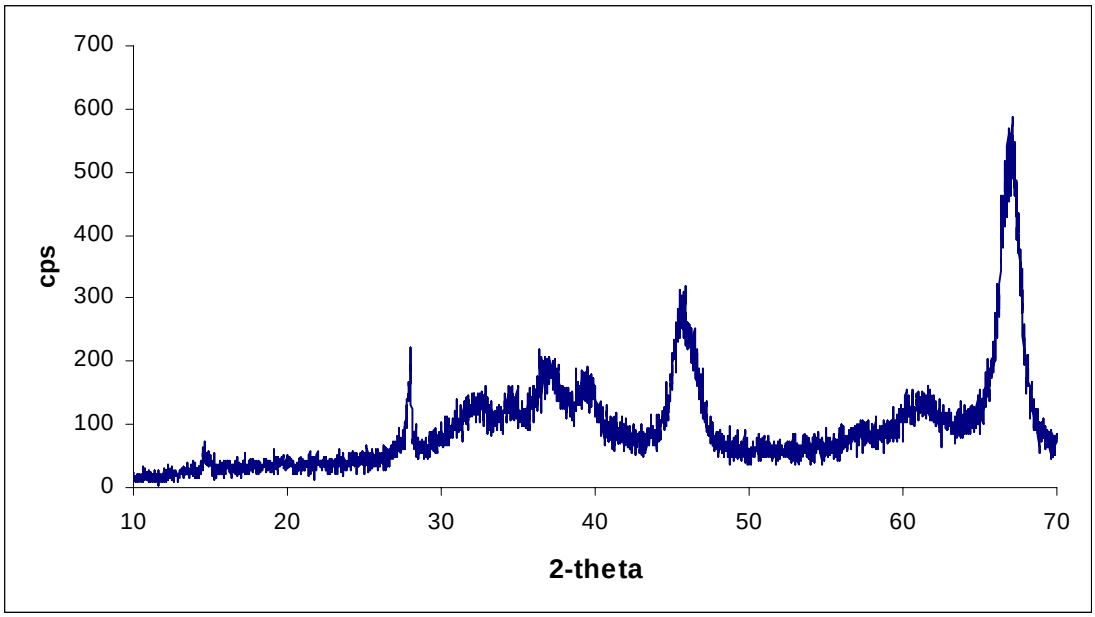

Fig. 3-20 XRD of calcined 15% B_2O_3/Al_2O_3

Figs. 3-20–3-22 show the XRD patterns of 15 wt% B_2O_3 on other supports - Al_2O_3, TiO_2, and ZrO_2. 15 wt% B_2O_3/Al_2O_3 exhibited a sharp peak at $2\theta = 28^o$ due to $B(OH)_3$. No other diffraction peaks of $B(OH)_3$ were detected. broad peaks are due to γ-Al_2O_3. The titania support shows a mixture of anatase and rutile phases, with anatase being predominant. For 15 wt% B_2O_3/TiO_2, the most intense peak of $B(OH)_3$ can be observed at $2\theta \sim 28^o$. The zirconia support was pure tetragonal phase. Due to the small crystallite size, the x-ray diffraction peaks were rather broad. As with the other supports, after impregnation, 15 wt% B_2O_3/ZrO_2, shows the presence of $B(OH)_3$.

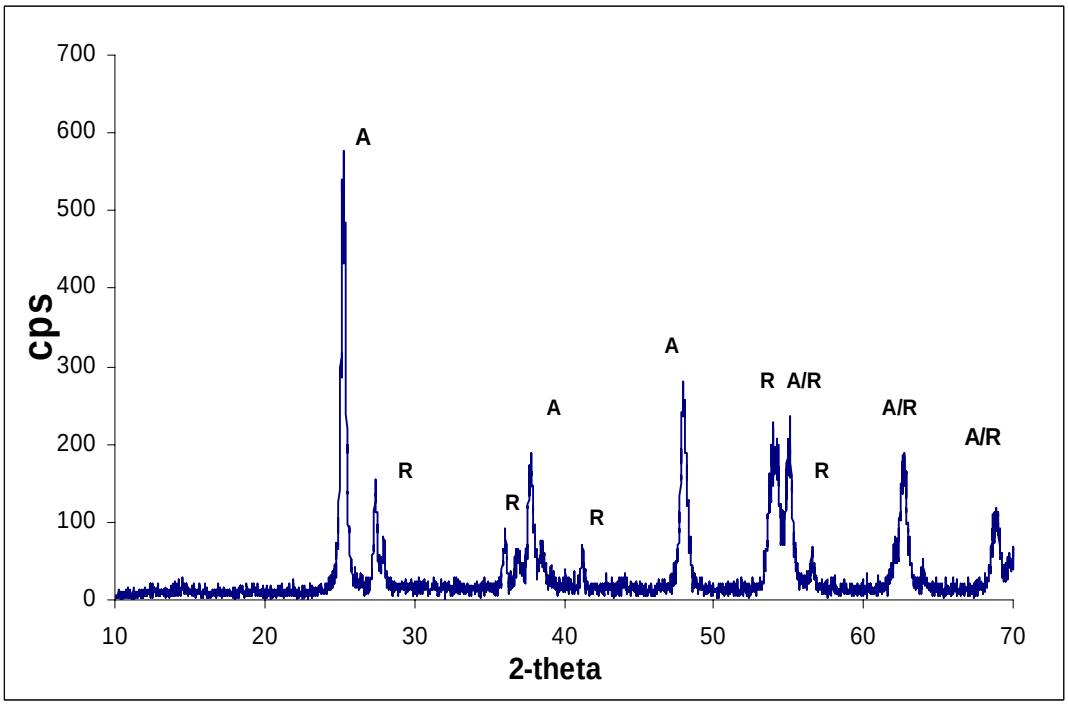

Fig. 3-21 XRD of calcined 15% B_2O_3/TiO_2

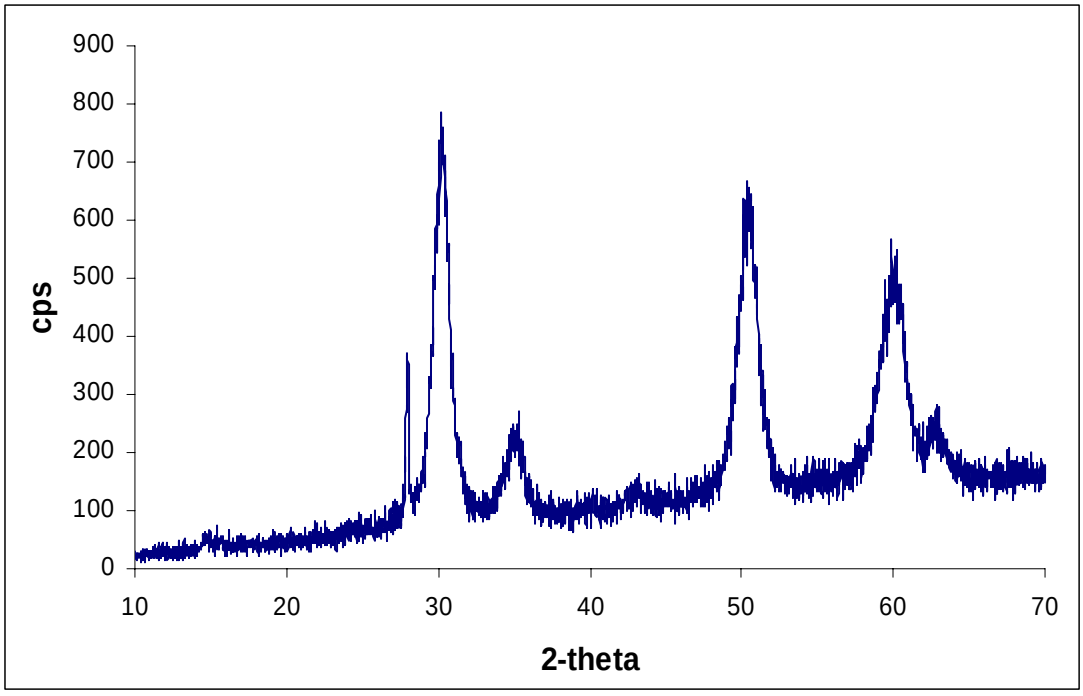

Fig. 3-22 XRD of calcined 15% B_2O_3/ZrO_2

3.2.2 BET Surface Area and Pore Volume

For B_2O_3/SiO_2 catalysts, an increase in boria loading resulted in a decrease of surface area and pore volume (Fig. 3-23). The surface area decreased from 288 m^2/g in SiO_2 to 231 m^2/g in the sample with 20 wt.% boria loading (Table 3-5). At the same time, the pore volume decreased from 0.75 cc/g to 0.52 cc/g. This suggests that the boria covered some of the pores of the silica at high loading. 15% B_2O_3/TiO_2 exhibited the lowest surface area and pore volume compared to the other supported boria catalysts. The surface area and pore volume of 15% B_2O_3/TiO_2 are 37.8 m^2/g and 0.14 cc/g, respectively. The surface area of 15% B_2O_3/ZrO_2 was 103 m^2/g, similar to that of 15% B_2O_3/Al_2O_3. However, their pore volumes differed by a factor of two, with the Al_2O_3-imprgneted sample having the higher surface area.

Table 3-5 BET surface area and pore volume of supported boron oxide calcined at 350 ^oC

Catalyst	BET Surface Area (m^2/g)	Pore Volume (cc/g)
SiO_2	288	0.75
5% B_2O_3/SiO_2	276	0.70
10% B_2O_3/SiO_2	255	0.63
15% B_2O_3/SiO_2	235	0.57
20% B_2O_3/SiO_2	231	0.52
15% B_2O_3/TiO_2	37.8	0.14
15% B_2O_3/ZrO_2	103	0.38
15% B_2O_3/Al_2O_3	110	0.76

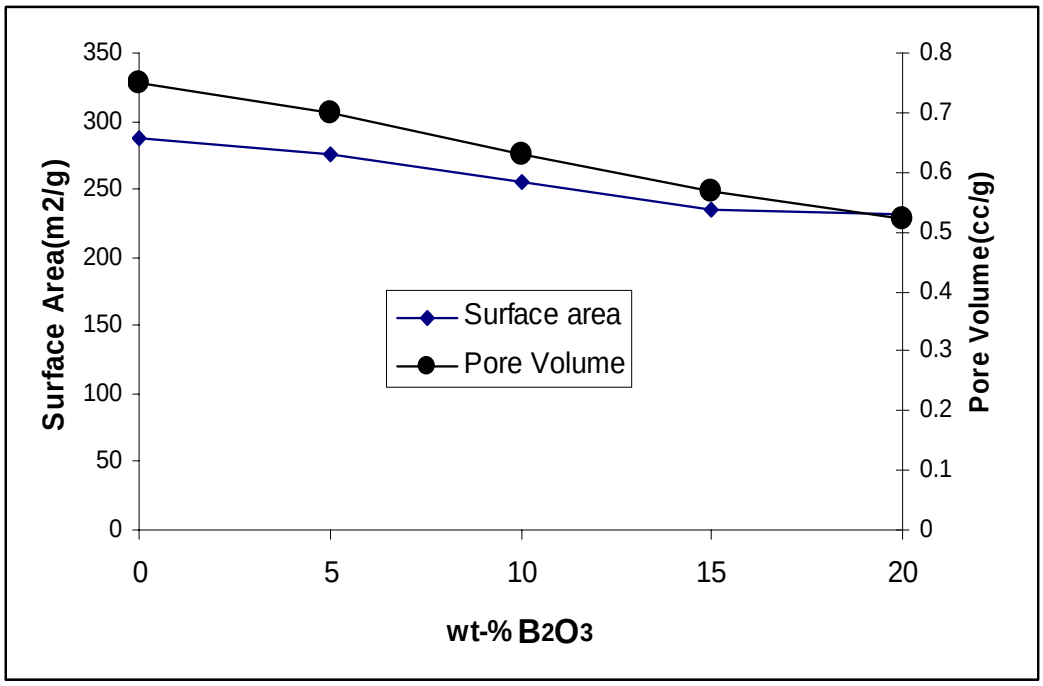

Fig. 3-23 Surface area and pore volume of silica-supported boria catalysts.

3.2.3 ^{11}B-MAS NMR

Fig. 3-24 displays the ^{11}B-MAS NMR spectra of B_2O_3/SiO_2 catalysts with different boria loading. In amorphous and crystalline compounds, boron may exist in tetrahedral BO_4 units and trigonal BO_3 units. Tetrahedrally coordinated boron could also arise from the coordination of hydroxyl groups to BO_3 units or from the coordination of an oxygen in the support to the three-coordinated boron (Scheme 3-1). The spectra of the five compounds showed peaks corresponding to BO_3 and BO_4 units. The signal corresponding to BO_4 unit is around 5 ppm. The signal for trigonally coordinated BO_3 was split and broadened due to second order quadrupolar effect [63]. With increase of boria loading, the signal of BO_4 became stronger and broader. After drying for 48 h at 100 ^{o}C, the ^{11}B-NMR spectrum of 15% B_2O_3/SiO_2 showed that the resonance due to tetrahedrally-coordinated B was reduced compared to the three-

coordinated boron (Fig. 3-25). This shows that part of the BO_4 resonance is due to hydroxylated B species.

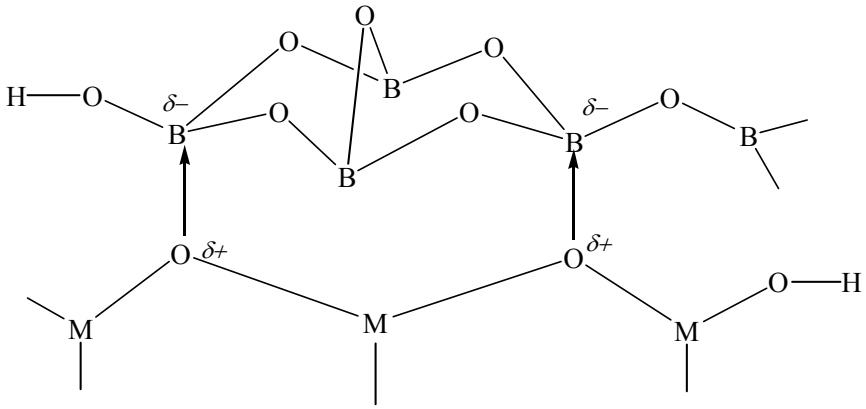

Scheme 3-1 Structure of metal oxide-supported boria catalyst [61]. M = metal.

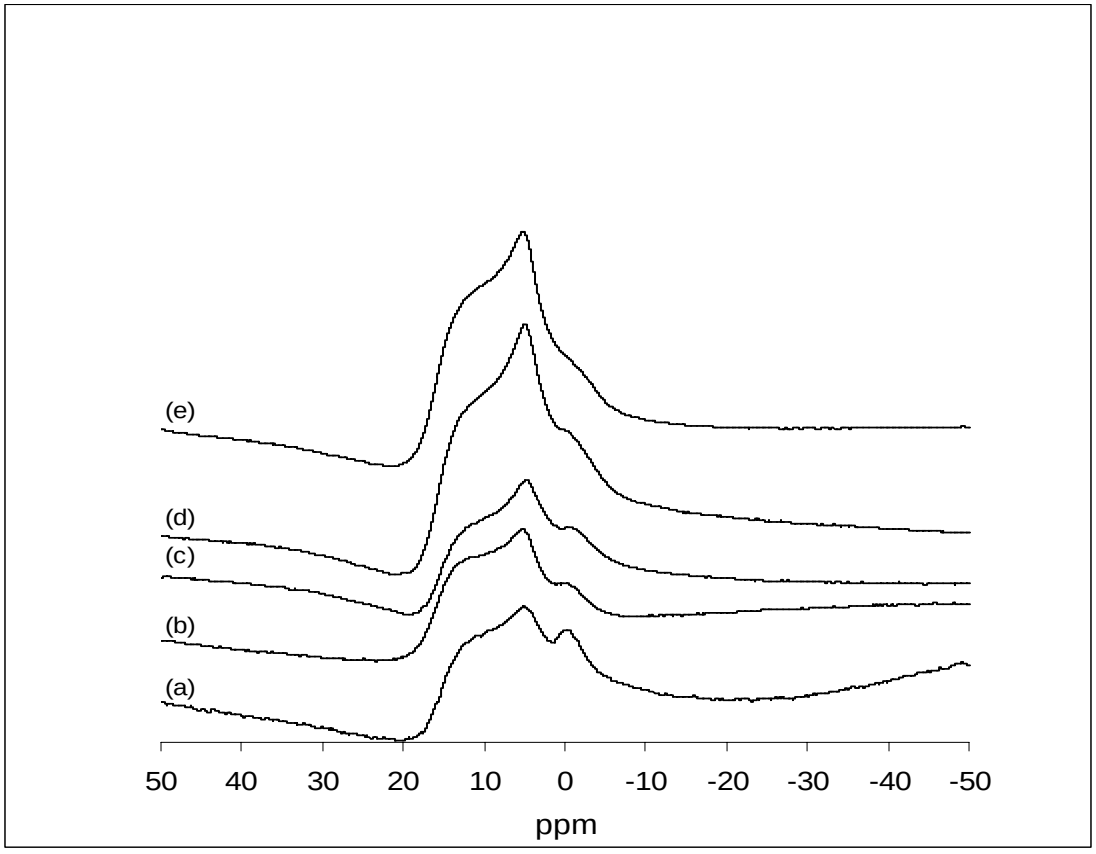

Fig. 3-24 ^{11}B-MAS NMR of (a) 5% B_2O_3, (b) 10% B_2O_3, (c) 15% B_2O_3, (d) 20% B_2O_3 and (e) 40% B_2O_3.

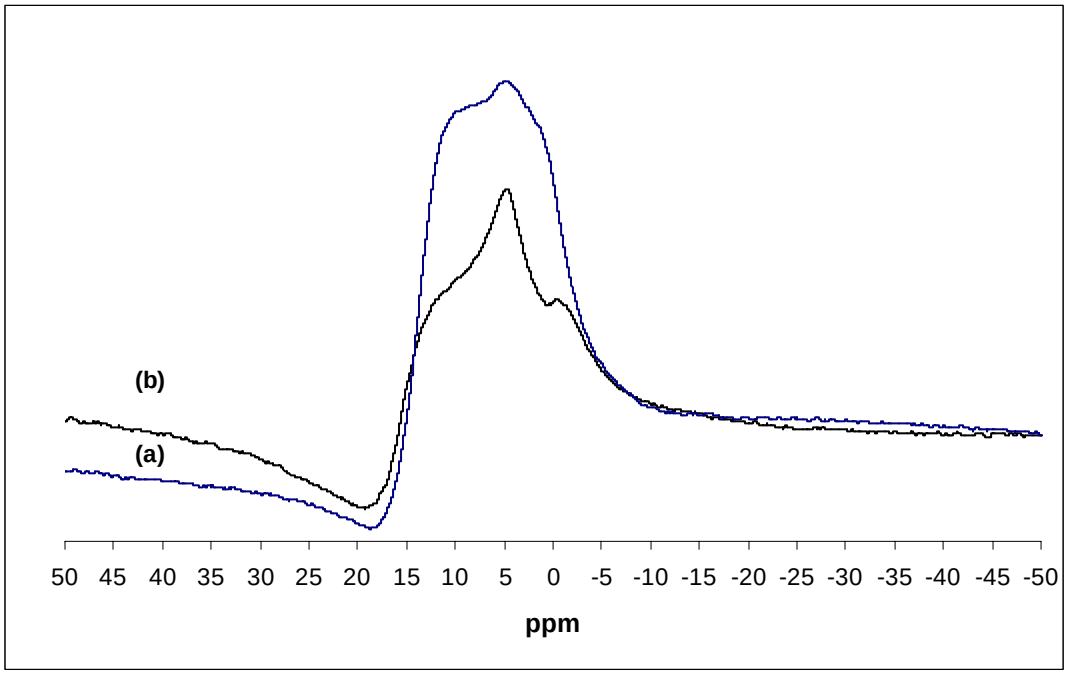

Fig. 3-25 ^{11}B-MAS NMR of (a) 15% B_2O_3/SiO_2 after drying at 100 ^{o}C for 48 h, (b) 15% B_2O_3/SiO_2

3.2.4 IR Pyridine Adsorption

Fig. 3-26 shows the infrared spectra of pyridine adsorption at room temperature on SiO_2 and boria-supported SiO_2 catalysts. SiO_2 shows only two bands ~ 1446 cm^{-1} and 1580 cm^{-1}. Both bands are indicative of hydrogen bonded pyridine. A small adsorption at ~ 1462 cm^{-1} is due to the weak Lewis acidity of the material. After impregnation with 5 wt% boron oxide, the 1462 cm^{-1} band became stronger. In addition, adsorption bands at 1495 cm^{-1} and 1626 cm^{-1} appeared. Both these bands are due to coordinately bonded pyridine at Lewis acid sites. No Brønsted acidity was noted in this sample. Brønsted acidity was observed from samples with 10 wt% B_2O_3 and higher. Interestingly, in the high boron oxide samples, the adsorption band at ~ 1462 cm^{-1} completely disappeared. However, from the presence of bands at 1595 cm^{-1}, and 1626 cm^{-1}, Lewis acid sites are still present.

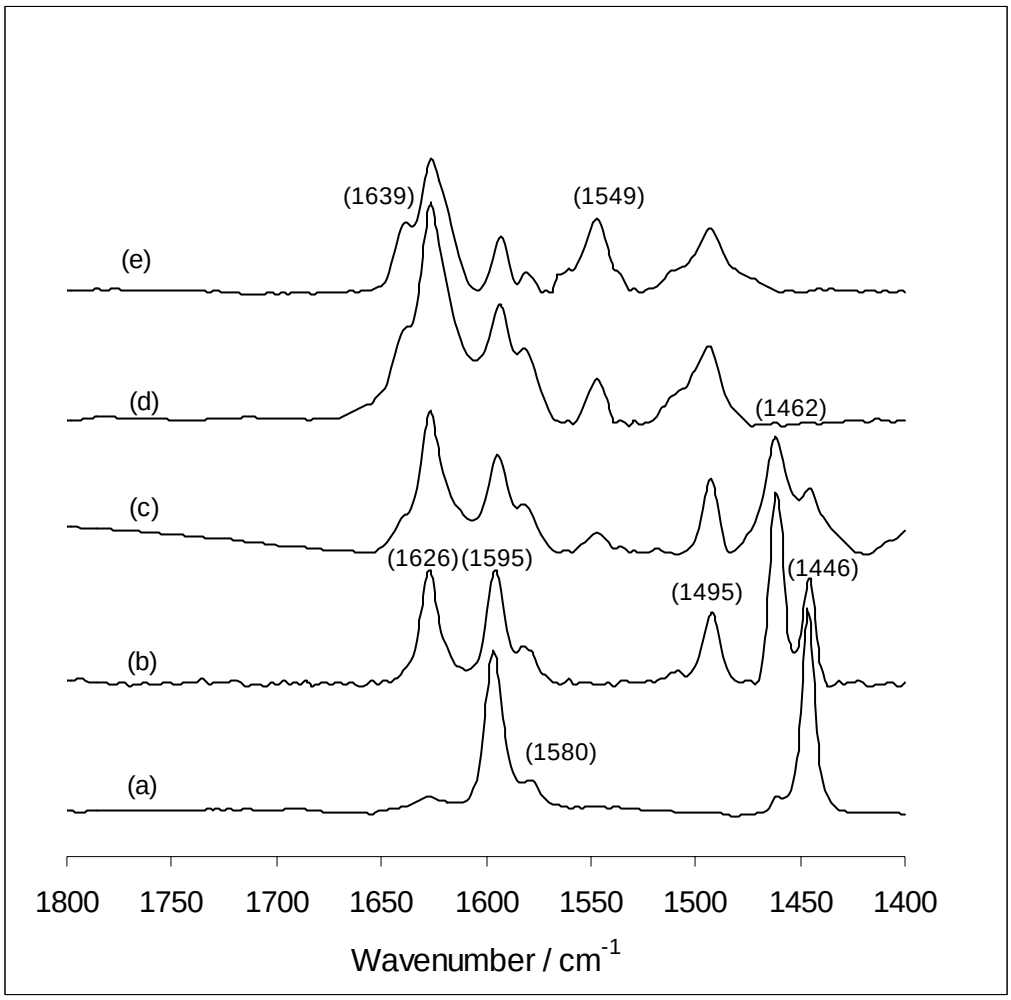

Fig. 3-26 IR spectra of pyridine adsorbed at room temperature on (a) SiO_2, (b) 5% B_2O_3 /SiO_2 , (c) 10% B_2O_3/SiO_2, (d) 15% B_2O_3/SiO_2 and (e) 20% B_2O_3/SiO_2

On heating the 15 wt% B_2O_3/SiO_2 sample to higher temperatures, the intensity of the absorption bands decreased due to desorption of pyridine. The bands also narrowed as only strongly bound pyridine remained. Even after heating to 200 ^oC, both Lewis and Brønsted acidity were still present.

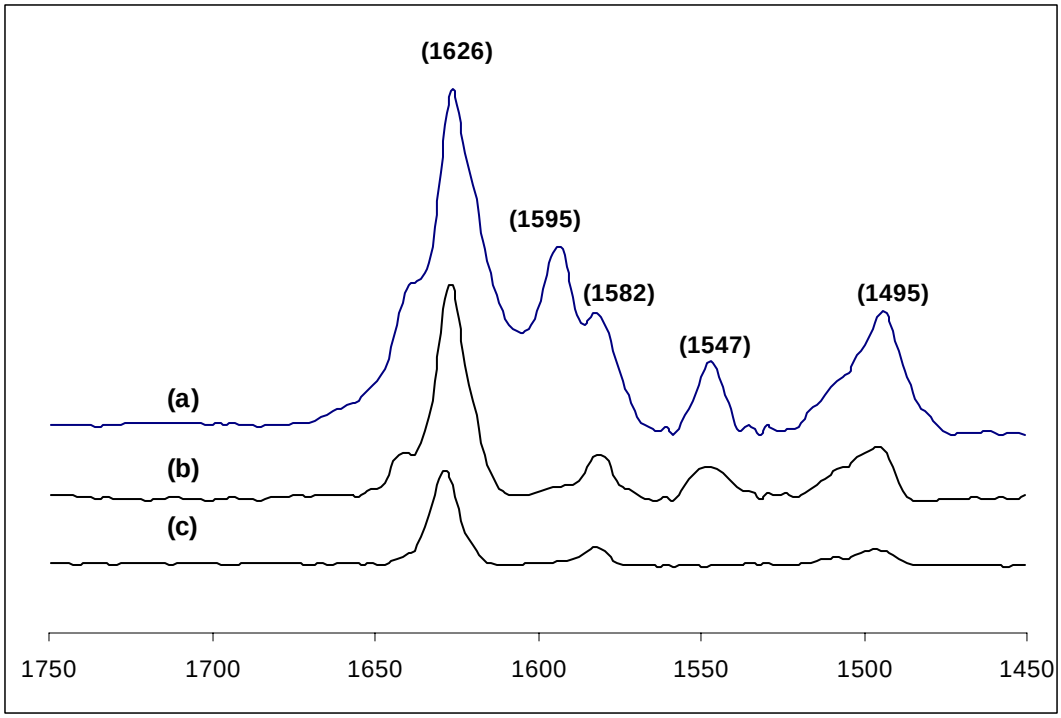

Fig. 3-27 Pyridine adsorbed on 15% B_2O_3/SiO_2 at different temperatures (a) room temperature, (b) 100 ^oC and (c) 200 ^0C.

3.3 $InCl_3$-Supported on $Zr(OH)_4$ Catalyst

3.3.1 X-Ray Diffraction

The powder diffraction patterns of $InCl_3$/ $Zr(OH)_4$ catalysts dried at 120 ^oC overnight are shown in Fig. 3-28. No peaks due to $InCl_3$ were observed for loadings of 0.25-4 mmol $InCl_3$/g $Zr(OH)_4$. This suggests that the crystallites of $InCl_3$ on the support were very small, < 3 nm, or the $InCl_3$ was present as a thin layer. Only the amorphous spectrum of $Zr(OH)_4$ was detected.

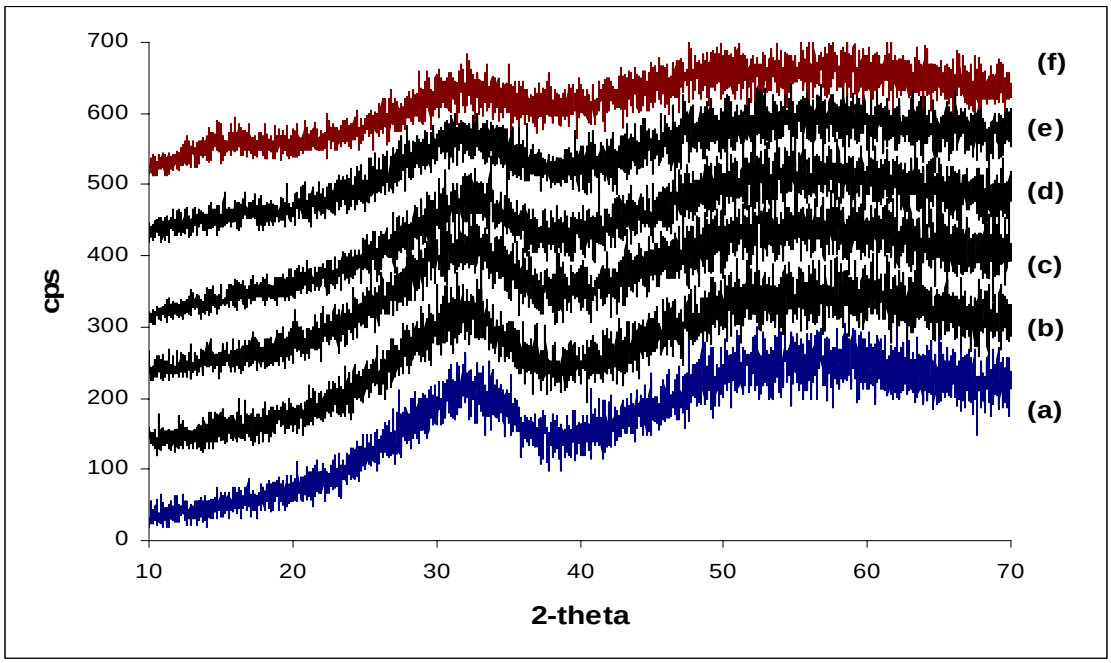

Fig. 3-28 XRD of (a) $Zr(OH)_4$ (b) 0.25 mmol $InCl_3$/g $Zr(OH)_4$ (c) 0.5 mmol $InCl_3$/g $Zr(OH)_4$ (d) 1 mmol $InCl_3$/g $Zr(OH)_4$ (e) 2 mmol $InCl_3$/g $Zr(OH)_4$ and (f) 4 mmol $InCl_3$/g $Zr(OH)_4$ dried at 120 ^oC

3.3.2 BET Surface Area and Pore Volume

Table 3-6 shows the BET surface area and pore volume of $InCl_3$ supported catalysts. Samples were degassed at 100 ^0C for 3 h before analysis. An increase in $InCl_3$ loading resulted in a decrease of surface area and pore volume. The surface area decreased from 330 m^2/g in 0.25 mmol $InCl_3$/g $Zr(OH)_4$ to 137 m^2/g in the sample with 4 mmol $InCl_3$ loading. At the same time the pore volume decreased from 0.71 cc/g to 0.34 cc/g. In contrast to the high surface area of $Zr(OH)_4$-supported $InCl_3$, 2 mmol $InCl_3$/g ZrO_2 exhibited a lower surface area value of 100 m^2/g. This is due to the low surface area of ZrO_2

Table 3-6 BET surface area and pore volume of supported $InCl_3$ catalysts dried at 120 ^oC

Catalyst	BET surface area (m^2/g)	Pore volume (cc/g)
$Zr(OH)_4$	335	0.71
0.25 mmol $InCl_3$/g $Zr(OH)_4$	330	0.70
0.5 mmol $InCl_3$/g $Zr(OH)_4$	329	0.66
1 mmol $InCl_3$/g $Zr(OH)_4$	286	0.62
2 mmol InCl3/g $Zr(OH)_4$	203	0.46
4 mmol $InCl_3$/g $Zr(OH)_4$	137	0.34
2 mmol $InCl_3$/g ZrO_2	100	0.39

3.3.3 IR Pyridine Adsorption

$InCl_3/Zr(OH)_4$ shows the presence of Lewis and Brønsted acidity (Fig. 3-29). After evacuation of the IR cell at room temperature for 1 h, absorption bands of hydrogen-bonded pyridine and coordinately bonded pyridine together that of pyridinium ion were observed. Heating to 100 ^oC removed the hydrogen-bonded pyridine. Both Lewis and Brønsted acidity were observed even after heating to 200 ^oC.

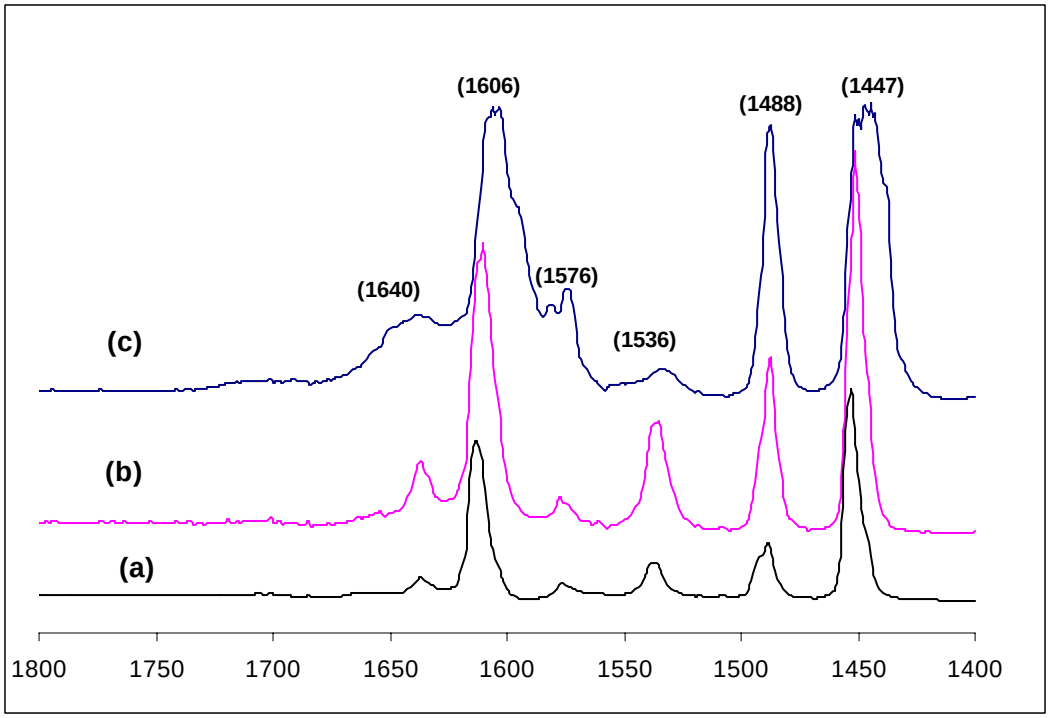

Fig. 3-29 IR pyridine adsorption on 2 mmol $InCl_3$/g $Zr(OH)_4$ at (a) room temperature, (b) 100 ^oC and (c) 200 ^oC.

3.4 ZrO_2-Supported SiO_2 Catalysts

3.4.1 Powder X-Ray Diffraction

Hydrous zirconia was refluxed at 100 ^oC in the presence of quartz chips and glass chips. Under an alkaline pH of 9 dissolution of silica occurs and is incorporated into the hydrous zirconia. The effect of silica on zirconia is studied. The undigested ZrO_2 crystallized predominantly in the monoclinic phase (Fig. 3-30). The percentage of monoclinic was 79.5% (Table 3-7). In the quartz-series, Q-1-500 had about 65.5% monoclinic phase, but this percentage decreased with digestion time. Pure tetragonal phase was observed in sample Q-8-500, that had been digested for 8 days. The same trend was observed for samples digested with glass chips. The monoclinic phase

decreased from 64.6% in G-1-500 to 18.6% after only 2-days digestion. After 4 days digestion, pure tetragonal zirconia was formed. A longer digestion time of 8 days resulted in amorphous zirconia. A comparison of the effect of quartz and glass chips on the crystal phase is given in Fig. 3-32. Glass has a bigger influence on the formation of tetragonal phase. This may be due to the other components present in glass besides silica, like boron, calcium and aluminium. The effect of dopants in favoring the tetragonal phase of zirconia is known [124, 125]. The weight loss per day for the glass chips was higher than that of quartz chips (Table 3-8).

ICP analysis showed that the dissolved silicon was taken up by the hydrous zirconia during digestion (Table 3-7). Whilst no silicon was detected in the undigested zirconia, between 0.45 to 2.85 wt% Si was measured in the samples digested in the presence of glass chips. The uptake of Si was lower in the quartz-series, with Si content of 0.24-1.12 wt%.

The effect of Si on the surface area and pore volume of hydrous zirconia is given in Table 3-9. Hydrous zirconia containing silicon had surface areas of 353-430 m^2/g as compared to 234 m^2/g in the pure hydrous zirconia. The porosity of these hydrous zirconias was also higher by up to five times. The pore volume increased from 0.17 cc/g in 0-100 to 0.85 cc/g in G-8-100. Similarly, in the quartz series, the pore volume of Q-8-100 was 0.76 cc/g.

Calcination at 500 ^oC resulted in the formation of zirconia. Zirconia formed from the undigested hydrous zirconia had a surface area of only 47.1 m^2/g. However, zirconia from the glass-series had surface area of 68.7 to 245 m^2/g. The surface area increased

with the length of digestion of the hydrous zirconia. In the quartz-series, the surface area, 172 m^2/g, was also higher than 0-100, 74.1 m^2/g. The porosity of silica-containing zirconia is higher than that of pure zirconia. The silica-containing zirconia had pore volumes of 0.30-0.62 cc/g as compared to 0.13 cc/g in the pure zirconia.

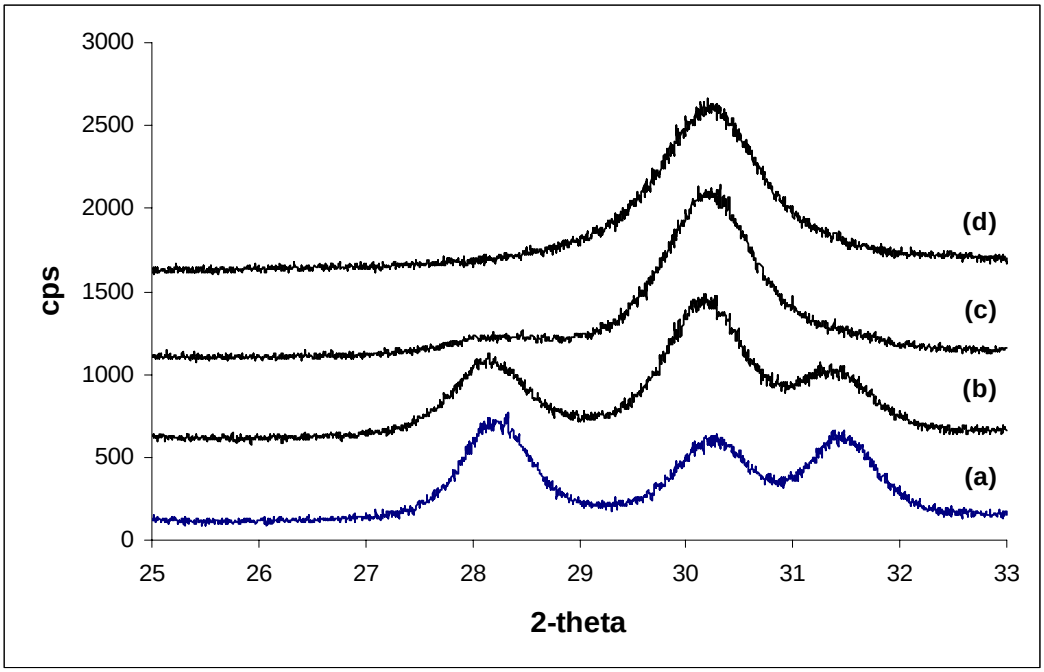

Fig. 3-30 XRD of (a) Q-1-500, (b) Q-2-500, (c) Q-4-500 and (d) Q-8-500.

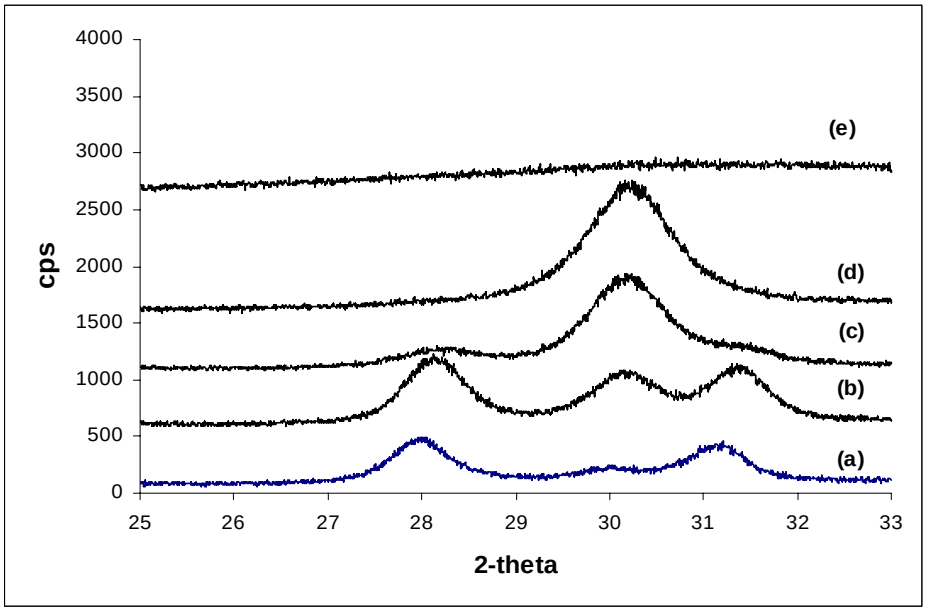

Fig. 3-31 XRD of (a) 0-500, (b) G-1-500, (c) G-2-500, (d) G-4-500 and (e) G-8-500.

Table 3-7 Microstructural parameters for calcined ZrO_2 samples

Catalyst	Crystal type	D (Å)	%T	%M	Si (wt%)
0-500	M	123	20.5	79.5	0.00
	T	82.4			
Q-1-500	M	119	34.5	65.5	0.00
	T	109			
Q-2-500	M	108	56.3	43.7	0.24
	T	103			
Q-4-500	M	90.5	90.2	9.8	0.35
	T	88.0			
Q-8-500	T	76.6	100	0	1.12
G-1-500	M	118	35.4	64.6	0.45
	T	103			
G-2-500	M	91.1	81.5	18.6	1.33
	T	90.6			
G-4-500	T	81.9	100	0	1.40
G-8-500	Amorphous	-	-	-	2.85

M = Monoclinic, T = Tetragonal

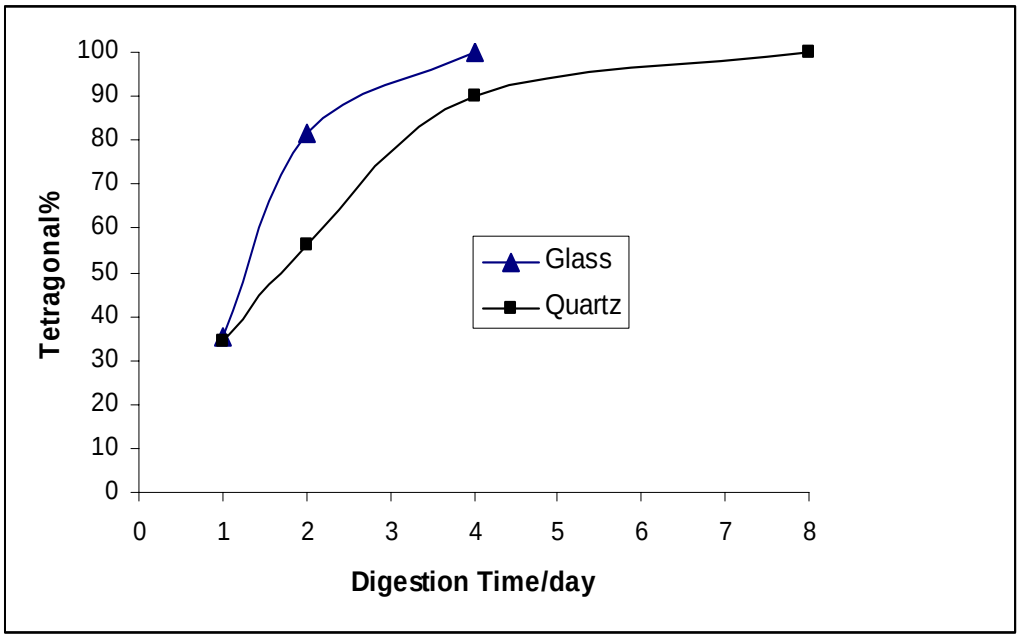

Fig. 3-32 % Tetragonal phase vs. digestion time

Table 3-8 Weight loss of glass and quartz during digestion

	Before digestion/g	After 8 days digestion/g	Weight loss/g	Weight loss per day/g
Glass	31.9720	31.6832	0.2888	0.0361
Quartz	31.9205	31.7590	0.1615	0.0201

Table 3-9 BET surface area and pore volume of hydrous ZrO_2 digested with glass and quartz.

Hydrous ZrO_2	Surface Area (m^2/g)	Pore Volume (cc/g)
0-100	234	0.17
G-1-100	353	0.44
G-2-100	386	0.57
G-4-100	409	0.70
G-8-100	430	0.85
Q-1-100	382	0.54
Q-2-100	383	0.59
Q-4-100	387	0.66
Q-8-100	394	0.76

Table 3-10 BET surface area, pore volume and amount of silica of ZrO_2 digested with glass and quartz.

ZrO_2	Surface Area (m^2/g)	Pore Volume (cc/g)
0-500	47.1	0.13
G-1-500	68.7	0.30
G-2-500	105	0.35
G-4-500	166	0.46
G-8-500	254	0.62
Q-1-500	74.1	0.36
Q-2-500	96.8	0.40
Q-4-500	116	0.43
Q-8-500	172	0.49

Conclusion

1. MSU-S aluminosilicates were formed using HY and BEA zeolite seeds. The lattice spacing, a_o, decreased with higher Al content. The surface area of these mesoporous materials was higher, in the order of 800-1000 m^2/g. About 10% of the surface is due to microporous. NMR analysis showed that most of the Al was incorporated into the framework. The ratio of tetrahedrally coordinated Al to extraframework Al decreased with higher Si/Al ratio for MSU-S_{HY}. Pyridine adsorption studies found that only Lewis acidity was present in these samples.

2. Al-MCM-41(70) showed the presence of both Brønsted and Lewis acidity. Only tetrahedrally-bonded Al was detected in this sample.

3. In the B_2O_3/SiO_2 samples, increasing B_2O_3 loading decreased the surface area and pore volume. B_2O_3 was present in the hydrated form, H_3BO_3, on the prepared samples. Both BO_3 and BO_4 units were detected by NMR studies. However, the proportion of tetrahedrally coordinated boron could be reduced by drying at 100 ^oC. The boron- oxide/SiO_2 samples showed strong Lewis acidity. Brønsted acidity was measured in samples with boron oxide loading of 15 wt% and higher.

4. $InCl_3/Zr(OH)_4$ catalysts were X-ray amorphous for loadings up to 4 mmol $InCl_3$/g $Zr(OH)_4$. The samples showed both Lewis and Brønsted acidity.

5. Si-incorporation into hydrous zirconia resulted in high surface area and increase in pore volume. Despite calcination at high temperatures, the high surface area and porosity were retained. The presence of Si also favors the formation of the tetragonal phase.

CHAPTER IV

RESULTS AND DISCUSSION

CATALYTIC STUDIES

4.1 α-Pinene Oxide Isomerization Reaction

Earlier work of other research groups on the acid catalyzed rearrangement of α-pinene oxide showed the potential of solid Lewis acids to promote the selective formation of campholenic aldehyde [102,108,126]. Lewis acids, especially the zinc halides, can give selectivity as high as 85% towards campholenic aldehyde. Recently, Hölderich et al. [108] reported a selectivity to campholenic aldehyde of 78% by using a carefully prepared H-US-Y zeolite at 0 ^{o}C. The authors claimed that the high selectivity observed was a result of well-dispersed Lewis acid sites on the catalyst. Zeolite HY has a three-dimensional pore system of 7.4 Å with super cages of 12 Å. The larger pore system allows a good diffusion of the reactants into the channel system.

4.1.1 Catalytic Activity of HY Zeolites

Based on these former studies, α-pinene oxide isomerization reaction was carried out over HY zeolite (Zeolyst) with different Si/Al ratio (10.4, 24 and 60). Before the reaction, the catalysts were calcined at 550 ^{o}C for 8 h to decompose NH_4^+ to H^+. HY zeolite with Si/Al =10.4 was the most active for the reaction (Fig. 4-1). After 4 h, the conversion reached ~100% at room temperature. The conversion decreased with increasing Si/Al ratio. For HY with Si/Al = 24 and 60, the conversion after 8 h was 100% and 61%, respectively. Treatment of HY (Si/Al = 60) with dilute HCl may result in either removal of Al or removal of extraframework silica. In the case of the former, the acidity of the catalyst would be lowered and consequently, a less active

catalyst may result. If extraframework silica is removed, then an increase in activity may actually occur as the active sites are exposed following the removal of the extraneous silica. Hölderich et al. [108] had observed an increased in activity in the HCl-treated catalyst although the selectivity to campholenic aldehyde remained unchanged at ~ 68%. The authors used a HY sample with very low Si/Al (140). The improvement in activity was attributed to the removal of silica species which were blocking the catalytically active sites. However, in the present study, it was found that the activity of the HCl-treated HY (Si/Al 60) was similar to that of the untreated catalyst (Table 4-1).

The selectivity to campholenic aldehyde was highest over HY with Si/Al = 60. With higher Al content, the selectivity over the HY catalysts decreased from 66% in HY (Si/Al = 60) to 49% in HY (Si/Al = 10.4). The initial selectivity of the catalysts was higher. For HY (Si/Al = 60), a selectivity 73% was measured after 30 min but it decreased with time. Both HY (Si/Al = 24) and HY (Si/Al = 10.4) suffered bigger decrease in selectivity with time than HY (Si/Al = 60). HCl-treatment did not affect the selectivity of the catalyst to campholenic aldehyde (Fig. 4-2). Zeolite Beta (Si/Al =50) showed similar conversion and selectivity as that of HY (Si/Al = 60). There was a decrease in the initial selectivity but after 1 h, the selectivity to campholenic aldehyde remained constant at 52%. Over the zeolite catalysts, the other products formed besides campholenic aldehyde, were isomeric aldehyde (16%), *trans*-carveol (8%), isopinocamphone (6%), *p*-cymene (3%) and *trans*-sobrerol (3%).

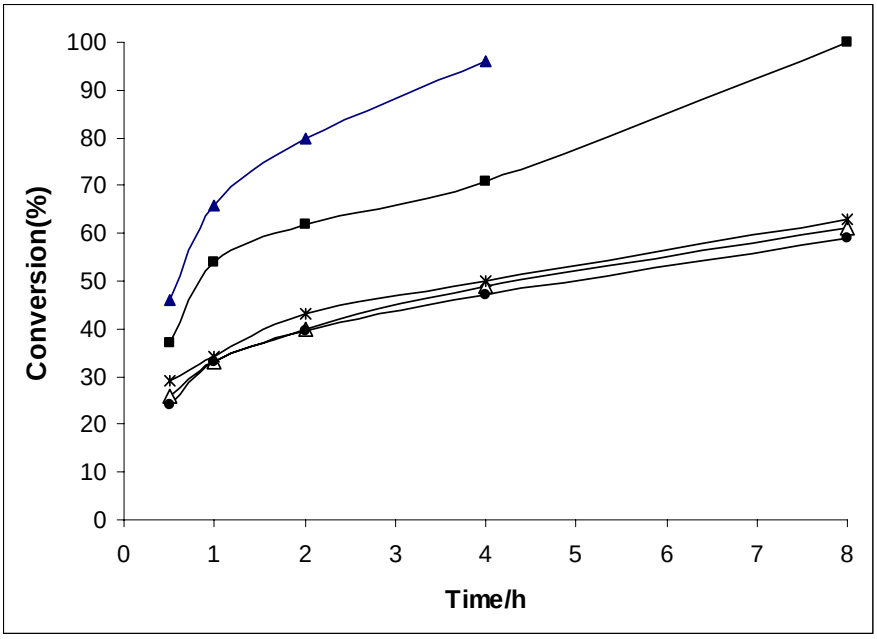

Fig. 4-1 Conversion of α-pinene oxide versus reaction time at room temperature. Over (●) HCl-treated HY (Si/Al=60), (Δ) HY (Si/Al=60), (ж) H-Beta (Si/Al =50), (■) HY (Si/Al = 24), (▲) HY (Si/Al = 10.4).

Table 4-1 Conversion, selectivity and yield over HY zeolites and H-Beta after 4 h at room temperature in toluene.

Catalyst	Conversion (%)	Selectivity (%)[a]	Yield (%)
HY (Si/Al =10.4)	96	49	47
HY (Si/Al = 24)	71	51	36
HY (Si/Al = 60)	49	66	32
HY (Si/Al = 60)[b]	47	66	31
H-Beta (Si/Al = 50)	50	52	26

a = selectivity towards campholenic aldehyde, b = HCl-treated.

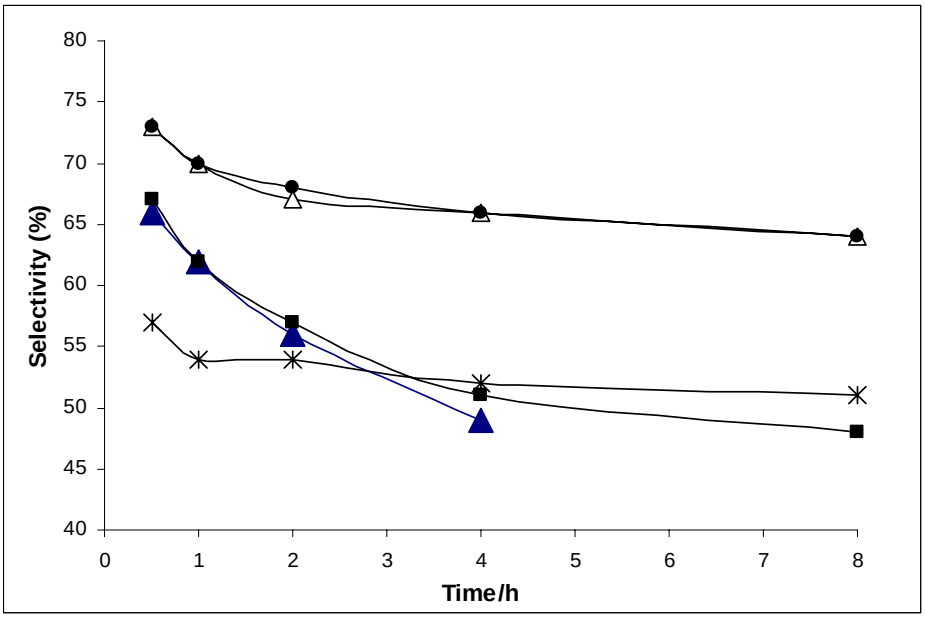

Fig. 4-2 Selectivity versus time at room temperature. (●) HCl-treated HY (Si/Al=60), (Δ) HY (Si/Al=60), (ж) H-Beta (Si/Al =50), (■) HY (Si/Al = 24), (▲) HY (Si/Al = 10.4).

4.1.2 Catalytic Activity of MSU-S Materials

In the next step of this study, the isomerization of α-pinene oxide to campholenic aldehyde was studied over a number of micro- and mesoporous catalysts, the so-called MSU-S materials. MSU-S_{HY} with Si/Al 25 to 70, MSU-S_{BEA}(67), and Al-MCM-41(70) were compared for their catalytic activity.

Effect of Si/Al Ratio and Nature of Mesoporous Materials

Over the MSU_{HY} materials (Fig. 4-3), the catalyst with Si/Al = 25 was the most active. After 1 h reaction, the conversion was ~70%, while for MSU-S_{HY}(50) and MSU-S_{HY}(70), the conversion was ~52% and 34%, respectively. After 8 h, the conversion of MSU-S_{HY}(50) and MSU-S_{HY}(70) reached 74% and 69%, respectively (Table 4-2).

Table 4-2 Selectivity to campholenic aldehyde over various catalysts

Catalyst	Selectivity (%)[a]	Selectivity (%)[b]
MSU-S_{HY} (25)	75	73
MSU-S_{HY}(50)	86	76
MSU-S_{HY}(70)	100	86
MSU-S_{HY}(70)[c]	100	100
MSU-S_{BEA}(67)	87	76
Al-MCM-41(70)	72	53

[a] after 0.5 h, [b] after 8 h, [c] HCl-treated. Reaction at room temperature

The selectivity to campholenic aldehyde showed a reverse trend to the activity, increasing from MSU-S_{HY}(25) to MSU-S_{HY}(70). At reaction times of 1 h or shorter, both MSU-S_{HY}(50) and MSU-S_{HY}(25) had selectivity to campholenic aldehyde of ~ 85%. For MSU-S_{HY}(70), the only product formed was campholenic aldehyde (Fig. 4-4). Such high selectivity for α-pinene oxide isomerization has not been reported before. Indeed, over MSU-S_{HY}(70), 100% selectivity was maintained for up to 2 h reaction time. With longer times, the selectivity decreased (Fig. 4-5). For MSU-S_{HY}(25) and MSU-S_{HY}(50), the selectivity decreased to 73-76% while for MSU-S_{HY}(70), the selectivity was 86%.

While many other products besides campholenic aldehyde have been observed over acid catalysts [108], the number of isomers formed over MSU-S_{HY} materials was very much reduced. In zeolite HY, five other isomers were observed besides the desired aldehyde. In MSU-S_{HY}(25), isomeric aldehyde constituted 17% of the products while isopinocamphone formed 10% of the total products. For MSU-S_{HY}(50), the selectivity to isomeric aldehyde and isopinocamphone was 13% and 11% respectively.

HCl-treated MSU-S_{HY}(70) had a lower activity than the untreated MSU-S_{HY}(70). After 8 h, the conversion was only 47% as compared to 69% in MSU-S_{HY}(70). This is in contrast to the microporous HY zeolites where no change in activity occurred. The results suggest that some dealumination had occurred with acid treatment. However, the selectivity to campholenic aldehyde over the HCl-treated MSU_{HY}(70) was unchanged, at 100%. Interestingly, the selectivity remained unchanged with reaction time so that even after 8 h reaction, campholenic aldehyde was the only product formed.

MSU-S_{BEA}(67) was not as active of MSU-S_{HY}(70). The conversion closely parallels that of the HCl-treated MSU_{HY}(70). The initial selectivity was high, around 88% but decreased with longer reaction time to 76%. Al-MCM-41(70) was more active than the MSU-S materials with similar Si/Al ratio although its activity was less than that of MSU-S_{HY}(25). The selectivity for campholenic aldehyde was the lowest of the materials tested here. Its initial selectivity was 72% but this decreased to 53% after 8 h.

The high selectivity to campholenic aldehyde over MSU-S_{HY} catalysts may be due to the mixture of microporosity and mesoporosity inherent in these compounds. The walls of MSU materials have microporous channels of zeolitic nature where those of zeolite HY have been found to be most ideal for the isomerization of α-pinene oxide [108]. Reaction can occur within the micropores but due to the thinness of the walls, the diffusion length is short and the formed product can diffuse away from the active site before further reaction to other isomers occurs. The formation of the other isomers at longer reaction times indicates that subsequent isomerization of

campholenic aldehyde occurs in a consecutive reaction. In Al-MCM-41(70), the mesoporous channels allow a fast rate of reaction but poor selectivity.

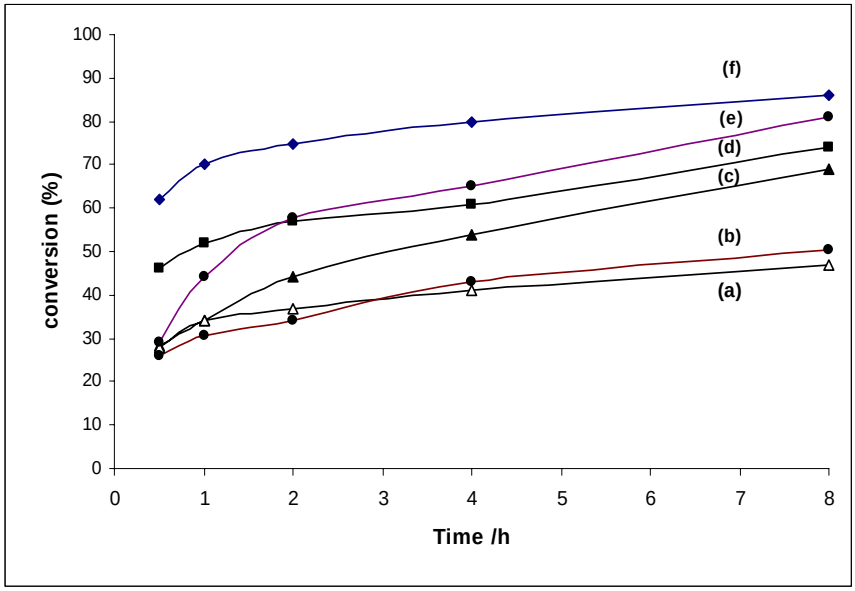

Fig. 4-3 Conversion of α-pinene oxide versus reaction time for (a) HCl-treated MSU-S_{HY}(70), (b) MSU-S_{BEA}(67), (c) MSU-S_{HY}(70), (d) MSU-S_{HY}(50), (e) Al-MCM-41(70) and (f) MSU-S_{HY}(25) at room temperature in toluene.

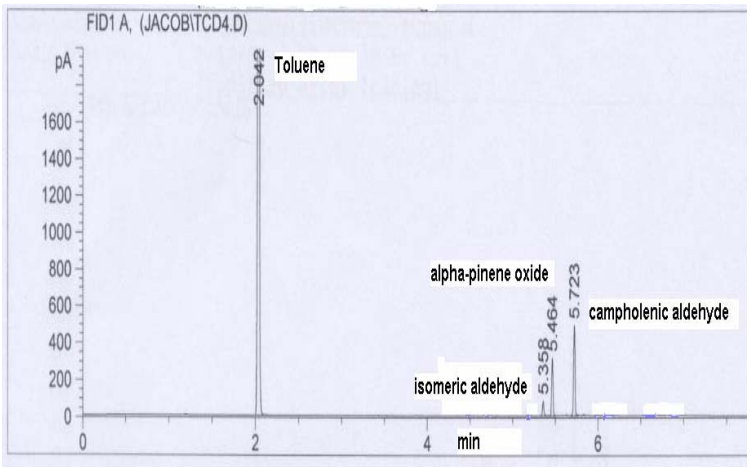

Fig. 4-4 Gas chromatogram of α-pinene oxide isomerization reaction over MSU-S_{HY}(70) after 8 h at room temperature in toluene.

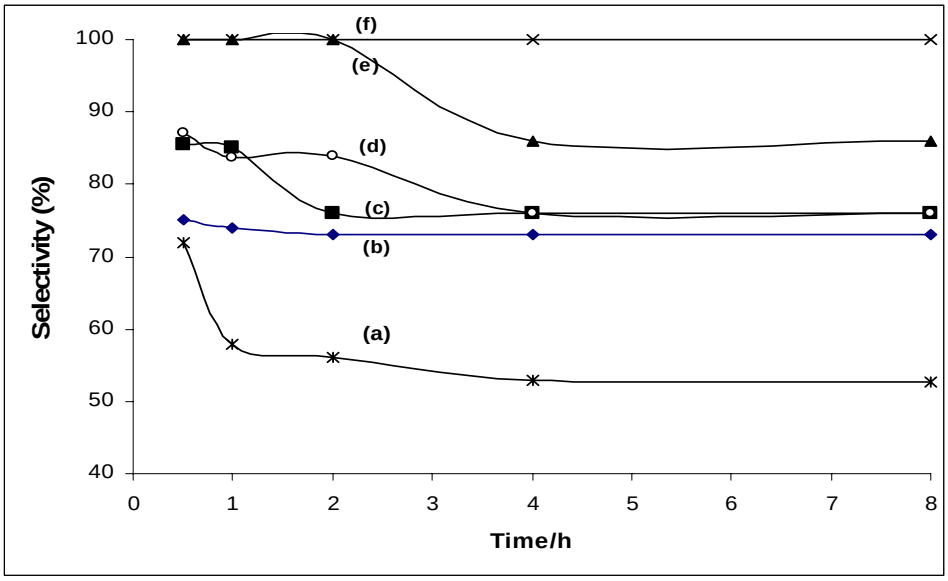

Fig. 4-5 Selectivity to campholenic aldehyde versus reaction time for (a) Al-MCM-41(70), (b) MSU-S_{HY}(25), (c) MSU-S_{HY}(50), (d) MSU-S_{BEA}(67), (e) MSU-S_{HY}(70) and (f) HCl-treated MSU-S_{HY}(70) at room temperature in toluene.

Effect of Temperature

Fig. 4-6 shows the conversion, selectivity and yield to campholenic aldehyde at 0 ^{o}C, 25 ^{o}C, and 50 ^{o}C over MSU-S_{HY}(70). The selectivity increased from 65 % at 50 ^{o}C to 100 % at 0 ^{o}C. However, the conversion at 0 ^{o}C was very slow and after 8 h reached a limiting value of ~30 %. In contrast, at 50 ^{o}C, 100 % conversion was achieved. Two by-products, isomeric aldehyde (18%) and isopinocamphone (17 %) were also formed at this temperature. The yield increased with increase of temperature from: 30% at 0 ^{o}C to 65% at 50 ^{o}C.

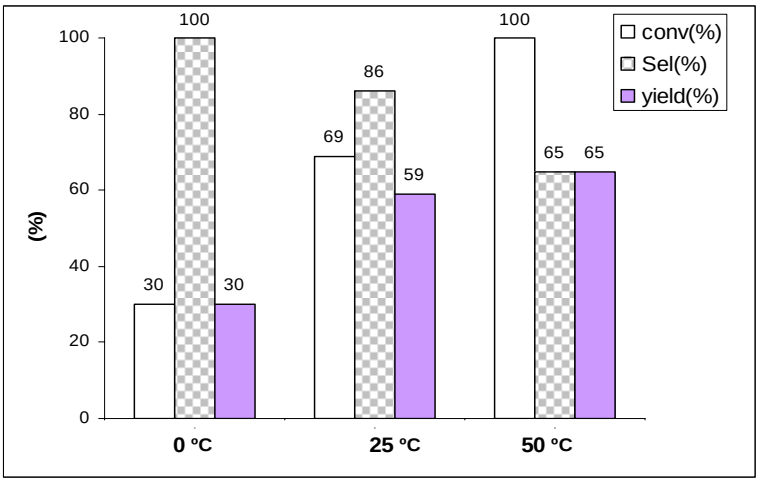

Fig. 4-6 Effect of temperature on activity, selectivity, and yield towards campholenic aldehyde over MSU-S_{HY}(70) (At 0 °C and 25 °C the selectivity and conversion were measured after 8 h. At 50 °C the selectivity and conversion were measured after 6 h)

The activation energy, E_a for the reaction was calculated using Arrhenius equation. The calculated activation energy, E_a = 35.05 kJmol^{-1}. The activation energy, E_a was calculated as follows:

For 1st order reaction, $[I]_t = [I]_o e^{-kt}$ (1)

where

$[I]_t$ = concentration of I after time t, $[I]_o$ = Initial concentration of I

k = rate coefficient, t = residence time

However, $conversion = 1 - \frac{[I]_t}{[I]_o} = 1 - e^{-kt}$ (2)

$\therefore \ln[1 - conversion] = -kt$ (3)

$\ln[-\ln(1 - conversion)] = \ln kt$ (4)

From Arrhenius equation $kt = Ae^{\frac{-E_a}{RT}}$ (5)

$$\therefore \ln[kt] = \ln[A] - \frac{E_a}{RT} \quad (6)$$

From (4) $\ln[-\ln(1-conversion)] = \ln(A) - \frac{E_a}{RT}$ (7)

Plotting ln[-ln(1-conversion)] vs 1/T, the gradient gives the value of E_a/R from which the activation energy can be calculated (Fig. 4-7).

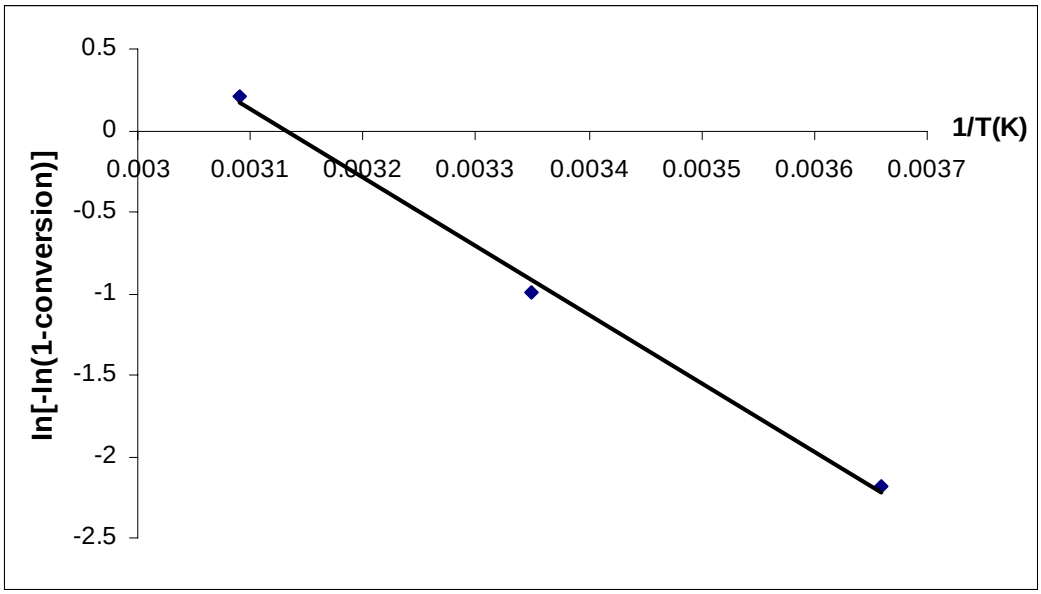

Fig. 4-7 Plot of ln[-ln(1-conversion)] vs 1/T after 1 h reaction time

Effect of Solvent

The effect of various solvents on the selectivity and the activity over MSU-S_{HY}(70) at room temperature was investigated (Table 4-3). The solvent employed has a big impact on the selectivity and activity. In toluene, after 2 h, the conversion was 44% and the selectivity to campholenic aldehyde was 100%. In contrast, the conversion was only 26% after 2 h when 1, 2-dichloroethane was the solvent. The selectivity to campholenic aldehyde was lower than in toluene, 74%. When solvents with high dipolar moments were used such as 2-propanol, 1,2-dichlorobenzene and sulfolane, the conversion was higher than in toluene or 1,2-dichloroethane, between 77-95%.

However, the selectivity to campholenic aldehyde was lower, 43-54%. Other isomers such as isopinocamphone, *trans*-sobrerol, *p*-cymene and isomeric aldehyde were produced.

Table 4-3 Effect of various solvents for α-pinene oxide isomerization over MSU-S_{HY} (70) at room temperature.

Solvent	Dipole Moment (D)	Conv. (%) (a)	Sel. (b)	Sel. (c)	Sel. (d)	Sel. (e)	Sel. (f)	Sel. (g)	Sel. (h)
Toluene	0.34	44	100	-	-	-	-	-	-
1,2 dichloro ethane	0.70	26	74	14.6	-	11.4	-	-	-
2-propanol	1. 66	77	43	23	-	17.4	-	-	16.6
1,2 dichloro benzene	2.5	95	53	-	-	-	-	5.8	41.2
Sulfolane	4.6	89	54	-	-	-	-	18.4	11.1

(a) after 2 h, selectivity towards (b) campholenic aldehyde, (c) isopinocamphone, (d) *trans*–carveol (e) p-cymene (f) *trans*-sobrerol (g) isomeric aldehyde (h) others

The effect of various solvents on the activity and selectivity of the isomerization reaction may be explained by varying adsorption of solvent into the microporous system of the MSU-S, hence affecting the α-pinene oxide concentration. This effect has been observed over Ti-Beta where the hydrophobicity of the sample resulted in preferential adsorption of less polar molecules over more polar molecules [102]. Hence, the α-pinene oxide concentration in the micropores was low resulting is a low activity. In more polar solvents, the initial rate was higher but the catalyst rapidly deactivated due to bimolecular reaction between the α-pinene oxides. In the MSU-S

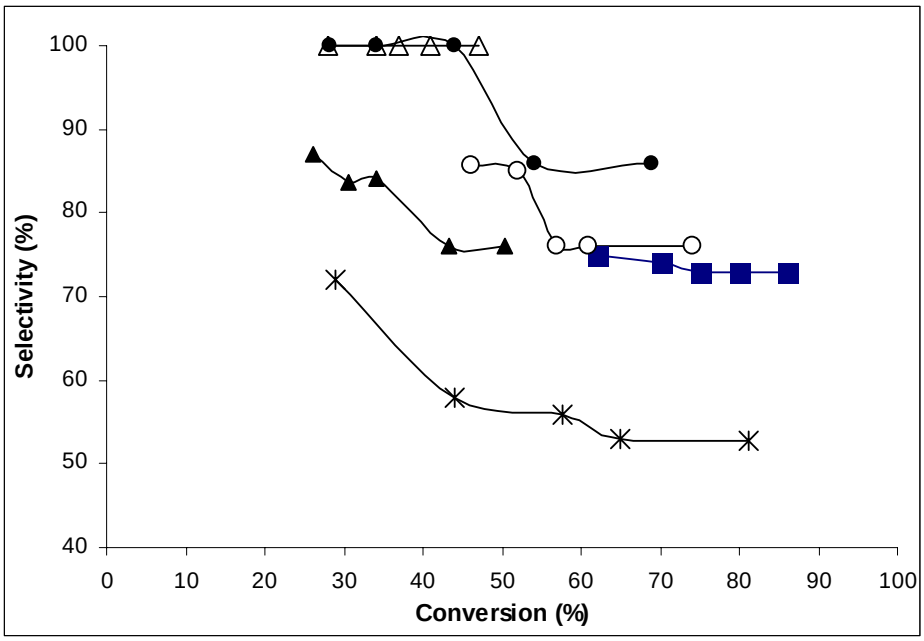

Fig. 4-8 Selectivity versus conversion at room temperature in toluene over (Δ) HCl-treated MSU-S_{HY}(70), (●) MSU-S_{HY}(70), (▲) MSU-S_{BEA}(67), (○) MSU-S_{HY}(50), (■) MSU-S_{HY}(25) and (Ж) Al-MCM-41(70).

materials, the higher rate of reaction in polar solvents did not lead to deactivation of the catalyst. Close to 100% conversion was reached after 4-6 h; this fast rate of reaction may be a result of the polar solvents favoring a higher concentration of α-pinene oxide in the micropores. The build-up of campholenic aldehyde in the micropores may lead to subsequent isomerization to less desired products. Although the microporous channels are shorter than in zeolite, diffusion away from the active sites may still be limiting when the reaction rate is fast. A plot of activity versus selectivity over MSU-S materials at room temperature in toluene shows that selectivity decreased when the activity is increased above 40% (Fig. 4-8). When 2-propanol was used as solvent, the selectivity was lowest and this may be due to the transformation of the Lewis acid site into a Brønsted acid site by coordination of alcohol [102].

Deactivation of Catalyst

In order to investigate the reuseability of the MSU-S materials, MSU-S_{HY}(25) catalyst was recovered after 8 h reaction and regenerated by calcining in air at 550 ^{o}C for 8 h. The sample before regeneration was white, as before the reaction, showing the absence of any organic residues. The regenerated catalyst was tested in two further rounds of reaction. The activity for the fresh catalyst after 8 h was 86% while for the one- and two-time regenerated catalysts, the activity was slightly lower at 81% and 76%, respectively (Fig. 4-9). The selectivity to campholenic aldehyde also decreased (Fig. 4-10). The only by-products formed over the fresh MSU-S_{HY}(25) were isomeric aldehyde and isopinocamphone. However, over the regenerated MSU-S_{HY}(25), two other side-products besides isomeric aldehyde and isopinocamphone were formed, *trans*-sobrerol and *trans-carveol*. After the first regeneration, *trans*-sobrerol and *trans*-carveol were formed with selectivity 5% and 2%, respectively. After the second regeneration, the selectivity to *trans*-sobrerol was increased to 7% while *trans*-carveol remained at 2%. The selectivity to isomeric aldehyde remained constant.

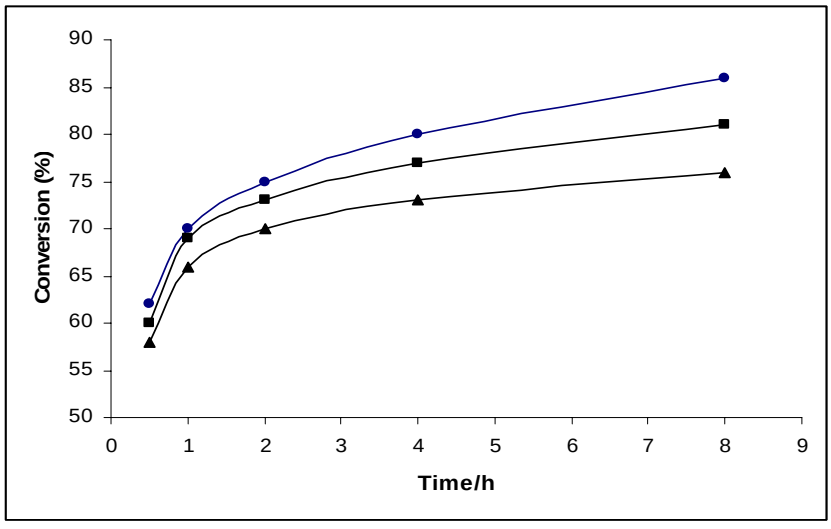

Fig. 4-9 Conversion at room temperature versus time for (●) fresh MSU-S_{HY}(25) and after (■) one and (▲) two regenerations in air at 550 ^{o}C for 8 h

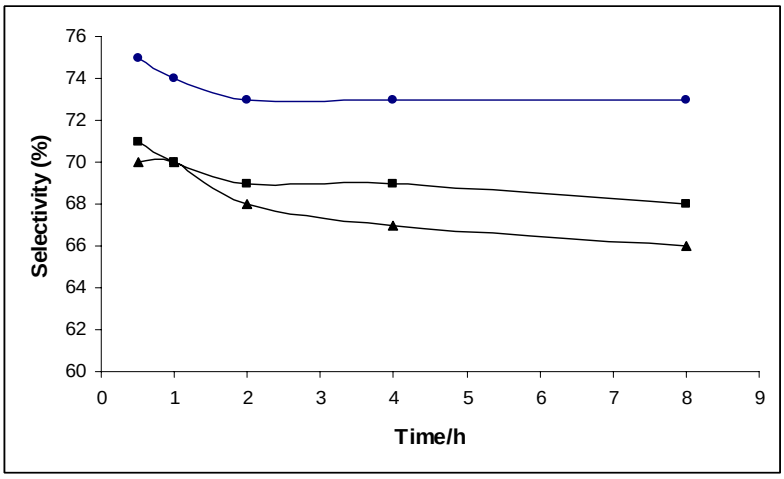

Fig. 4-10 Selectivity to campholenic aldehyde at room temperature versus time for (●) fresh MSU-S_{HY}(25) and after (■) one (▲) two regenerations in air at 550 ^{o}C for 8 h.

4.1.3 Catalytic Activity of Metal Oxides-Supported Boron Oxide

The effect of different supports was investigated for the isomerization of α-pinene oxide reaction using 15 wt% boria loading on ZrO_2, TiO_2, Al_2O_3 and SiO_2.

Effects of Support and Boria Oxide Loading

Table 4-4 compares the performance of boron oxide supported on various metal oxides for the isomerization reaction. SiO_2 itself has very poor activity. After 8 h, only 4% conversion was attained. However, the main product was campholenic aldehyde, with selectivity 76%. When 15 wt% boron oxide was impregnated on the support, the conversion increased to 65% after 8 h with a selectivity of 69%. 15 wt% B_2O_3/TiO_2 gave a lower conversion 39%, with a selectivity of 60%. This may be to its low surface area, 39 m^2/g, compared to the rest. When ZrO_2 was used as the support, the catalyst was even less selective to campholenic aldehyde, 49%. B_2O_3/Al_2O_3 was the most active of the catalysts studied. The conversion was 95.4% after 8 h. However, the selectivity was only 59.5%. Both B_2O_3/ZrO_2 and B_2O_3/Al_2O_3 had *trans*-sobrerol as the main side-product, 13-18%.

As the silica-supported sample gave the highest yield of campholenic aldehyde, the effect of boron oxide loading was next investigated. The conversion increased with boron oxide loading and reached a maximum at 15 wt% loading (Fig. 4-11). Despite the increase in activity, the selectivity towards campholenic aldehyde was independent of boron oxide loading. At room temperature, the selectivity was around 70%. The side-products observed include isomeric aldehyde (12.5%), *p*-cymene (4.1%), isopinocamphone (7.3%), *trans*-carveol (4%) and *trans*-sobrerol (2.1%) (Fig. 4-12). The slightly lower selectivity of the boron oxide-containing samples as compared to SiO_2 may be due to the presence of Brønsted acidity in the former. From the IR pyridine adsorption studies, SiO_2 had only Lewis acid sites but Brønsted acidity was generated after impregnation with boron oxide. *Trans*-carveol, *trans*-sobrerol, and *p*-cymene are possible products of Brønsted acidity.

Table 4-4 Conversion and selectivity over different supported boron oxide catalysts.

Catalyst	Conversion (%)[a]	Selectivity (%)[b]	Yield(%)
SiO_2	4	76	3.04
5% B_2O_3/SiO_2	27	70	18.9
10% B_2O_3/SiO_2	55	69	37.9
15% B_2O_3/SiO_2	89	69	61.4
20% B_2O_3/SiO_2	65	69	44.8
15% B_2O_3/TiO_2	39	60	23.4
15% B_2O_3/ZrO_2	57	49	27.9
15% B_2O_3/Al_2O_3	95.4	59.5	56.8

[a]Reaction conditions: 1.5 g of α-pinene oxide and 0.15 g of catalyst in 6 g of toluene at room temperature after 8 h. [b]Selectivity towards campholenic aldehyde.

Effect of Temperature

Fig. 4-13 compares the activity, selectivity and yield of campholenic aldehyde over 15 wt% B_2O_3/SiO_2 after 8 h, using toluene as solvent. The selectivity to campholenic aldehyde increased from 64% at 50 ^oC to 71% at 0 ^oC. Even at 0 ^oC and 50 ^oC, the same by-products were observed. However, at 0 ^oC, the conversion reached a limiting value of around 46% after 8 h while 100% conversion was achieved at 50 ^oC after 8 h.

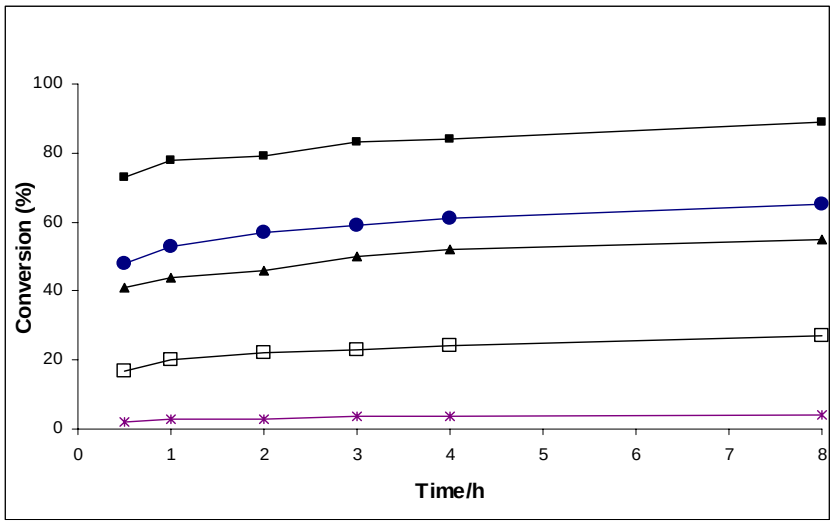

Fig. 4-11 Effect of boria loading on α-pinene oxide isomerization at room temperature over (ж) SiO_2, and (□) 5% B_2O_3/SiO_2, (▲) 10% B_2O_3/SiO_2, (●) 20% B_2O_3/SiO_2, (■) 15% B_2O_3/SiO_2

As such, the yield obtained at 0 ^oC was 32.7 % after 8 h while at room temperature and 50 ^oC, the higher yields 61% and 64%, respectively, were obtained. The activation energy of the isomerization reaction was calculated, 30.6 $kJmol^{-1}$ (Fig. 4-14). This is close to the value of 35.1 $kJmol^{-1}$ for MSU-S_{HY}.

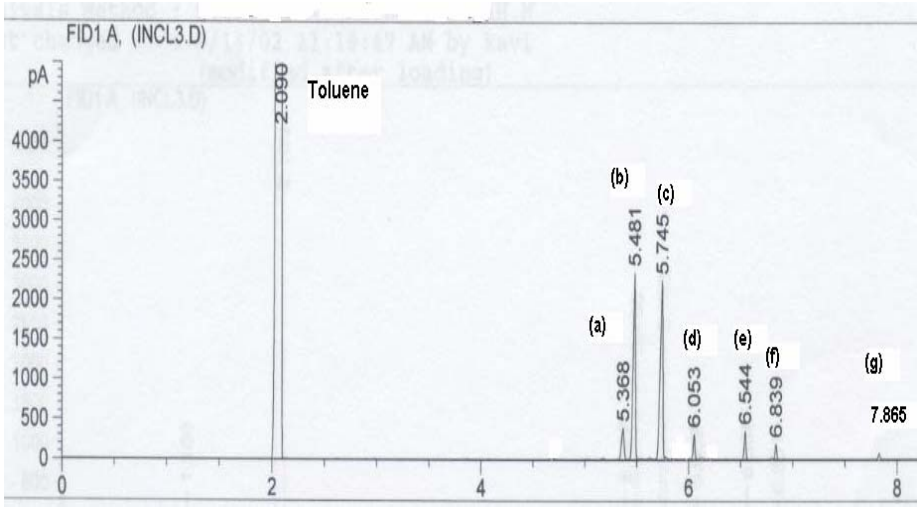

Fig. 4-12 Gas chromatogram for α-pinene oxide reaction over 15 wt% B_2O_3/SiO_2 in toluene after 8 h. (a) isomeric aldehyde, (b) α-pinene oxide, (c) campholenic aldehyde, (d) *p*-cymene, (e) isopinocamphone, (f) *trans*-carveol and (g) *trans*-sobrerol.

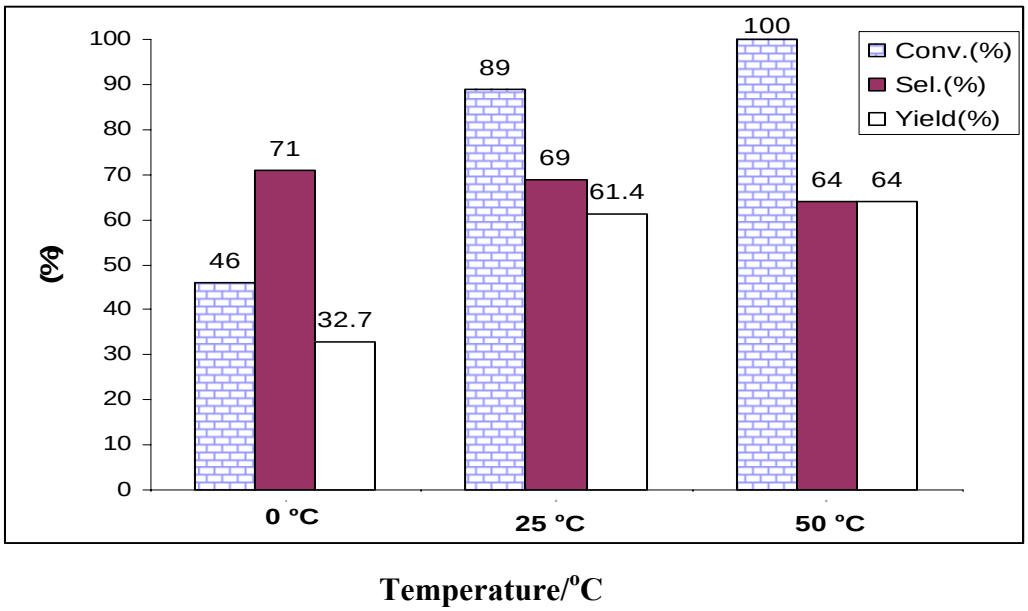

Fig. 4-13 Effect of temperature on activity, selectivity and yield to campholenic aldehyde after 8 h over 15 wt% B_2O_3/SiO_2.

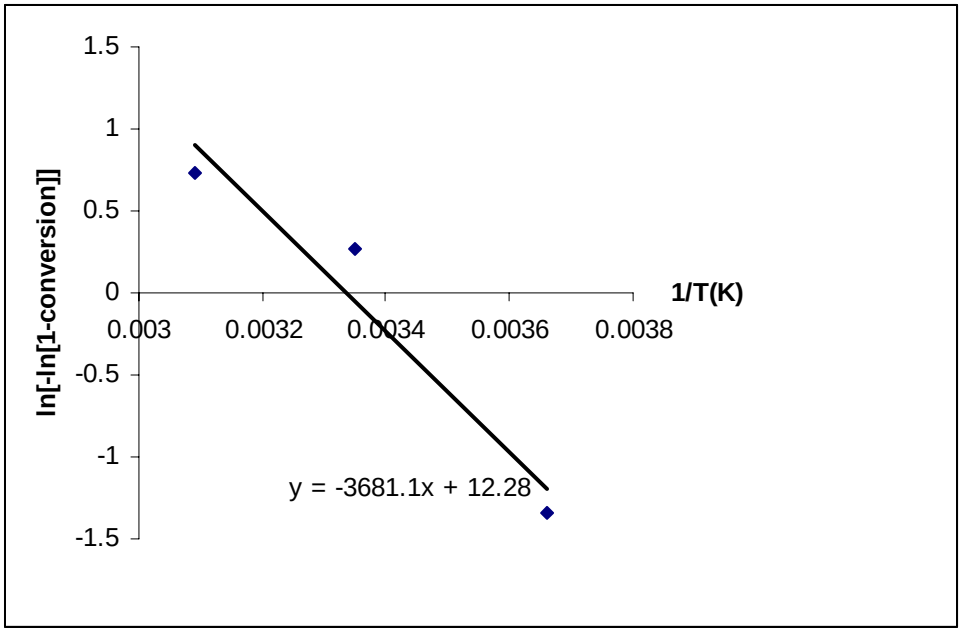

Fig. 4-14 Plot of ln[-ln[1-conversion]] vs 1/T(K)

Effect of Solvent

The effect of various solvents on the activity and selectivity over 15 wt%B_2O_3/SiO_2 was investigated at room temperature (Table 4-5). Both toluene and 1,2-dichloroethane with low polarity were good solvents; the yield of campholenic aldehyde was high for both these solvents, 62.3% and 56% respectively. However, 1,2-dichloroethane gave more by-products compared to toluene. For 2-propanol, the conversion as well as the selectivity towards the aldehyde was very low. The conversion and selectivity were 10% and 50% respectively. This could be due to the strong adsorption of the molecule to the Lewis acid site. More than ten side-products were observed. In polar solvents like 1,2-dichlorobenzene and sulfolane, the reaction rate was high especially in the latter. However, the selectivity in sulfolane was only 50%. The selectivity to campholenic aldehyde was highest when acetonitrile was the solvent, 76%.

Table 4-5 Effect of various solvents for α-pinene oxide isomerization over 15% B_2O_3/SiO_2 at room temperature.

Solvent	Dipole Moment (D)	Conv. (%) (a)	Sel. (%) (b)	Sel. (%) (c)	Sel. (%) (d)	Sel. (%) (e)	Sel. (%) (f)	Sel.(%) (g)	Sel. (%) (h)
Toluene	0.34	89	70	7.3	4.0	4.1	2.1	12.5	0
1,2 dichloro--ethane	0.70	80	70	8.0	5.4	2.4	0	11.2	3.0
2-propanol	1. 66	10	50	0	0	13	0	7.0	30
1,2 dichloro-benzene	2.5	94	68	9	8.5	0	0	14.5	3.0
Acetonitrile	3.44	30	76	4.5	8.7	5.0	5.8	0	0
Sulfolane	4.6	100[(i)]	50	2.7	0	14.7	7.5	6.3	18.8

(a) after 8 h. Selectivity towards (b) campholenic aldehyde, (c) isopinocamphone, (d) *trans* – carveol, (e) *p*-cymene, (f) *trans*-sobrerol, (g) isomeric aldehyde, (h) other by-products, (i) after 1 h

Deactivation of Catalyst

For all the B_2O_3/SiO_2 catalysts tested, the initial rate of rearrangement was very high (Fig. 4-11). However, the rate of conversion level off after ~ 2 h. The change of catalyst's colour from white to light yellow indicates deposition of organic by-products on the catalyst. In order to establish whether the deactivation was indeed due to pore blocking or covering of the active sites by organic products, a 15% B_2O_3/SiO_2 sample was recovered after reaction and regenerated by heating at 350 ^oC in air for 8 h. This process should remove organic materials from the catalysts. However, the colour of the catalyst changed from light yellow to light brown after heating, showing that the treatment temperature was inadequate for the oxidation and removal of the residues. A higher temperature was not used due to the low melting point of boron oxide at 450 ^oC. Melting of boron oxide would lead to change in the surface concentration and textural properties of the catalyst, rendering a comparison with the

fresh catalyst meaningless. The results showed the activity of regenerated catalyst was about three times lower compared to the fresh catalyst (Fig. 4-15). The selectivity was slightly reduced form ~ 70% to ~ 64% (Fig. 4-16). The catalyst was regenerated another time. The activity of the catalyst regenerated for the second time was reduced further. The highest conversion reached was 19.4% with 62% selectivity after 8 h. Hence, it is difficult to reuse the B_2O_3/SiO_2 catalyst.

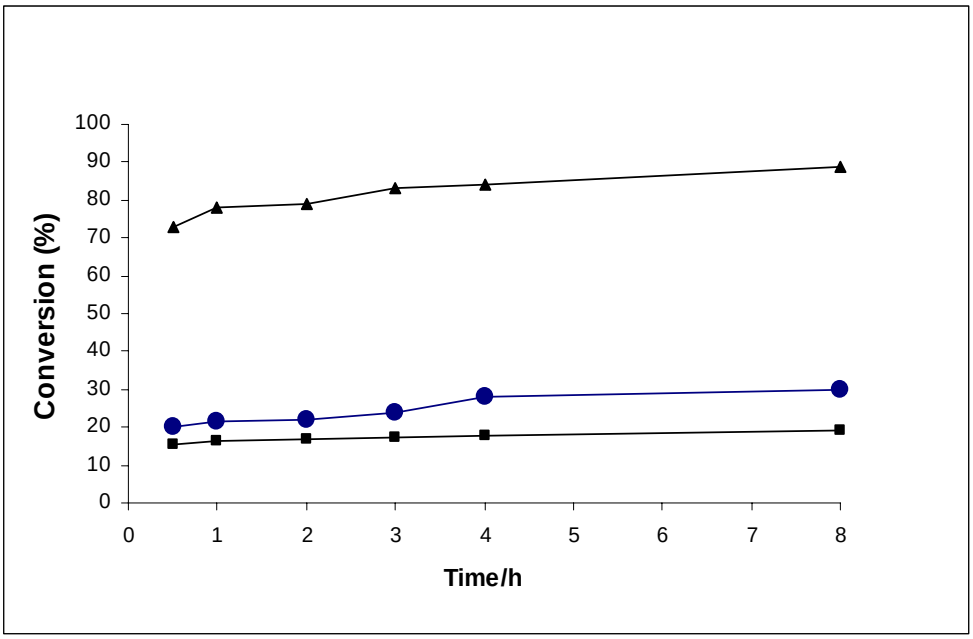

Fig. 4-15 Conversion versus time (▲) fresh 15% B_2O_3/SiO_2, and after (●) first time (■) second time regeneration in air at 350 ^oC for 8 h.

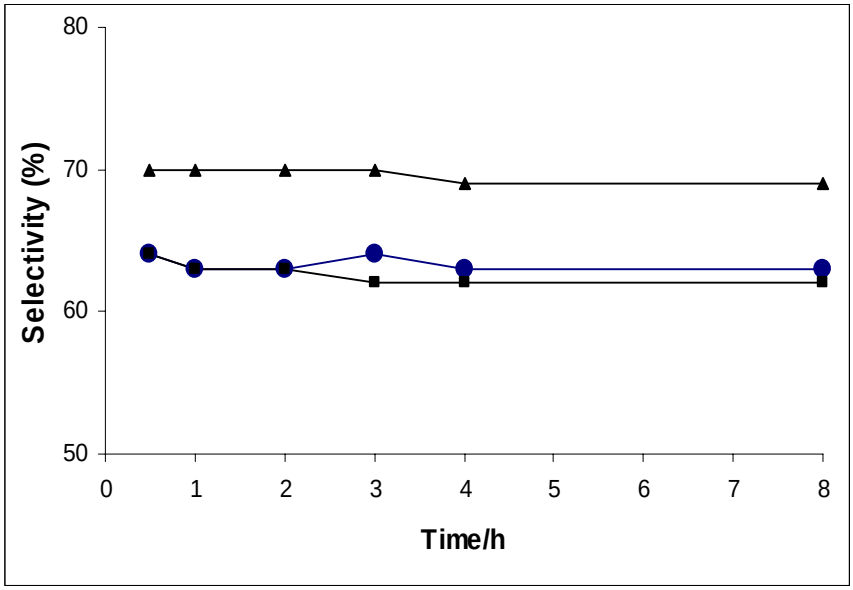

Fig. 4-16 Selectivity towards campholenic aldehyde versus time (▲) fresh 15% B_2O_3/SiO_2, and after (●) first time (■) second time regeneration in air at 350 ^oC for 8 h.

4.1.4 Catalytic Activity of $InCl_3$-Supported on ZrO_2

Table 4-6 α-Pinene oxide isomerization over $InCl_3$-supported on hydrous ZrO_2 and ZrO_2.

Catalysts	Conversion (%)*	Selectivity (%)[(a)]	Yield (%)
$Zr(OH)_4$	5.3	78	4.1
0.5 mmol $InCl_3$/g $Zr(OH)_4$	16	73	12
1 mmol $InCl_3$/g $Zr(OH)_4$	30	72	22
2 mmol $InCl_3$/g $Zr(OH)_4$	42	54	23
4 mmol $InCl_3$/g $Zr(OH)_4$	77	49	38
1 mmol $InCl_3$/g ZrO_2	18	46	8.3

*Reaction conditions : 1.5 g epoxide and 0.15 g catalyst in 6 g toluene after 24 h reaction time at room temperature. [a]towards campholenic aldehyde

$InCl_3$ was supported on hydrous zirconia and ZrO_2. The $InCl_3$ loading has a big effect on the activity and selectivity to campholenic aldehyde (Table 4-6). The conversion for hydrous ZrO_2 was only 5.3% after 24 h. The activity increased from 16% to 76.6% with increasing $InCl_3$ loading from 0.5 mmol to 4 mmol (Fig. 4-17). The conversion over 1 mmol $InCl_3$/g ZrO_2, 17.6%, was almost half that of 1 mmol $InCl_3$/g $Zr(OH)_4$, 30%.

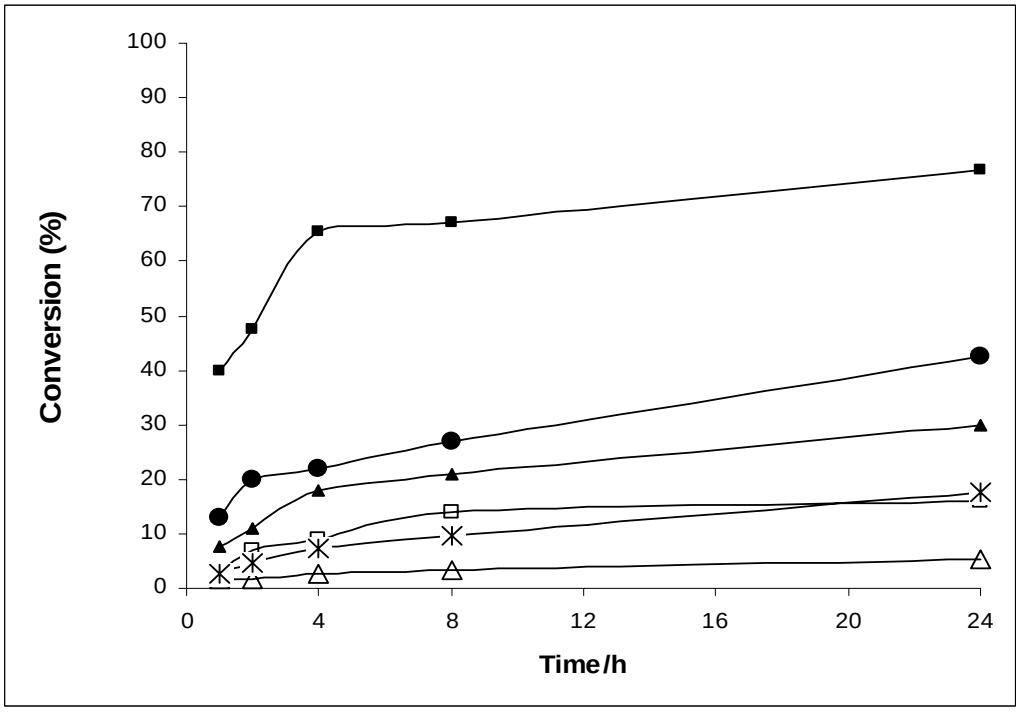

Fig. 4-17 Conversion of α-pinene oxide at room temperature in toluene over (Δ) $Zr(OH)_4$, mmol $InCl_3$/g $Zr(OH)_4$ with (□) 0.5 mmol $InCl_3$, (▲) 1 mmol $InCl_3$, (●) 2 mmol $InCl_3$, (■) 4 mmol $InCl_3$ and (ж) 1 mmol $InCl_3$/g ZrO_2.

While the isomerization of α-pinene oxide was enhanced by $InCl_3$ loading, the selectivity towards campholenic aldehyde decreased (Fig. 4-18). The support also plays a role besides the impregnated material. Compared to hydrous zirconia, ZrO_2 was a poorer support for the isomerization. A large number of by-products were observed for all the catalysts tested. The poor selectivity and large number of by-products may be due to the strongly Brønsted acidic nature of the samples. The yield after 24 h was highest for 4 mmol $InCl_3$/g $Zr(OH)_4$ and decreased with decreasing $InCl_3$ content. 4 mmol $InCl_3$/g $Zr(OH)_4$ had a yield of 38% while 0.5 mmol $InCl_3$/g $Zr(OH)_4$ had only 12% yield after 24 h. The high yield of 4 mmol $InCl_3$/g $Zr(OH)_4$ is due to its high activity.

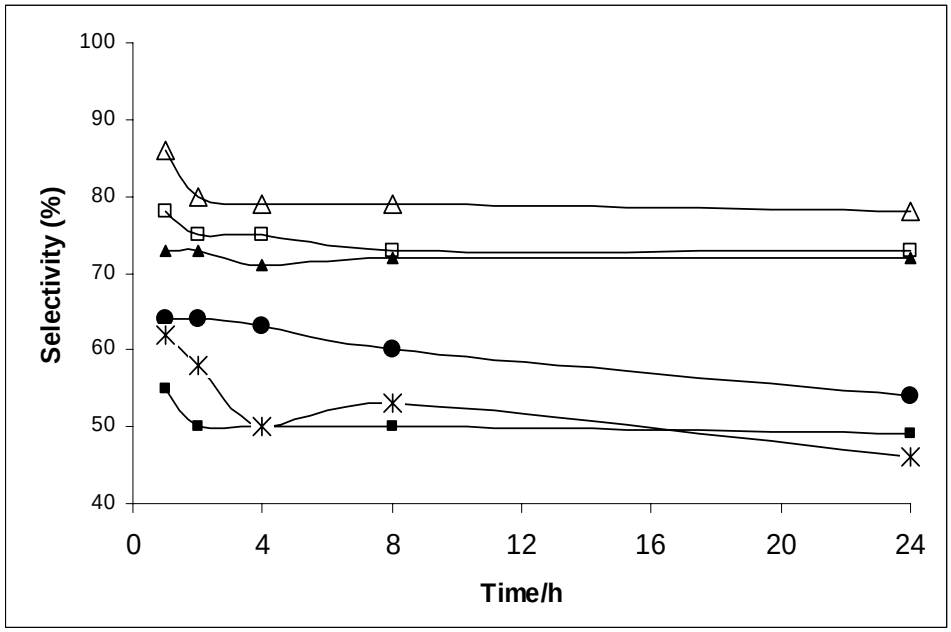

Fig. 4-18 Selectivity to campholenic aldehyde at room temperature in toluene over (Δ) $Zr(OH)_4$, mmol $InCl_3$/g $Zr(OH)_4$ with (□) 0.5 mmol $InCl_3$, (▲) 1 mmol $InCl_3$, (●) 2 mmol $InCl_3$, (■) 4 mmol $InCl_3$ and (ж) 1 mmol $InCl_3$/g ZrO_2.

4.1.5 Catalytic Activity of ZrO_2-Supported SiO_2 Catalysts

ZrO_2 containing silica was tested for α-pinene oxide rearrangement at room temperature in toluene. The results are summarized in Table 4-7. Zirconia is not a good catalyst for α-pinene oxide isomerization. Although the selectivity is high, above 70%, the activity is very low despite the high surface area of the material. The incorporation of silica into hydrous zirconia increased the conversion slightly. However, the selectivity decreased. Similarly, calcined zirconia and silica-containing zirconia had low activity and selectivity. Hence, these materials are not suitable as catalysts for α-pinene isomerization.

Table 4-7 α-Pinene oxide rearrangement over hydrous ZrO_2 and ZrO_2 digested with glass and quartz, at room temperature after 24 h in toluene.

Catalysts	Si (wt%)	Conversion (%)	Selectivity (%)[a]
Hydrous zirconia			
0-100	0.00	3.8	71
Q-8-100	1.12	4.2	59
G-8-100	2.85	10	53
Zirconia			
0-500	0.00	3.0	57
Q-4-500	0.35	3.4	57
G-4-500	1.40	6.2	53
Q-8-500	1.12	3.6	57
G-8-500	2.85	8.0	53

[a]selectivity towards campholenic aldehyde.

4.2 Liquid-Phase Beckmann Rearrangement of Cyclohexanone Oxime

The conventional liquid-phase Beckmann rearrangement of cyclohexanone oxime employs concentrated sulfuric acid as a catalyst. The fuming sulfuric acid makes this process environmentally unacceptable. For the vapor-phase Beckmann rearrangement of cyclohexanone oxime, many heterogeneous catalysts have been tested. These include silica-alumina [127], supported boron oxide [51, 55, 128], faujasite zeolite [129], pentasil zeolite [130-133], mesoporous MCM-41[134] and supported tantalum oxide [135]. However, the vapor-phase rearrangement over solid acid catalyst needs high reaction temperatures of 250 to 350 ^{o}C. Hence, side-products which are difficult to purify tend to be formed and rapid catalyst deactivation was also observed. Therefore, liquid-phase Beckmann rearrangement of cyclohexanone oxime over heterogeneous catalysts was explored in this study. The heterogeneous liquid-phase catalytic rearrangement under mild reaction conditions was tested by using different solid acid catalyst and different solvents.

Solid acids such as MSU-S_{HY}, MSU-S_{BEA}, Al-MCM-41(70), silica-supported boron oxide, $InCl_3/ZrO_2$, 10 wt.% PO_4^{-3}/ZrO_2, 20 wt.% WO_3/ZrO_2, sulfated zirconia were tested in different solvents such as toluene, N,N-dimethylformamide, chlorobenzene, 1,2-dichlorobenzene and acetonitrile. The reaction temperature was 100 ^{o}C. Only 15% B_2O_3/SiO_2 gave 2% conversion after 24 h in N, N-dimethylformamide at 100 ^{o}C with 100% selectivity towards cyclohexanone. The desired ε-caprolactam was not observed. None of the other catalysts showed any activity under the reaction conditions, even after 48 h. The homogeneous liquid-phase Beckmann rearrangement of cyclohexanone oxime over P_2O_5 was tried out following reference [136]. N,N-dimethylforamide was used as the solvent and the reaction temperature was kept at

100 ^{o}C. After 2.4 h, the conversion was 7.3%. The selectivity to ε-caprolactam was only ~ 20% with the major product being cyclohexanone (80%) (Fig. 4-19).

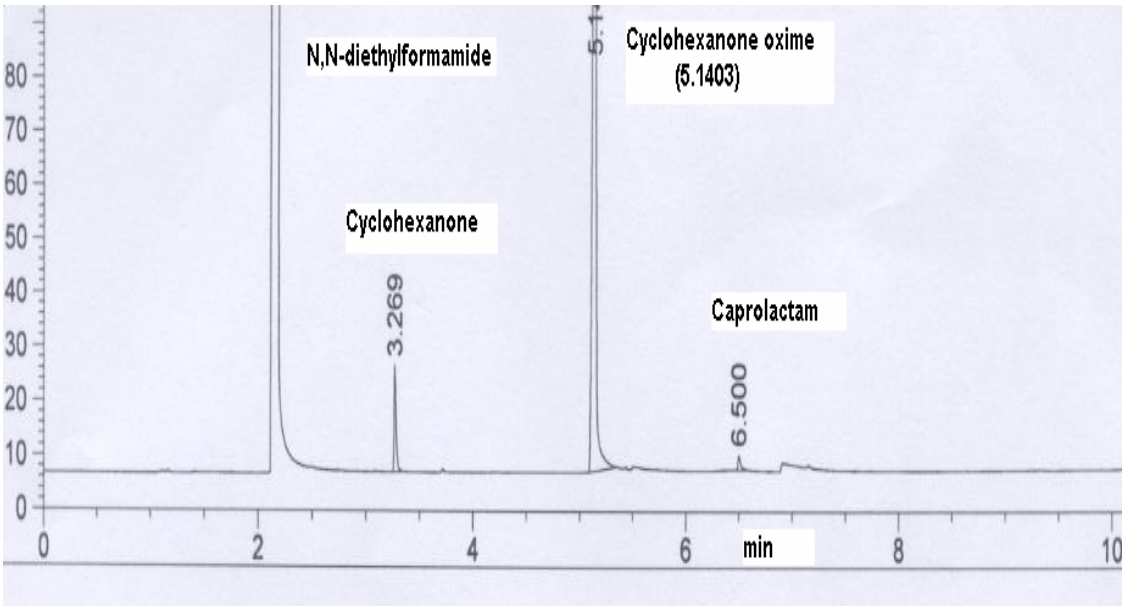

Fig. 4-19 Gas chromatogram of homogeneous liquid-phase Beckmann rearrangement of cyclohexanone oxime over P_2O_5 at 100 ^{o}C in N,N-dimethylformamide after 2.5 h.

Conclusion

1. MSU-S type materials prepared from nanoclustered zeolite seeds are good catalysts for α-pinene oxide isomerization. Although the conversion decreased with higher Si/Al ratio, the selectivity to campholenic aldehyde increased. HCl-treated MSU-S_{HY}(70) showed the highest selectivity, with 100 % selectivity to campholenic aldehyde.

2. B_2O_3/SiO_2 catalysts were also active in α-pinene oxide isomerization. However, the activity increased with boria loading up to 15 wt% and then decreased as the loading of boria was further increased. The selectivity was ~ 70% over these catalysts.

3. Toluene was a good solvent for α-pinene oxide isomerization. The conversion was higher in polar solvents but the selectivity to campholenic aldehyde decreased with increase of other side products.

4. MSU-S materials could be regenerated and reused with little loss of activity and selectivity. However, B_2O_3/SiO_2 catalysts lost activity after each round of reaction. This was due to deposition of organic residues which could not be removed by calcination at 350 °C.

5. Liquid phase Beckmann rearrangement reaction was carried out over different types of solid acid catalysts. However, none of the catalysts tested showed good activity or selectivity for the reaction.

References

[1] T. Yanagisawa, T. Shimizu, K. Kuroda, and C. Kato, Bull. Chem. Soc. Jpn., **63**, 988, (1990)

[2] J.S. Beck, J.C. Vartuli, W.H. Roth, M.E. Leonowicz, C.T. Kresge, K.D. Schmitt, C.T.W. Chu, D.H. Olson, E. W. Sheppard, S.B. McCullen, J.B. Higgins, and J.L. Schlenker, J.Am. Chem. Soc., **114**, 10834, (1992).

[3] Q.N. Le, R.T. Thomson, and G.H. Yokomizo, US Pat., 5134241 (1992).

[4] G. Bellussi, C. Perego, A. Carati, S. Peratello, E.P. Massara, and G. Perego, Stud. Surf. Sci. Catal., **84**, 85, (1995).

[5] B. Chiche, E. Sauvage, F. Di Renzo, I.I. Ivanova, and F. Fajula, J. Mol. Catal., A., **134**, 145, (1998)

[6] E. Armengol, M.L. Cano, A. Coma, H. Garcia, and M.T. Navarro, Chem. Commun., 519, (1995).

[7] B. Chakroborty, A.C. Pulikottil, and B. Viswanathan, Catal. Lett., **39**, 63, (1996).

[8] S.B. Pu, J.B. Kim, M. Seno, and T. Inui, Microporous. Mater., **10**, 25, (1997).

[9] S. Hitz, and R. Prins, J. Catal., **168**, 194, (1997).

[10] E. A. Gunnewegh, S.S. Gopie, and H. van Bekkum, J. Mol. Catal., **106**, 151, (1996).

[11] K.R. Kloetstra, and H. van Bekkum, Chem. Commun., 26, (1995).

[12] C.T.Kresge, M.E. Leonowicz, W.T. Roth, J.C. Vartuli, and J.C. Beck, Nature, **359**, 710, (1992).

[13] J.C. Beck, J. C. Vertuli, G.J. Kennedy, C.T. Kresge, W.J. Roth, and S.E. Schramm, Chem. Mater., **6**, 1816, (1994).

[14] J. M. Kim, S. K. Kim, and R. Ryoo, Chem. Commun., 259, (1998).

[15] A. Sayari, J. Am. Chem. Soc., **122**, 6504, (2000).

[16] Y. Liu, A. Karkamakar, and T. J. Pinnavaia, Chem. Commun., 1822, (2001).

[17] T. R. Pauly, Y. Liu, T. J. Pinnavaia, S. J. L. Billinge and T. P. Rieker, J. Am. Chem. Soc., **121**, 8835, (1999).

[18] T. R. Pauly, and T. J. Pinnavaia, Chem. Mater., **13**, 987, (2001).

[19] S.S. Kim, Y. Liu, and T. J. Pinnavaia, Microporous Mesoporous Mater., **44**, 489, (2001).

[20] D. Zhao, Q. Huo, J. Feng, B. F. Chmelka, and G. D. Stucky, J. Am. Chem. Soc., **120**, 6024, (1998).

[21] D. Zhao, J. Sun, Q. Li, and G.D. Stucky, Chem. Mater., **12**, 275, (2000).

[22] P. Schmidt-Wikel, C. J. Glinka, and G. D. Stucky, Langmuir, **16**, 356, (2000).

[23] S.S. Kim, T.R. Pauly, and T. J. Pinnavaia, Chem. Commun., 1661, (2000).

[24] Y. Liu, and T.J. Pinnavaia, J. Mater. Chem., **12**, 3179, (2002).

[25] H.Y. Zhu, G.Q. Lu, and X.S. Zhao, J. Phys. Chem., B **102**, 7371, (1998).

[26] R. Mokaya, Chem. Commun., 633, (2001).

[27] J.M. Kim, S. Jun, and R. Ryoo, J. Phys. Chem. B, **103**, 6200, (1999).

[28] D.T. On, P. Reinert, L. Bonneviot, and S. Kaliaguine, Stud. Surf. Sci. Catal., **135**, 929, (2001).

[29] D.T. On, and S. Kaliaguine, Angew. Chem. Int. Ed. Engl., **40**, 3248, (2001).

[30] L. Huang, W. Guo, P. Deng, and Q. Li, J. Phys. Chem. B, **104**, 2817, (2000).

[31] K.R. Kloetstra, H. van Bekkum, and T.C. Jansen, Chem. Commun., 2281, (1997).

[32] Y. Liu, W. Zhang, and T.J. Pinnavaia, J. Am. Chem. Soc., **122**, 8791, (2000).

[33] Y. Liu, W. Zhang, and T.J. Pinnavaia, Angew. Chem. Int. Ed., **40**, 1255, (2001).

[34] Y. Liu, and T.J. Pinnavaia, Chem. Mater., **14**, 3, (2002).

[35] Z.T. Zhang, Y. Han, F.S. Xiao, S.L. Qiu, L. Zhu, R.W. Wong, Y. Yu, Z. Zhang, B.S. Zou, Y.Q. Wang, H.P. Sun, D.Y. Zhao, and Y. Wei, J. Am. Chem. Soc., **123**, 5014, (2001).

[36] Z.T. Zhang, Y. Han, L. Zhu, R.W. Wong, Y. Yu, S.L. Qiu, D.Y. Zhao, and F.S. Xiao, Angew. Chem. Int. Ed., **40**, 1253, (2001).

[37] P.E.A. de Moor, T.P.M. Beelen, and R.A. van Santen, J. Phys. Chem. B, **103**, 1639, (1999).

[38] C.E.A. Kirschhock, R. Ravishankar, P.A. Jacobs, and J.A. Martens, J. Phys. Chem. B, **103**, 11021, (1999).

[39] C.E.A. Kirschhock, R. Ravishankar, F. Verspeurt, P.J. Grobet, P.A. Jacobs, and J.A. Martens, J. Phys. Chem. B, **103**, 4965, (1999).

[40] Y. Han, S. Wu, Y. Sun, D. Li, F.S. Xiao, J. Liu, and X. Zhang, Chem. Mater., **14**, 1148, (2002).

[41] D.T. On, and S. Kaliaguine, Angew. Chem. Int. Ed., **41**, 1036, (2002).

[42] S. Inagaki, S. Guan, T. Ohsuna, and O. Terasoki, Nature, **416**, 304, (2002).

[43] R.A. Sheldon, CHEMTECH, March 1994, p 38.

[44] R.A. Sheldon, H. van Bekkum, *Fine Chemicals through Heterogeneous Catalysis,* R. Wiley-VCH, 2001, p 2.

[45] K. Tanabe, *Solid Acids and Bases*, Academic Press, New York, 1970.

[46] K. Tanabe, and W.F. Hoeldrich, Appl. Catal. A; Gen., **181**, 399, (1999).

[47] G.C. Bond, Appl. Catal., **71**, 1, (1991).

[48] G.C. Bond, *Heterogeneous Catalysts, Principles and Applications,* Clarendon Press, Oxford, 1987, chapter 7

[49] K. Koboyashi, T. Shimuzu, and K. Inamura, Chem. Lett., 211, (1992).

[50] F. Cavani, G. Centi, F. Parrinello, and F. Trifiro, Stud. Surf. Sci. Catal., **31**, 227, (1987).

[51] S. Sato, S. Hasebe, H.Sakurai, K. Urabe, and Y. Izumi, Appl. Catal. A, **29**, 107, (1987).

[52] H. Sakurai, S. Sato, K. Urabe, and Y. Izumi, Chem. Lett., 1783, (1985).

[53] T. Curtin, J.B. McMonagle and B.K. Hodnett, Appl. Catal. A, **93**, 91, (1992).

[54] S. Sato, H. Sakurai, K. Urabe, and Y. Izumi, Chem. Lett., 277, (1985).

[55] S. Sato, K. Urabe, and Y. Izumi, J. Catal., **102**, 99, (1986).

[56] W.F. Yates, R.O. Downs, and J.C. Burleson, US Patent 3639391 (1972).

[57] K. Yoshida, K. Fujiki, T. Harada, Y. Moroi, and T. Yamaguchi, Jpn. Patent 7310478 (1973).

[58] B.Q. Xu, S.B. Cheng, S. Jiang, and Q.M. Zhu, Appl. Catal. A, **188**, 361, (1999).

[59] B.Q. Xu, S.B. Cheng, X. Zhang, S.F. Ying, and Q.M.Zhu, Chem. Commun., 1121, (2000).

[60] B.Q. Xu, S.B. Cheng, X. Zhang, and Q.M.Zhu, Catal. Today, **63**, 275, (2000).

[61] H. Matsuhashi, K. Kato, and K. Arata, Stud. Surf. Sci. Catal., **90**, 251, (1993).

[62] S. Sato, Kuroki, T. Sodesawa, F. Nozaki, and G.E. Maciel, J. Mol. Catal. A, **104**, 171, (1995).

[63] K. P. Peil, L.G. Galya, and G. Marcelin, J. Catal., **115**, 441, (1989).

[64] J.L. Parsons, M.E. Miberg, J. Am. Chem. Soc., **43**, 326, (1960).

[65] T. Takahashi, K. Ueno, and T. Kai, Canad. J. Chem. Eng., **69**, 1096, (1991).

[66] BASF, German Patent 1227028, (1976).

[67] Y. Izumi, and T. Shiba, Bull. Chem. Soc. Jpn., **37**, 1797, (1964).

[68] P.D.L. Mercera, J.G. van Ommen, E.B.M. Desbarg, A.J. Burggraf, and J.R.H. Ross, Appl. Catal. **71**, 199, (1994).

[69] T. Yamaguchi, Catal. Today, **20**, 199, (1994).

[70] K. Shibata, T. Kigoure, J. Kitagawa, T. Sumiyoshi, and K. Tanabe, Bull. Chem. Soc. Jap., **46**, 2985, (1973).

[71] S. Soled, and G.B. Mcvider, Catal. Today, **14**, 189, (1992).

[72] J.R. Shon, and H.J. Jang, J. Mol. Catal., **64**, 349, (1991).

[73] J.B. Miller, S.E. Rankin, and E.I. Ko, J. Catal. **148**, 673, (1994).

[74] D.H. Aguilar, L.C. Torres-Gonzalez, and L.M. Torres-Mortinez, J. Solid. State Chem. **158**, 349, (2000).

[75] K. Kamiya, S. Sakka, and Y. Takemichi, J. Mater. Sci., **15**, 1765, (1980).

[76] K. Ishihara, *Lewis Acids in Organic Synthesis*, H. Yamamoto (Ed.); Wiley-VCH, Weinheim, 2000; vol.1

[77] G.A. Olah, S.Kobayashi, and M.Tashiro, J.Am. Chem. Soc., **99**, 7498, (1972).

[78] J.A. Marshall, and K.W. Hinkle, J.Org. Chem., **60**, 1920, (1995).

[79] T.P. Loh, J. Rei, and M. Lin, Chem. Commun., 2515, (1996).

[80] T. Miyai, Y. Onishi, and A. Baba, Tetrahedron Lett., **39**, 6291, (1998).

[81] M. Yasuda, Y. Onishi, T. Ito, and Y. Baba, Tetrahedron Lett., **55**, 1017, (1999).

[82] V.R. Chaudhary, and S.K. Jana, J. Mol. Catal., **180**, 267, (2002).

[83] C. Walling, J. Am. Chem. Soc., **72**, 1164, (1950).

[84] J.B. Peri, J. Phys. Chem., **69**, 211, (1965).

[85] P. Fink, and J. Datka, J. Chem. Soc. Faraday Trans. 1, **85**, 309, (1989).

[86] D.J. Parillo, R. J. Gorte, and W.E. Farneth, J. Am. Chem. Soc., **115**, 12441, (1993).

[87] E.P. Parry, J. Catal., **2**, 371, (1963).

[88] H. A. Benesi, J. Catal., **28**, 176, (1973).

[89] H. Knözinger, H. Stolz, J. Phys. Chem., **75**, 105, (1971).

[90] M.H. Healy, L.F. Wieserman, E.M. Arnett, and K. Wefers, Langmuir, **5**, 114, (1989).

[91] H.Miyata, and J. Moffat, J. Catal., **77**, 110, (1980).

[92] A. Corma, C. Rodellas, and V. Fornes, J. Catal., **88**, 374, (1984).

[93] J. Kotral, and L. Kubelkova, Stud. Surf. Sci. Catal., **94**, 509, (1995).

[94] S.B. Sharma, B.L. Megers, D.T. Chen, J. Miller, and J.A. Dumesic, Appl. Catal., A, **102**, 253, (1993).

[95] H. Karge, and V. Dondur, J. Phys. Chem., **94**, 765, (1990).

[96] A. Corma, V. Fornes, F. Melo, and J. Herrero, Zeolites, **7**, 559, (1990).

[97] T. Hashiguchi, S. Sakai, *Acid-Base Catalysis,* K. Tanabe, H. Hattori, T.Yamaguchi, T. Tanaka (Eds.), Kodansha, Tokyo, 1989, p 191.

[98] S. Chatterjce, H.L. Greene, Y.J. Park, J. Catal., **138**, 179, (1992).

[99] G. Carr, G. Dosanjh, A.P. Millar, and D. Whittaker, J. Chem. Soc., Perkin Trans. **2**, 1419, (1994).

[100] H. van Bekkum, and H.W. Kouvenhoven, Stud. Surf. Sci. Catal., **41**, 45, (1988).

[101] W.F. Hölderich, J. Roseler, G. Heitmann, and A.T. Liebens, Catal. Today, **37**, 351, (1997).

[102] P.J. Kunkeler, J.C. van der Waal, J. Bremmer, B.J. Zuurdeeg, R.S. Downing and H. van Bekkum, Catal. Lett., **53**, 135, (1998).

[103] K. Wilson, A. Renson, and J.H. Clark, Catal. Lett., **61**, 51, (1999).

[104] N. Ravasio**,** M. Finiguerra, and M. Garagano, *Catalysis Organic Reactions,* F.E. Herkers (ed.) Dekker, New York, 1998, p 513.

[105] A. Aucejo, M.C. Bugruet, A. Corma, and V. Fornes, Appl. Catal., **22**, 187, (1986).

[106] O. Immuel, H.H. Scwarz, H. Starcke, and W. Swoden, Chem. Ing. Tech., **56**, 612, (1984).

[107] A. Costa, P.M. Deya, Sinisterra, and J.M. Marinas, Can. J. Chem., **58**, 1266, (1980).

[108] W.F. Hölderich, J. Roseler, G.Heitmann, and A.T. Liebens, Catal. Today, **37**, 353, (1997).

[109] H. Sato, and K. Hirose, Chem. Lett., 1765, (1993).

[110] A. Corma, H.Garcia, J.Primo, and E. Sastre, Zeolites, **11**, 593, (1991).

[111] M.A. Camblor, A. Corma, H. Garcia, V. Semmer-Herledan, and S. Valencia, J. Catal., **177**, 267, (1998).

[112] C. Young-Min, and R. Hyun-Ku Rhee, J. Mol. Catal. A, **175**, 249, (2001).

[113] J. Klinowski, J. Chem. Soc., **93**, 193, (1997)

[114] G.K. Chuah, S. Jaenicke, S.A. Cheong, and K.S. Chan, Appl. Catal. A, **145**, 267, (1996).

[115] F. Abbattista, A. Delastro, G. Gozzelino, D. Mazza, M. Vallino, G. Busco, and V. Lorenzelli, J. Chem. Soc. Faraday Trans., **86**, 3653, (1990).

[116] M. Scheithauer, R. K. Grasselli, and H. Knözinger, Langmuir, **14**, 301(1998).

[117] C.A. Emeis, J. Catal., **141**, 347, (1993).

[118] A.U. Rahama, *Nuclear Magnetic Resonance*, Springer-Verlag New York,1986.

[119] G. Engelhardt, Stud. Surf. Sci. Catal., **58**, 285, (1991)

[120] H. Sato, H. Yoshioka, and Y. Izumi, J. Mol. Catal. A, **149**, 25, (1999).

[121] H.P. Klug, L.E. Alexander, *X-Ray Diffraction Procedures for Polycrystalline and Amorphous Solids,* Wiley, New York, 1974, p.618.

[122] R.B. Borade, and A. Clearfield, Microporous Mater., **5**, 289, (1996).

[123] Y. Murakami, K. Otsuka, Y. Wada, and A. Morikawa, Bull. Chem. Soc. Jap., **63**, 340, (1990).

[124] P. Afanasiev, C. Geantet, and M. Breysse, J. Mater. Chem., **4**, 1653, (1994).

[125] G.K. Chuah, Catal. Today, **49**, 131, (1999).

[126] K. Arata and K. Tanabe, Chem. Lett. 1017, (1979).

[127] S. Kobayashi, Chem. Lett. 2187, (1991).

[128] BASF, German Patent No. 37686, 1978.

[129] P.S. Landis, P.B. Venuto, J. Catal. **6**, 245, (1966).

[130] Mobil Oil, US Patent No. 4359421, 982.

[131] H. Sato, N. Ishii, K. Hirose, S. Nakamura, Proc. 7th Int. Zeolite Conf., 1986, p.1213.

[132] H. Sato, K. Hirose, Y. Nakamura, Chem. Lett., 1987, (1993).

[133] W. F. Hölderich, and G. Heitmann, Catal. Today, **38**, 227, (1993).

[134] L.X. Dai, K. Koyama, and T. Tatsumi, Catal. Lett. **53**, 211, (1998).

[135] T. Ushikubo, and K. Wada, J. Catal., **148**, 138, (1994).

[136] H. Sato, H. Yoshioka, and Y. Izumi, J. Mol. Catal. A, **149**, 25, (1999).